FEDERAL UNIVERSITY OF SÃO CARLOS - UFSCar
CENTER OF EXACT SCIENCES AND TECHNOLOGY - CCET
DEPARTMENT OF MECHANICAL ENGINEERING - DEMec

Elisa Gamper Vergamini

DYNAMIC MODELING AND STUDY OF THE RESPONSE OF THREE AUTOMATED GUIDED VEHICULES PROPOSALS

São Carlos - SP
2021

Elisa Gamper Vergamini

DYNAMIC MODELING AND STUDY OF THE RESPONSE OF THREE AUTOMATED GUIDED VEHICULES PROPOSALS

Undergraduate thesis presented to the Department of Mechanical Engineering of the Federal University of São Carlos for the obtaining of the bachelor's degree in Mechanical Engineering.

Advisor: Prof. Dr. Luis Antonio Oliveira Araujo

São Carlos - SP
2021

FUNDAÇÃO UNIVERSIDADE FEDERAL DE SÃO CARLOS

COORDENAÇÃO DO CURSO DE ENGENHARIA MECÂNICA - CCEMec/CCET

Rod. Washington Luís km 235 - SP-310, s/n - Bairro Monjolinho, São Carlos/SP, CEP 13565-905

Telefone: (16) 33519703 - http://www.ufscar.br

DP-TCC-FA nº 10/2021/CCEMec/CCET

Graduação: Defesa Pública de Trabalho de Conclusão de Curso

Folha Aprovação (GDP-TCC-FA)

FOLHA DE APROVAÇÃO

ELISA GAMPER VERGAMINI

DYNAMIC MODELING AND STUDY OF THE RESPONSE OF THREE AUTOMATED GUIDED VEHICLES PROPOSALS.

Trabalho de Conclusão de Curso

Universidade Federal de São Carlos – Campus São Carlos

São Carlos, 14 de janeiro de 2021

ASSINATURAS E CIÊNCIAS

Cargo/Função	Nome Completo
Orientador	Luis Antonio Oliveira Araujo
Membro da Banca 1	João Vitor de Carvalho Fontes
Membro da Banca 2	Vitor Ramos Franco

Documento assinado eletronicamente por **Luis Antonio Oliveira Araujo**, **Docente**, em 20/01/2021, às 01:53, conforme horário oficial de Brasília, com fundamento no art. 6º, § 1º, do Decreto nº 8.539, de 8 de outubro de 2015.

Documento assinado eletronicamente por **Joao Vitor de Carvalho Fontes**, **Docente**, em 21/01/2021, às 11:26, conforme horário oficial de Brasília, com fundamento no art. 6º, § 1º, do Decreto nº 8.539, de 8 de outubro de 2015.

Documento assinado eletronicamente por **Vitor Ramos Franco**, **Docente**, em 21/01/2021, às 16:44, conforme horário oficial de Brasília, com fundamento no art. 6º, § 1º, do Decreto nº 8.539, de 8 de outubro de 2015.

A autenticidade deste documento pode ser conferida no site https://sei.ufscar.br/autenticacao, informando o código verificador **0315876** e o código CRC **79A1FD90**.

Referência: Caso responda a este documento, indicar expressamente o Processo nº 23112.000984/2021-08

SEI nº 0315876

Modelo de Documento: Grad: Defesa TCC: Folha Aprovação, versão de 02/Agosto/2019

Dedico este trabalho a todas as meninas que sonham em ser engenheiras. Que essa jornada seja a cada dia mais incentivada e reconhecida pela sociedade.

Agradecimentos

Agradeço primeiramente à minha família, por ser minha base, minha fonte inesgotável de amor e força.Vovó, Mama, Papa, Fer, Dani, Buzi, Piles e Pingo. Eu amo vocês mais do que jamais serei capaz de explicar.

À minha segunda família que me inspira todos os dias. Vó Rose, Carmen, Saulo, Natália, Brasa, Maria Clara, Marília, Paula e Daniel, amo demais vocês e agradeço todos os dias por ter vocês em minha vida.

À minha família de coração Tia Mara, Lucas, Jana e Danielzinho, obrigada por todo o amor de sempre. Et aussi à ma famille du coeur française, Marie et Augusto, je vous aime trop fort et vous mes manquez toujours.

A minhas amigas de sempre para sempre Flora, Gabi, Carol e Marcelinha, que a gente sempre siga com nosso amor de amigas-irmãs, que mesmo de longe nunca diminui.

À minha dupla preferida, Luigi e Leone, obrigada por basicamente cada segundo da minha graduação.

A toda minha turma, a 015 é sem dúvida a mais eclética, bizarra, engraçada e sensacional combinação de loucos geniais que eu amo de paixão e que já morro de saudades todos os dias.

Aos amigos Mama e Gandia, por cada momento durante essa graduação e na vida, amo muito vocês.

A todos com quem tive o prazer de conviver em meus dois intercâmbios, vocês me proporcionaram momentos inesquecíveis! Em especial Vitória, Zé, Julia, Rafa e Tiago.

A todos os professores de verdade com quem tive o prazer de aprender e conviver. Em especial minhas maiores inspirações, Prof. Mariano, Prof. Aroca e Prof. Luis.

Aos técnicos e demais funcionários da UFSCar, pessoas de quem o trabalho árduo simplesmente possibilitou minha formatura.

Ao meu orientador Prof. Luis, por toda a paciência e disposição de sempre em me ajudar, por sempre me aconselhar e me incentivar a ser a melhor versão de mim mesma.

Aos companheiros de Baja e CAAMec com quem compartilhei momentos únicos de aprendizado, de conquistas e de diversão, vocês moram no meu coração.

A todo o restante da minha família com quem sempre pude contar e compartilhar minhas maiores alegrias e tristeza. Minhas Tatas Ita e Tete que me ensinaram a nunca desistir e são meus maiores exemplos de força. Meu Tio Diniz e Tia Silvia, que amo tanto. Minhas primas amadas Maria Paula e Tucky, minhas parceiras de sempre. Meu Papy e minha Mamy, que mesmo não tendo a chance de conhecer sei que muito de vocês vive em mim.

Ao meu melhor amigo, companheiro, namorado e parceiro de vida. Cínpissi, a gente é força e vamos conquistar e tentar mudar o mundo juntos, obrigada por ser um exemplo de resiliência, superação e inspiração para mim! Je t'aime!

Merci!

"Eu não estou aceitando as coisas que eu não posso mudar,
estou mudando as coisas que eu não posso aceitar."
Angela Davis

Resumo

Os veículos automaticamente guiados (AGVs) são uma tecnologia amplamente usada na indústria para o transporte dos mais diversos produtos. Suas vantagens na velocidade, segurança e logística em galpões ou em linhas de produção são notáveis. Apesar de seu frequente emprego, a academia geralmente aborda os AGVs em termos de sua automação, sensoriamento e trilhas de locomoção, sendo pouco investigados, por exemplo, a fabricação de protótipos e a análise e desenvolvimento de suas suspensões. Considerando a aplicação de AGVs em ambiente externos, como terrenos arenosos ou neve, o presente trabalho visa estudar três modelos dentre os vários disponíveis no mercado: dois deles do tipo unit load (um com quatro rodas motoras e o outro com seis rodas, sendo motoras apenas o par central) e o terceiro do tipo empilhadeira com quatro rodas. São avaliados em especial o deslocamento linear vertical do conjunto carga + chassi e o deslocamento angular em torno do centro gravitacional dos AGVs (o chamado *pitch*). Para tal, aplicou-se o método do espaço de estados em conjunto com o software Matlab - Simulink a fim de obter as respostas no domínio do tempo para as entradas impulso, degrau e rampa. Foram feitas também análises de estabilidade em frequência, com a produção de diagramas de Bode e mapas de polos e zeros dos três sistemas. Foi identificada estabilidade em todos os conceitos avaliados, mas observou-se a insuficiência do amortecimento (definido com auxílio da literatura) para os modelos com quatro rodas. Por fim, verificou-se também que o deslocamento angular tem mais influência sobre a carga do que o deslocamento vertical nos três casos, o que enseja a necessidade de otimizar os coeficientes de amortecimento e rigidez para atenuar tal efeito ou ainda implementar uma alternativa de controle sobre a suspensão dos veículos.

Palavras-chave: AGV, modelagem dinâmica, suspensão, resposta no tempo, diagramas de Bode, estabilidade.

Abstract

The automatically guided vehicles (AGVs) are a technology widely used in industry for the transportation of the most diverse products. Its advantages in speed, safety and logistics in warehouses or production lines are remarkable. Despite their frequent use, the academy approaches in AGVs are, generally, towards their automation, sensoring and locomotion trails, being little explored, for example, the manufacturing of prototypes and the study and developing of their suspension. Considering the application of AGVs in outdoor environments, such as sandy terrains or snow, the present work intends to investigate three models among those available in market, being: two of them of the unit load type (one with four driving wheels and the other with six wheels, being only the central pair driving) and the third one a forklift with four wheels. More specifically, the linear vertical displacement of the set load + chassis and the angular displacement (pitch) around their gravitational center are evaluated. To reach this, the state space method was applied together with the Matlab - Simulink software in order to obtain the responses in time domain for the inputs pulse, step and ramp. Frequency stability analyses also took place and were performed with the aid of Bode diagrams and maps of poles and zeros for the three systems. All concepts were proved stable, even though the damping (defined with support on literature) was found insufficient for the four-wheel models. Finally, it was verified for all cases that the pitch has more influence on the load then vertical displacement, which brings the need of optimizing damping and stiffness coefficients to attenuate such an effect or even implement an alternative control for the vehicles' suspension.

keywords: AGV, dynamic modeling, suspension, time response, Bode diagrams, stability.

List of Figures

List of Tables

Contents

1 Introduction

As an introduction, a brief contextualization of Automated Guided Vehicles (AGVs) development history will be presented, just like their presentation as dynamic systems. After these topics, the motivation for the investigations made is described altogether with its objectives.

1.1 Automated Guided Vehicles: history and nowadays

The emergence of new technologies has provided and given rise to new tools that enable and optimize the production and management processes. According to Fazlollahtabar e Niaki (2018), Ferrelli et al. (2015), with the advent of automation and advances in technology, engineering and science have played a fundamental role in the use of innovation in production, impacting the productivity and boosting competitiveness, which contributes to the appearance of new automation methods in industry.

Companies seek to optimize their processes, replacing man in the execution of productive activities by electronic or mechanical means with high levels of technology (SANTOS et al., 2018). The development of AGVs was to replace a pilot industrial transport by a software capable of following the route and carrying out, or even loading and unloading materials without the need of direct human interation, offering security and speed in programmed continuous operations (YAN et al., 2017).

The AGVs' history begins around 1950, in Northbrook, USA, by Barret Electronics. The developed system consisted simply of a trailer that followed a wire as path, instead of a rail. Later, other types of systems were created, among then the firsts AGVs capable of following UV markings on the floor. This system was implemented at Willis Tower (formerly Sears Tower) in Chicago as a way of delivering mail to all its offices (CATARRINHO, 2018).

Nowadays, according to Haderspeck (2019) the AGV consists of a programmed electric vehicle, guided through rails, optical sensors, radio frequency or laser. These vehicles are integrated in an automated process and programmed to communicate with other robots as well as other components of the installation so that the product is moved smoothly through the warehouse, whether it is transporting goods from one point to another or providing sequential service to assembly operations(PéREZ, 2010)). For each function there is a specific model of Automatically Guided Vehicle that allows customized solutions. The most employed are the unit load AGV, forklift AGV, lift platform AGV, towing AGV, among others.

In Figure 1 two example of the models addressed in the development of this study are shown. The unit load AGV is introduced in two different configurations - with four motorized wheels and with six wheels, the later having only the central pair motorized - and the forklift model is also addressed by this work. The selection was created based on the models' popularity.

Figure 1 – AGV models analyzed

(a) Unit load AGV model.
Source: Extracted from Scott-Automation (2020).

(b) Forklift AGV model.
Source: Extracted from BA-Systèmes (2020).

All of these AGVs move automatically. Thanks to this intelligent method, the machine can perform its activities without much effort, quickly, correctly, effectively and safely. This is reached because the equipment can adapt to narrow places, share aisles with people and other utensils, in addition to adapting easily to changes in layout (KIM; TANCHOCO, 1999). Being this versatile, it is important to assure the security of their operation; this is, in fact, one of the great gains of the AGV, as the system has a programmed continuous speed and is equipped with optical and ultrasonic sensors on all sides, which makes them avoid collisions with their obstacles, from operators to other vehicles in the factory, problems that are commonplace when there are operators driving the vehicles (HAMMOND, 1986). In addition, AGVs are completely flexible, require little maintenance and have a higly variable load capacity. All these factors make this technology a real revolution in the world of production (CANO, 2006).

Although the AGV is a widely applied and studied technology, little is found in the literature on its projects and dynamic analysis. In general, the studies are more directed to its autonomous movement programming and logistics definitions.

1.2 The AGV as a dynamic system

According to Felicio (2010), a dynamic system is a set of components that founds itself inside a frontier and has responses that vary over time. In this context, these outputs are often related to the position or the movement of the parts, for example. The dynamics of AGV models are similar to that of conventional cars, especially for the four and six-wheels models, while the forklift model will be analogous to a conventional forklift.

Considering possible obstacles in the path of an AGV, the suspension will be responsible for absorbing the impact caused by the input on the load. Therefore, similarly to the study of the suspension of any vehicle, each module, as shown in Figure 2, is represented by a spring, which assume the role of tire's rigidity, the mass of the whole wheel, and a spring + damper as the suspension itself. These modules will support the chassis and the load masses, with the center of gravity depending on the AGV concept treated (WITCZAK et al., 2020).

Figure 2 – Suspension module

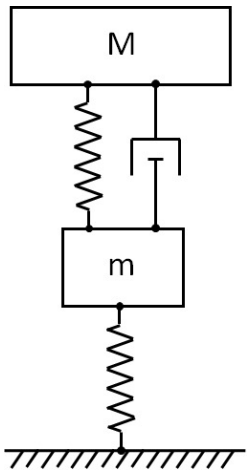

Source: Addapted from Witczak et al. (2020).

Normally, the path through which AGVs usually travel is flat terrain, without many obstacles, precisely to avoid suspension responses that result in the fall, break or loss of the transported load. However, the exploration of the use of AGVs in sandy terrains or even on snow were already explored (HOOGEWIJS, 2020). Taking this possibility, it is necessary to better understand the behavior of AGVs for eventual obstacles, enabling the implementation of a control system or even an active suspension for such applications.

1.3 Undergraduate thesis goals

Given how little dynamic aspects of AGVs are investigated, the present work is proposed in order to contribute to the evolution of this area of knowledge. This intention is concisely developed and summarized in the following section 1.3.1.

1.3.1 Objectives

The general objective of this work is to obtain the dynamic model and compare the suspension of three AGV models used in the industry, capturing the advantages and disadvantages of each one as a dynamic system.

The marked main goal is directly connected to several specific points, which shall be listed hereinafter:

- To develop the suspension dynamic models of the three automated guided vehicles;
- To analyze and compare the responses of the models in time and in frequency domains for different inputs;
- To study the stability of each model.

1.4 Thesis structure

The work is divided in order to be the most logical and as fluid as possible. For that, subsections are used and the general argument exposition sequence is easily observed through its titles.

The text is divided henceforth in four chapters. The second one introduces a literature review over what has already been studied and developed in this thesis topics, like general dynamic modeling theory and some other tools and methods of the same context. Authors' views and interpretations on these subjects are also considered.

In the third chapter, the methods and general aspects on which the work was developed are described. This description is supported by the contents of the previous sections.

Finally, chapter four exposes all the results achieved by the modeling and computer simulations, while the conclusion and global considerations over the work here registered are presented in chapter five.

2 State of the Art

This part comprises all theoretical and developed knowledge of engineering that is related to dynamic systems modeling and necessary for the full understanding of the work. Based on classical and modern literature, the text also features content on the understanding of the state-space method, the inputs and outputs and in the two pillars of response analysis: the time and frequency domains (being the stability analysis characterized as part of the possible procedures on the later).

2.1 Dynamic system modeling theory

A system is determined by a set of parts or components, of any size and without quantity limitations. This set must be limited by an imaginary boundary determined by the purpose of the study. This boundary determines what belongs to the system and what will be considered as external environment, thus making it possible to define the system's inputs and outputs (FELICIO, 2010).

According to Felicio (2010), an input is a phenomenon of any magnitude capable of modifying the state of the system, even if minimally. In dynamic systems, the inputs are considered to be independent of the system, i.e., without suffering any influence from it. Just as well, system's outputs are any magnitudes that characterize its state, that is, the information that comes out of it. Such information can be analyzed or defined as an objective to be, eventually, controlled. Just as the inputs do not depend on the system, the outputs do not depend on the external environment. If something from the external environment influences an output, it must be considered an input.

There is no uniqueness between outputs and inputs. In other words, a system can have multiple inputs and multiple outputs. To organize this fact, there are systems denominated SISO (single input and single output), MISO (multiple inputs and single output), MIMO (multiple inputs and multiple outputs) or SIMO (single input and multiple outputs), as exemplified in Figure 3 (BOTTURA, 1982).

Figure 3 – Different combinations of input-outputs for dynamic systems

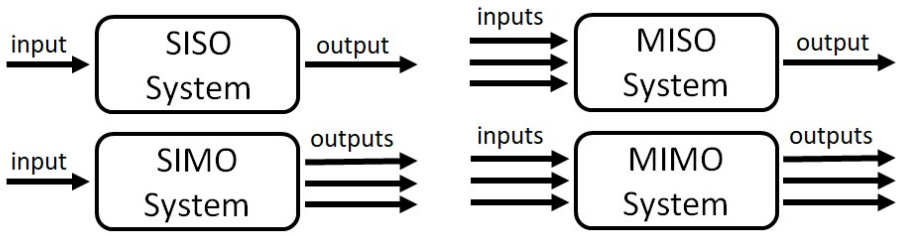

Source: Addapted from Felicio (2010).

The modeled systems can be of diverse natures, they can be mechanical, hydraulic, thermal or electrical, or even a mix of them all at once. The focus of this thesis will be the analysis of the mechanical system of three different AGVs.

One of the most fundamental and well-established model unit cell of mechanical systems is the mass-spring-damper, as shown in Figure 4.

Figure 4 – Mass-spring-damper system representation

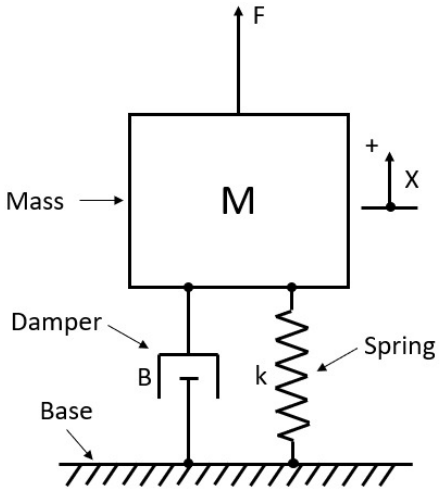

Source: Addapted from Felicio (2010).

In the system of Figure 4, only one input is shown, the force F, which is applied to the mass M. Such mass is supported by a damper with damping coefficient B and a spring with spring coefficient k. A few of the possible and countless outputs for this system can be the position x of the mass, the force of the spring on the ground, the temperature of the damper oil, among others.

The most common analysis is that of a system with only one input and only one output being studied, keeping the other inputs as constant. A system can also be classified as linear or non-linear. Linear systems can be described by a set of linear ordinary differential equations with constant coefficients. Assuming that in cases of multiple varying entries, the study of the response can be done considering one input at a time, and through the principle of superposition, it is reasonable to add all the individual responses. For a non-linear system, on the other hand, this principle is not applicable and the study will involve greater complexity (FELICIO, 2010).

The modeling of a system, essentially, has four main steps: the hypotheses adopted, the application of basic laws, the relations between the variables and finally the validation of the model. The first three steps are merged in the process. In this work, a experimental validation will not be performed, but it is important to emphasize that only through comparison with reality is it possible to truly validate a model (KARNOPP et al., 2006).

For the development of dynamic models of mechanical systems, Newton's second law will be the basic physics relation used for equations construction. The law is applied to each mass of the system and it is restricted to just a linear or just an angular coordinate. It is assumed that

conditions have been established to guarantee such restrictions. Equations 2.1 and 2.2 represents, respectively, Newton's second law for translation and rotation on an axis.

$$\sum F = m\ddot{x} \tag{2.1}$$

In which $\sum F$ is the sum of external forces acting on the body in the x direction, x is the displacement in the x direction, m is the mass of a point or rigid body under study and $\ddot{x}$ is the acceleration of the body in the x direction.

$$\sum M = I\ddot{\theta} \tag{2.2}$$

In which $\sum M$ is the sum of the external moments acting on the body in relation to the rotation axis, θ is the angular displacement of the body, I is the moment of inertia of the body in relation to the rotation axis and $\ddot{\theta}$ is the angular acceleration of the body.

In both equations, an intrinsic and pre-established signal convention is incorporated. For linear movements, the positive direction is chosen so that the displacement is equal to the positive direction adopted for the forces acting on the point. Similarly, for angular movements, the positive direction for angular displacement must be the same positive direction for the moments that act on the body. Acceleration, speed and displacement, both linear and angular, are related by derivations, operations that do not reverse the reference direction.

After applying the basic laws, the next step is to establish relations between the variables. Considering the mechanical reference system like the one in Figure 4, the damper and the spring will exert forces on the mass.

The spring adopted in the system is called linear, that is, the relation between force and deformation is linear. The springs are considered ideal, i.e. they have no mass and no energy loss effect. It is evident that, in reality, this do not occur perfectly; for many springs, however, this is precise if a range of forces and deformations are respected. Mathematically these limitations do not exist, and it is up to the analyst to verify the model's validity (FELICIO, 2010).

Springs are classified into two types: translation springs - generally referred to as only springs - and rotation springs - also known as torsional springs. For an ideal linear spring, like the one in Figure 5, the model is given by Equations 2.3 and 2.4.

Figure 5 – Linear string

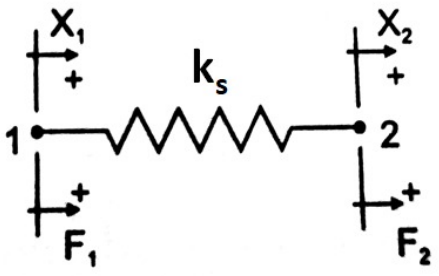

Source: Addapted from Felicio (2010).

$$F_1 = -k_s (x_1 - x_2) \tag{2.3}$$

$$F_2 = -k_s (x_2 - x_1) \tag{2.4}$$

Where x_1 and x_2 are the linear displacements, respectively, of the extremities 1 and 2 of the spring - the difference between these displacements is the deflection of the spring -, k_s is the coefficient of the spring, considered constant, F_1 is the force of the spring on the body that is coupled at the extremity 1 and F_2 is the force of the spring on the body that is coupled at the extremity 2.

Considering the torsional spring illustrated in Figure 6, the modeling is given by equations 2.5 and 2.6, analogously to the translation springs.

Figure 6 – Torsional string

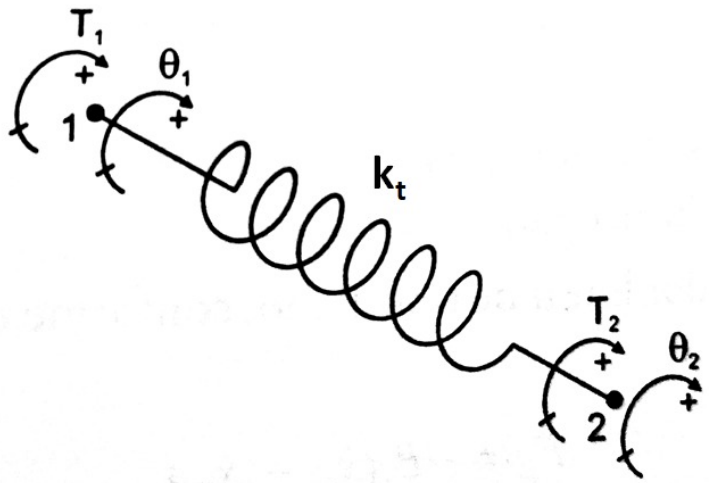

Source: Addapted from Felicio (2010).

$$T_1 = -k_t (\theta_1 - \theta_2) \tag{2.5}$$

$$T_2 = -k_t (\theta_2 - \theta_1) \tag{2.6}$$

Where θ_1 and θ_2 are the angular displacements, respectively, of the extremities 1 and 2 of the spring - the difference between these displacements is the angular deflection of the spring -, k_t is the coefficient of the torsional spring, considered constant, T_1 is the torque of the torsional spring on the body that is coupled at the extremity 1 and, similarly, the torque T_2 is the one of the spring on the body that is coupled at the extremity 2.

The dampers have their strength proportional to the speed difference of their ends. For modeling, dampers are considered ideal, that is, linear, without mass and without any elasticity effect. Analogously to springs, they can be classified into two types: translation and rotation (torsional) dampers (FELICIO, 2010).

For an ideal linear damper, as the one in Figure 7, the model is given by Equations 2.7 and 2.10.

Figure 7 – Linear damper

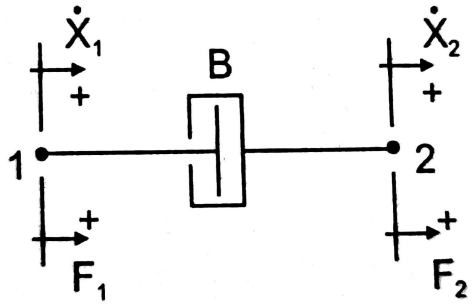

Source: Addapted from Felicio (2010).

$$F_1 = -B\left(\dot{x_1} - \dot{x_2}\right) \tag{2.7}$$

$$F_2 = -B\left(\dot{x_2} - \dot{x_1}\right) \tag{2.8}$$

Where $\dot{x_1}$ and $\dot{x_2}$ are the velocities, respectively, of the ends 1 and 2 of the damper, B is the damper coefficient, considered constant, F_1 is the force of the damper on the body that is coupled at the extremity 1 and F_2 is the force of the damper on the body that is coupled at the extremity 2.

Considering the torsional damper illustrated in Figure 8, the modeling is given by equations 2.7 and 2.10, similarly to the translation dampers.

Figure 8 – Torsional damper

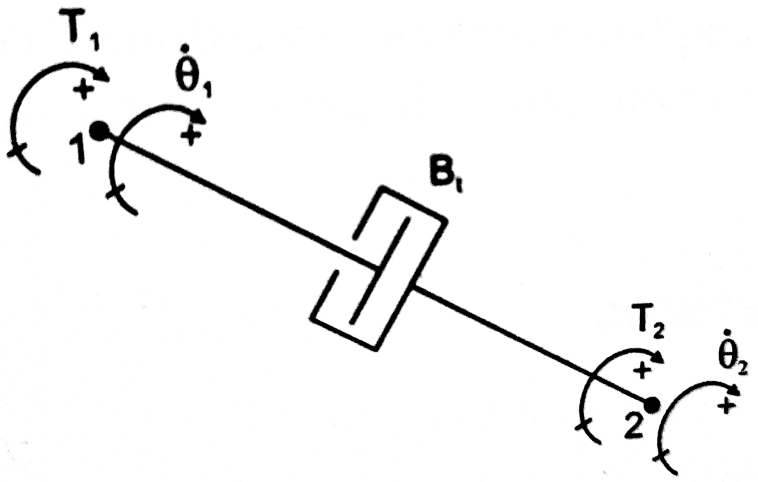

Source: Addapted from Felicio (2010).

$$T_1 = -B\left(\dot{\theta_1} - \dot{\theta_2}\right) \tag{2.9}$$

$$T_2 = -B\left(\dot{\theta}_2 - \dot{\theta}_1\right) \tag{2.10}$$

Where $\dot{\theta}_1$ and $\dot{\theta}_2$ are the angular velocities, respectively, of the extremities 1 and 2 of the damper, B is the coefficient of the torsional damper, considered constant, T_1 is the torque of the torsional damper on the body that is coupled at the extremity 1 and T_2 is the torque of the damper on the body that is coupled at the extremity 2.

Considering the equations and mathematical relations explained above, it is possible to proceed with the modeling. Considering a SISO system - that is, with only one input and one output -, the ratio of the output to the input is called the transfer function (TF) as shown in Equation 2.45 and Figure 9.

Figure 9 – Transfer function representation

Source: Author.

$$TF = \frac{q_o}{q_i} \tag{2.11}$$

In which, q_i is the input and q_o is the output. Three conditions are necessary to obtain a TF:

- All other inputs are null or constant;
- All initial conditions of all inputs are null;
- All other conditions are constants.

Thus, for a mechanical system like the one in Figure 4, the general set of hypotheses adopted is listed below (FELICIO, 2010):

1. All masses are rigid bodies and have constant values;
2. The springs are pure and linear;
3. The dampers are pure and linear;
4. When the mass can move, its movement is in one direction;
5. When the mass can rotate, the rotation is around a single axis;
6. All initial conditions are null;
7. All contact surfaces have zero friction (planes, bearings, etc.);

8. The variations in the magnitudes of the system are relatively small in order to maintain the behavior of the linear system.

More hypotheses can be added according to the application. Therefore, the basic laws associated with the relations between the variables of the elements of the system will form a differential equation like Equation 2.12.

$$F = k_s x + B\dot{x} + m\ddot{x} = (k_s + BD + mD^2)x \tag{2.12}$$

Note the appearance of operator D, a derivative operation indicator. When the second power is added, it represents a second order derivative.

Considering a force F as input of the system and a displacement x as output, the TF is obtained as in Equation 2.13.

$$\frac{x}{F}(D) = \frac{1}{mD^2 + BD + k_s} \tag{2.13}$$

Defining the following equations and considering all therms of 2.13 divided by k_s, Equation 2.17 can be obtained.

$$K = \frac{1}{k_s} \tag{2.14}$$

$$\omega_n = \sqrt{\frac{k_s}{m}} \tag{2.15}$$

$$\frac{2\zeta}{\omega_n} = \frac{B}{k_s} \; or \; \zeta = \frac{B}{2\sqrt{k_s m}} \tag{2.16}$$

$$\frac{x}{F}(D) = \frac{K}{\frac{D^2}{{\omega_n}^2} + \frac{2\zeta}{\omega_n}D + 1} \tag{2.17}$$

In which K is the gain of the transfer function (Equation 2.14), ω_n is the undampeded natural frequency $[rad/s]$ (Equation 2.15) and ζ the damping factor (Equation 2.16).

This TF is given as the standard second-order mechanical system. The same method can be applied to a system with more masses, but instead of scalar coefficients, matrices will be used in the equations. These matrices are squared with dimensions equal to the number of outputs, and non-zero values are necessarily present in the main diagonal. The stiffness matrix - representing the springs - and the damping matrix, have the coefficients of springs and dampers acting directly in the mass, and the other elements will be factors associated with the couplings between masses (AGUIRRE, 2004).

2.2 State space

Complex dynamic systems (MIMO) generally require high-order nonlinear differential equations for its description, whose solutions are rare and difficult analytically and even numerically (DORF; MBIHOP, 2013).

A state space representation is a mathematical model of a physical system composed of a set of related input, output and state variables using first order differential equations. The variables are expressed in vectors and the differential and algebraic equations are written in the matrix form, in a way that is possible only when the dynamic system is linear and time-invariant (OGATA, 2010).

According to Nise (2009), the state of a system is the smallest set of variables that allows its complete description. That means that once its dynamic equation and respective sequences are known, its future state can be predicted. For the representation of the state, the linear system, presented on Equation 2.18 is usually used.

$$\begin{aligned} \dot{x}(t) &= Ax(t) + Bu(t) \\ y(t) &= Cx(t) + Du(t) \end{aligned} \tag{2.18}$$

In which:
$x(t)$ is the state variables vector of size n
$y(t)$ is the outputs vector of size q
$\dot{x}(t)$ is the vector of the derivative of the state variables of size n
$u(t)$ is the inputs vector of size p
A is the state matrix of size $n \times n$
B is the input matrix of size $n \times p$
C is the output matrix of size $q \times n$
D is the feed-forward matrix of size $q \times p$

Applying the Laplace transform in Equation 2.18, changing it from the time domain to the frequency domain, we obtain Equation 2.19.

$$\begin{aligned} sX(s) - x(0) &= AX(s) + BU(s) \\ Y(s) &= CX(s) + DU(s) \end{aligned} \tag{2.19}$$

In order to solve the system, the first equation is replaced in the second, resulting in Equation 2.20.

$$Y(s) = C((sI - A)^{-1}x(0) + (sI - A)^{-1}BU(s)) + DU(s) \tag{2.20}$$

This method allow the determination of the TFs, relating each input to an output. With this in hand, it is convenient and feasible to apply the superposition method and, thus, to obtain outputs under the influence of two or more inputs.

2.3 Types of inputs

The singular signs - or, as also called, "signs of excitement" - are classified in the discrete case or in the continuous case. Although there are an infinite number of signs in these families, in practice only some of more interest are actually used. This is the case of three of them in particular: unit pulse, unit step and unit ramp, which are normally used as signals of excitation, i.e., inputs for systems being analyzed (GEROMEL; PALHARES, 2004).

Pulse

The representation and notation of the pulse function is presented, respectively, in Figure 10 and in Equation 2.21.

Figure 10 – Representation of the pulse function for $t > 0$

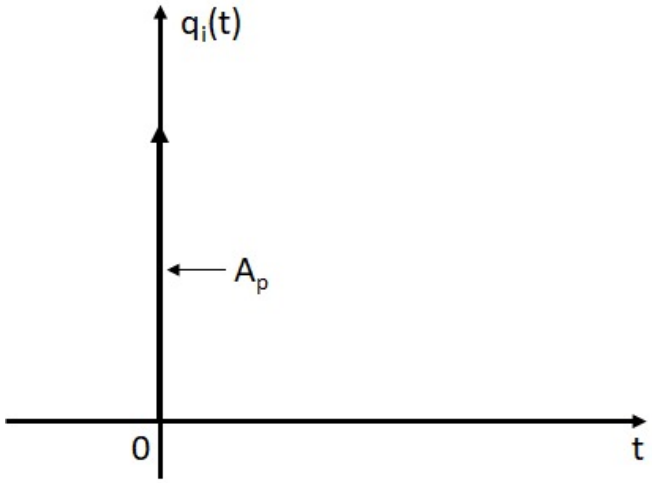

Source: Addapted from Felicio (2010).

$$q_i(t) = A_p\delta(t) \tag{2.21}$$

The Dirac delta function, also known as the δ function, is a distribution on the real line, which is infinite at zero point and zero on the rest of the line. The integral of the Dirac Delta function on every line is defined as having a value of area equals 1.

Therefore, by adding the constant $A_p \neq 0$ and multiplying by the unit function δ, a pulse of any desired magnitude is obtained. Physically, the function represents a one-time impact that will act as input to the system (KLUEVER, 2015).

Step

The representation and notation of the step function is presented, respectively, in Figure 11 and in Equation 2.22.

Figure 11 – Representation of the step function for $t > 0$

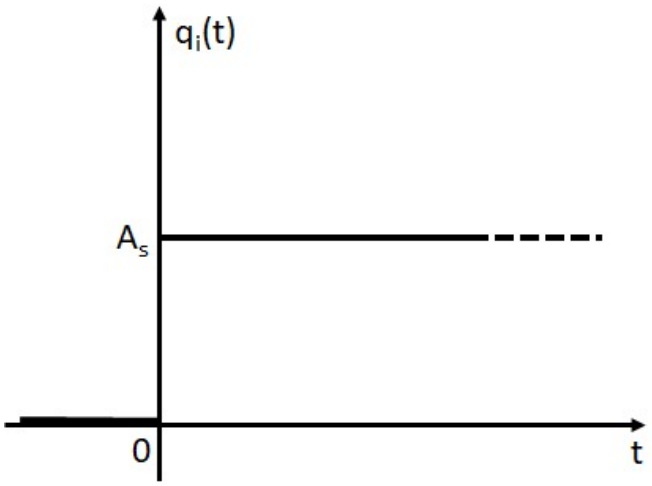

Source: Addapted from Felicio (2010).

$$q_i(t) = A_s u(t) \tag{2.22}$$

If the unit step $u(t)$ is multiplied by a constant $A_s \neq 0$ a step of amplitude A_s is obtained. The step function will physically represent, as the name suggests, a step - or a change from an input to another constant value kLUEVER15.

Ramp

The representation and notation of the ramp function is presented, respectively, in Figure 12 and in Equation 2.23.

Figure 12 – Representation of the ramp function for $t > 0$

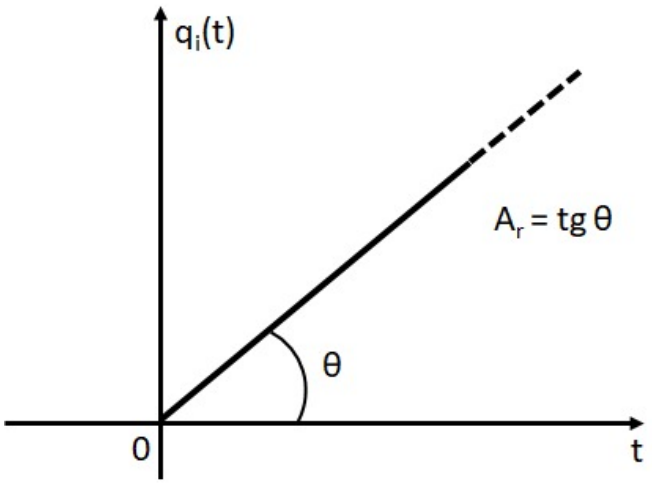

Source: Addapted from Felicio (2010).

$$q_i(t) = A_r t \tag{2.23}$$

If we multiply the unit ramp (the same as the time vector) by a constant $A_r \neq 0$ a ramp with a A_r slope is obtained. Physically, the ramp function will represent an input with constant variation in time, for example an uphill to which a car must climb (KLUEVER, 2015).

Therefore, a pulse is well determined by its area, the step by its amplitude and the ramp by its slope (or inclination).

Sinusoidal

In addition to the most common intakes explained above, the input in the frequency scope is also used precisely to understand the behavior of the system when subjected to a sinusoidal excitation (SPERANZA, 2016). An example of this excitation is shown in Figure 13 and in Equation 2.24.

Figure 13 – Representation of the sinusoidal excitation for $t > 0$

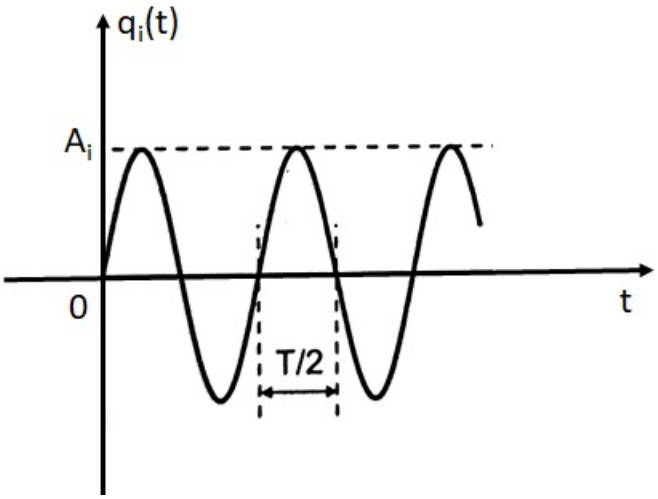

Source: Addapted from Felicio (2010).

$$q_i(t) = A_i sin(\omega t) \tag{2.24}$$

Where A_i is the amplitude, ω is the frequency that determines the period T. Along time, these parameters define an input with the sinusoidal format as desired.

2.4 Temporal response

The temporal response can be classified into two different types: permanent and transient. The steady-state part is a forced response depending on the type of excitation the system underwent, whether it be an impact (pulse), a change in position (step) or a change in speed (ramp). The transient portion is the system's natural response, which depends on the transfer function (FELICIO, 2010). This response is marked by characteristics that provide greater capacity for studying the system: the delay time, the rise time, the peak time, the maximum

overshoot and the settling time (GEROMEL; PALHARES, 2004). An example of a temporal response is shown in Figure 14.

Figure 14 – Representation of a temporal response of a system and its characteristics

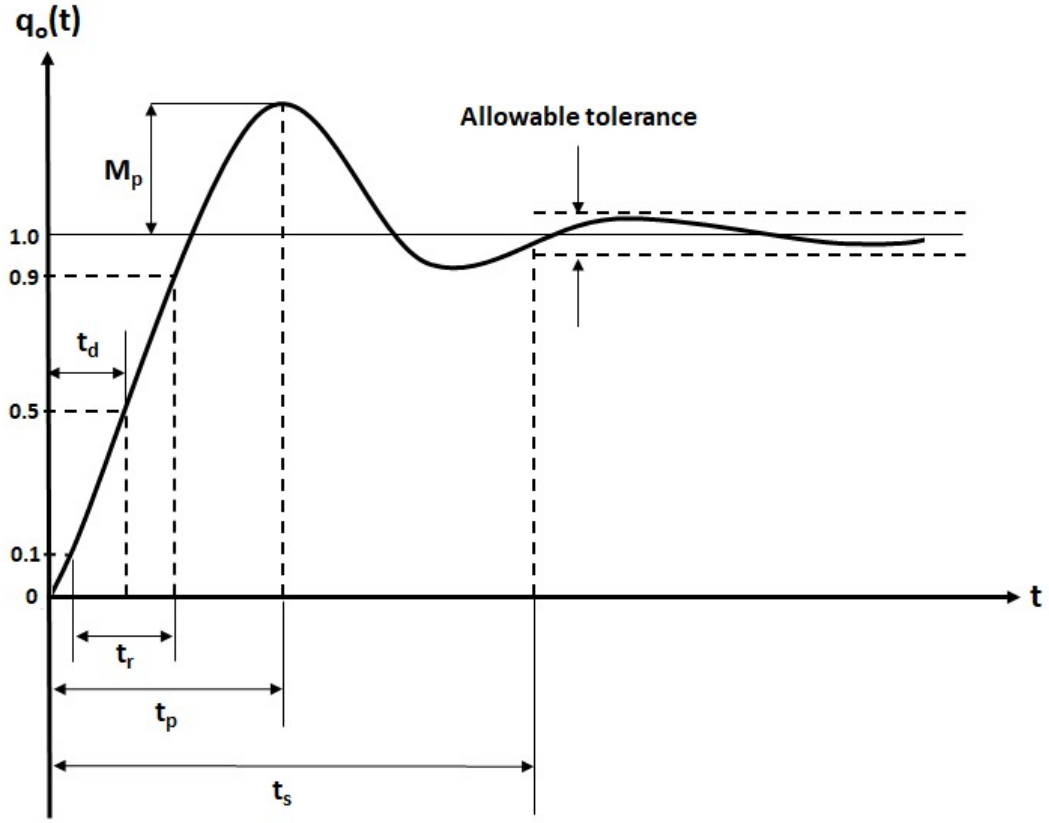

Source: Addapted from Karnopp et al. (2006).

The transient response characteristics are highlighted in Figure 14; a brief explanation of each one is presented as it follows (KARNOPP et al., 2006):

- Delay time (t_d): Time when system response reaches half the regime value;
- Rise time (t_r): Time which takes for the system response to go from 10% to 90% of the regime value;
- Peak time (t_p): Time that the system takes to reach the first overshoot peak;
- Maximum overshoot (M_p): Maximum value that the system reaches in relation to the regime value;
- Settling time (t_s): Time for the system to reach and stay within a range of specified values (usually 2%).

In order to obtain the temporal response of a mechanical system according to the order with a TF like that of Equation 2.25, it is necessary to find the homogeneous solution of the differential equation presented in Equation 2.26 (FELICIO, 2010).

$$\frac{q_o}{q_i}(D) = \frac{K}{\frac{D^2}{{\omega_n}^2} + \frac{2\zeta}{\omega_n}D + 1} \tag{2.25}$$

$$\frac{1}{{\omega_n}^2}D^2 q_o + \frac{2\zeta}{\omega_n}Dq_o + q_o = Kq_i \tag{2.26}$$

Equation 2.26 is also represented by the Equation 2.27.

$$\frac{1}{{\omega_n}^2}\frac{d^2 q_o}{dt^2} + \frac{2\zeta}{\omega_n}\frac{dq_o}{dt} + q_o = Kq_i \tag{2.27}$$

The solution for the differential Equation 2.27 is presented in Equation 2.28.

$$q_o = q_{oh} + q_{op} \tag{2.28}$$

Analyzing only the solution of the homogeneous part, we have the homogeneous differential equation, that is presented in Equation 2.29.

$$\left(\frac{D^2}{{\omega_n}^2} + \frac{2\zeta}{\omega_n}D + 1\right) q_o = 0 \tag{2.29}$$

Which has the characteristic equation 2.30 below.

$$\frac{D^2}{{\omega_n}^2} + \frac{2\zeta}{\omega_n}D + 1 = 0 \tag{2.30}$$

The roots of the characteristic equation are presented in Equation 2.31.

$$r_1, r_2 = -\zeta\omega_n \pm \omega_n\sqrt{\zeta^2 - 1} \tag{2.31}$$

Therefore, depending on the ζ value, the roots can be:

1. If $\zeta = 1 \rightarrow$ roots r_1 and r_2 are real and repeated. In this case, the system is called Critically Damped System

2. If $\zeta > 1 \rightarrow$ roots r_1 and r_2 are real and distinct. In this case, the system is called Over-Damped System

3. If $\zeta < 1 \rightarrow$ roots r_1 and r_2 are complex roots combined. In this case, the system is called Under-Damped System

In the following sections, the forms of the q_o function will be presented for each of the three systems presented befor.

Critically Damped Sytem

As $\zeta = 1$, from Equation 2.31 roots presented in Equation 2.32 are obtained.

$$r_1 = r_2 = -\omega_n \tag{2.32}$$

Therefore, by the theory of differential equations, the function q_{oh} is the one presented in Equation 2.33, where A and B are constants.

$$q_{oh} = Ae^{-\omega_n t} + Bte^{-\omega_n t} \tag{2.33}$$

Over-Damped System

As $\zeta > 1$, again from Equation 2.31 the roots presented in Equation 2.34 are obtained.

$$\begin{cases} r_1 = \left(-\zeta + \sqrt{\zeta^2 - 1}\right)\omega_n \\ r_2 = \left(-\zeta - \sqrt{\zeta^2 - 1}\right)\omega_n \end{cases} \tag{2.34}$$

Therefore, for this case the q_{oh} function is the one presented in Equation 2.35.

$$q_{oh} = Ae^{\left(-\zeta+\sqrt{\zeta^2-1}\right)\omega_n t} + Bte^{\left(-\zeta-\sqrt{\zeta^2-1}\right)\omega_n t} \tag{2.35}$$

Under-Damped System

As $\zeta < 1$, once more from Equation 2.31 the roots presented in Equation 2.36 are determined.

$$r_1 = r_2 = -\zeta\omega_n \pm i\sqrt{1 - \zeta^2\omega_n} \tag{2.36}$$

Therefore, for this case the q_{oh} function is the one presented in Equations 2.37 or 2.38.

$$q_{oh} = e^{-\zeta\omega_n t}\left[C_1 sin\left(\sqrt{1-\zeta^2}\omega_n t\right) + C_2 cos\left(\sqrt{1-\zeta^2}\omega_n t\right)\right] \tag{2.37}$$

$$q_{oh} = Ae^{-\zeta\omega_n t} sin\left(\sqrt{1-\zeta^2}\omega_n t\right) + \phi \tag{2.38}$$

In which C_1, C_2, A and ϕ are constants, with $A = \sqrt{C_1^2 + C_2^2}$, $\phi = arctg\left(\frac{C_2}{C_1}\right)$ and $\omega_{nd} = \omega_n\sqrt{1-\zeta^2}$ being the natural damped frequency.

Considering the inputs presented in the previous section, in Figures 15, 16 and 17 below it is possible to observe the general forms of the temporal responses of the second order system for a pulse, a step and a ramp excitation, respectively. The effects of the variation of the value of the damping factor in each of them can also be noted.

Figure 15 – Second order system response to pulse input.

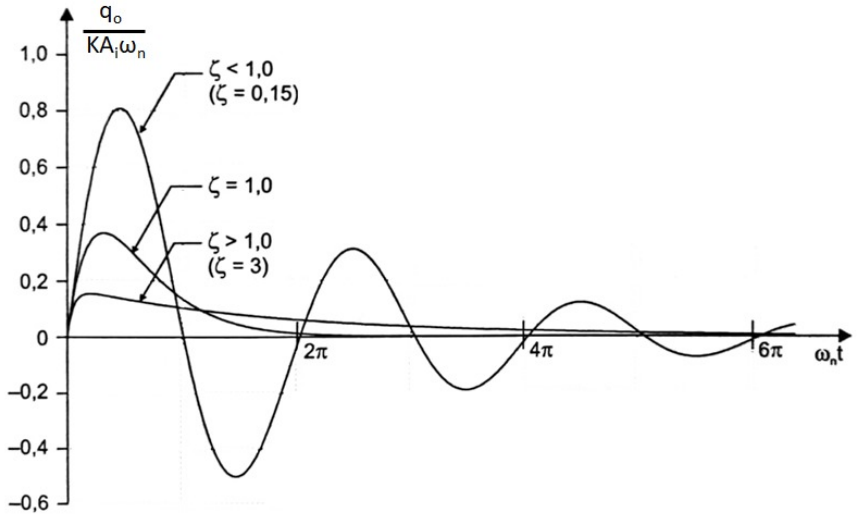

Source: Addapted from Felicio (2010).

Figure 16 – Second order system response to step input.

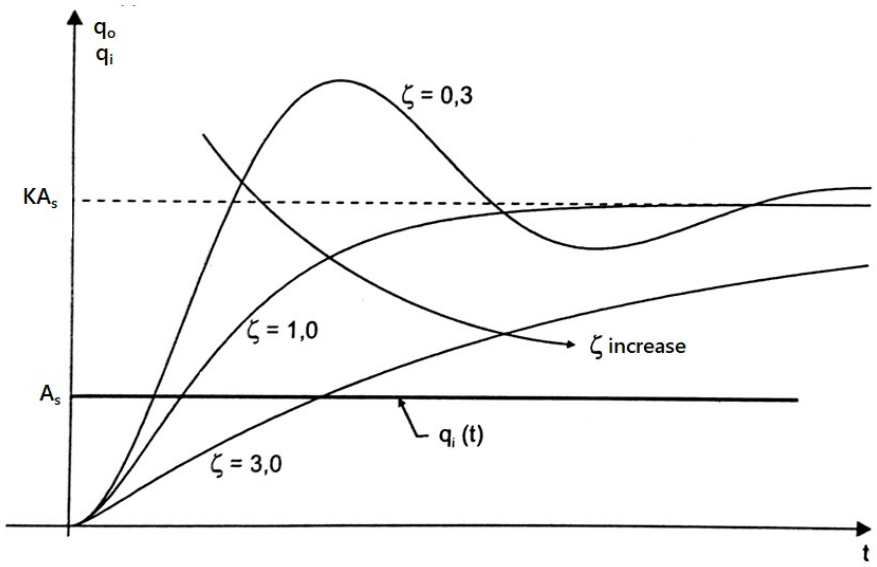

Source: Addapted from Felicio (2010).

It is possible to observe that the lower the damping factor, the greater the oscillations. For $\zeta > 1$ there are no more oscillations. Finally, for a pulse input, the final response value tends to zero.

It can also be seen that the lower the damping factor, the greater the oscillation and consequently the overshoot. For $\zeta > 1$ there is no more overshoot and the answer approaches an exponential. It is also worth mentioning that if there were no ζ - that is, if it were null - the system would vibrate indefinitely in its natural frequency (ω_n). If the K gain is unitary, the final output value will be the amplitude A_s of the input.

It can be seen that the output q_o tends to a straight line as long as time tends to infinity,

Figure 17 – Second order system response to ramp input.

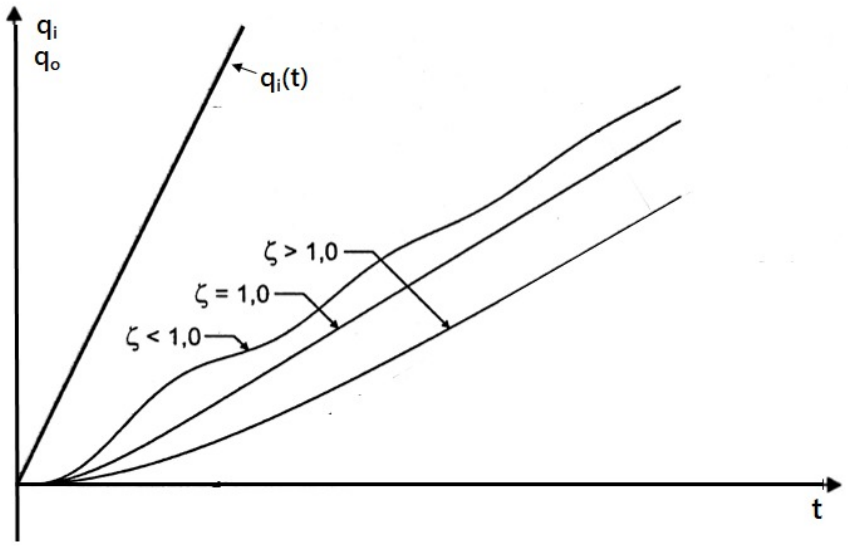

Source: Addapted from Felicio (2010).

whose slope will be parallel to the input if the gain $K = 1$.

2.5 Frequency response

Let be a dynamic system defined by Equation 2.39:

$$TF(D) = \frac{q_o(t)}{q_i(t)} \tag{2.39}$$

In which the input q_i is defined by Equation 2.24. Considering a stable system, the output function, at the steady state, will have the form expressed in Equation 2.40.

$$q_o(t) = A_o sin(\omega t + \phi) \tag{2.40}$$

A system subjected to a sinusoidal excitation will have as steady state response also a sinusoidal signal of same frequency as the input (SPERANZA, 2016). The amplitude (A_o) and angle (phase ϕ) of the output signal are, in general, different from the input signal as shown in Figure 18

The sinusoidal TF of any system is achieved replacing the D of Equation 2.25 with $i\omega$, resulting in Equation 2.41. $i\omega$ is a complex variable and can be represented by magnitude and phase, taking as parameter the frequency. If the phase is negative, that means there is a phase delay, but if it is positive, there is a phase advance (FELICIO, 2010).

$$\frac{q_o}{q_i}(i\omega) = \frac{k}{\left[1 - \left(\frac{\omega}{\omega_n}\right)^2\right] + i\left[\frac{2\zeta\omega}{\omega_n}\right]} \tag{2.41}$$

Figure 18 – Superposition of the output and input of the system

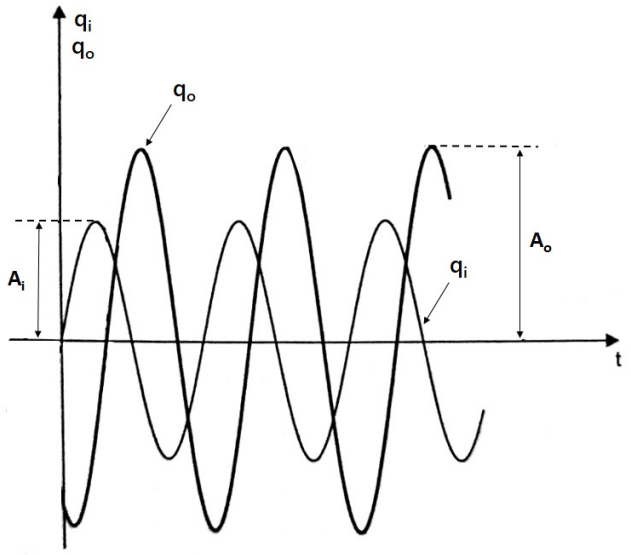

Source: Addapted from Felicio (2010).

Calculating the module and the phase of this complex function, we obtain Equations 2.42 and 2.43. The representation of a sinusoidal TF submitted to a sinusoidal input is a graph of the module (magnitude) by the excitation frequency and a graph of the phase by the same frequency. Both graphs are represented in Figure 19.

$$\frac{A_o}{A_i} = \left|\frac{q_o}{q_i}(i\omega)\right| = \frac{k}{\sqrt{\left[1-\left(\frac{\omega}{\omega_n}\right)^2\right]^2 + \left[2\zeta\left(\frac{\omega}{\omega_n}\right)\right]^2}} \tag{2.42}$$

$$\phi = -arctg\frac{2\zeta\left(\frac{\omega}{\omega_n}\right)}{1-\left(\frac{\omega}{\omega_n}\right)^2} \tag{2.43}$$

The standard representation of the module and phase is done on logarithmic scale, in order to allow the multiplication of the TF terms to be converted into a sum, thus providing the elaboration of the so-called Bode diagrams. The magnitude unit is obtained in decibel [dB] and that of the phase in degrees (D'AZZO; HOUPIS, 1995).

In second order systems, for $\zeta < 0.707$ the graph of the amplitude relations has a peak. The frequency at which this peak occurs is called the peak frequency ω_p and is defined by Equation 2.44. The peak frequency has the same value as the resonance ω_r frequency of the system (FELICIO, 2010).

$$\omega_p = \omega_n\sqrt{1-2\zeta^2},\ para\ \zeta < 0,707 \tag{2.44}$$

Figure 19 – Normalized frequency response for a second order system

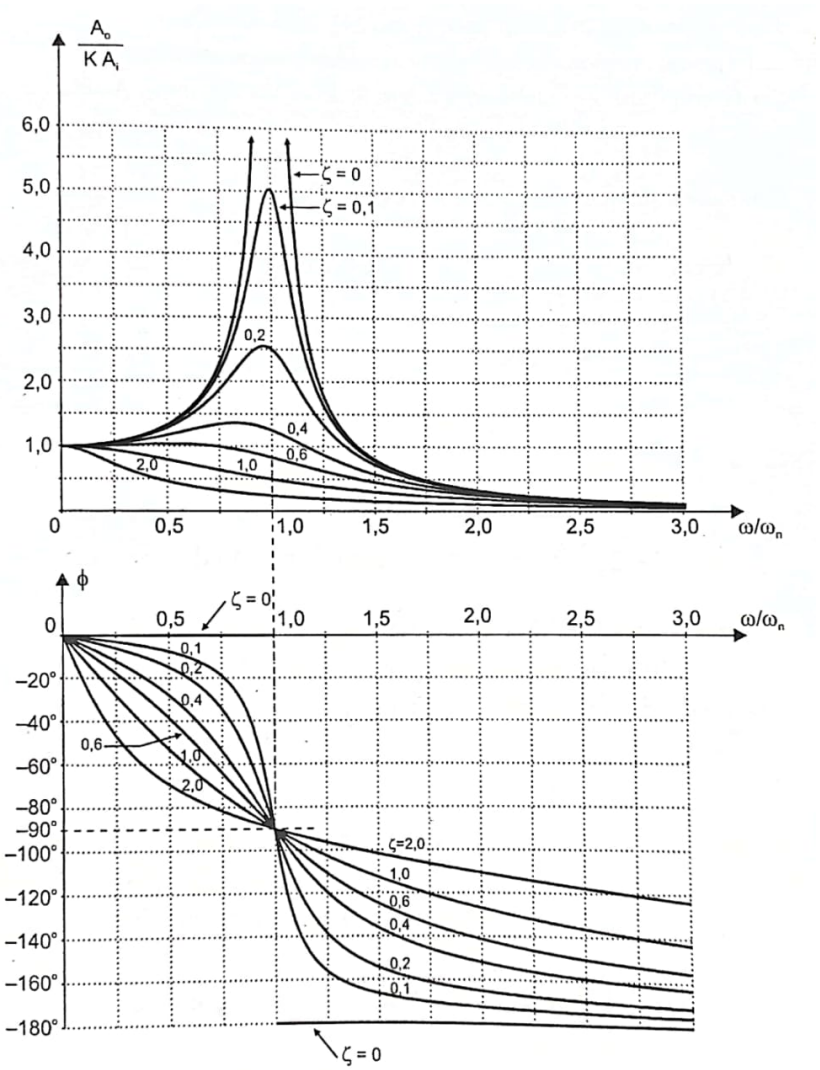

Source: Addapted from Felicio (2010).

2.6 Stability analysis

In mechanical terms an object is in stable equilibrium if, when pushed, it returns to its original position after the momentum ceases, as shown in the Figure 20a. It is unstable as the one shown in Figure 20b if, after being pushed, its position is unknown. A system is considered stable if, when subjected to a pulse input, for example, the output tends to zero as time tends to infinity. It will be unstable if the output tends to infinity as time tends to infinity. It is also possible that the output tends neither to zero nor to infinity but to a finite value other than zero, thus being considered critically stable (CASTRUCCI et al., 2011).

A common method for studying the stability of a system is the analysis of its poles and zeros. A system TF can, in general, be represented by Equation 2.45, or in simplified form by Equation 2.46.

$$TF(s) = \frac{k(s^m + a_{m-1}s^{m-1} + a_{m-2}s^{m-2} + ... + a_1 s + a_0)}{s^n + b_{n-1}s^{n-1} + b_{n-2}s^{n-2} + ... + b_1 s + b_0} \tag{2.45}$$

Figure 20 – Stability of a system

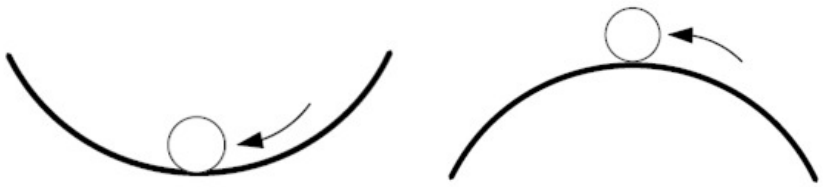

(a) Stable system (b) Unstable system

Source: Addapted from Ogata (2010).

$$TF(s) = \frac{K(s+z_1)(s+z_2)...(s+z_m)}{(s+p_1)(s+p_2)...(s+p_n)} \tag{2.46}$$

The n poles are the roots of the denominator of the TF ($-p_1, -p_2, ..., -p_n$), while the zeros are the roots of the TF numerator ($-z_1, -z_2, ..., -z_m$). The constant K defines system's gain .

Zeros are the values of s for which the transfer function is zero. The poles are the values of s for which the transfer function is infinite, that is, they make the denominator become zero. Poles and zeros can be complex or real quantities. When a system is described in the form of state space, the poles will be the eigenvalues of the matrix of states A of Equation 2.18 (OGATA, 2010). In general, they can be written as show in Equation 2.47.

$$s = \sigma \pm j\omega \tag{2.47}$$

In which σ is the real part of the pole or zero and $j\omega$ is the complex part of the pole or zero. The poles and zeros of a TF can be represented on a pole and zeros diagram. In Figure 21 the two-dimensional graph, known as s plane, is represented (FRANKLIN et al., 2002).

Figure 21 – Example of a s plane

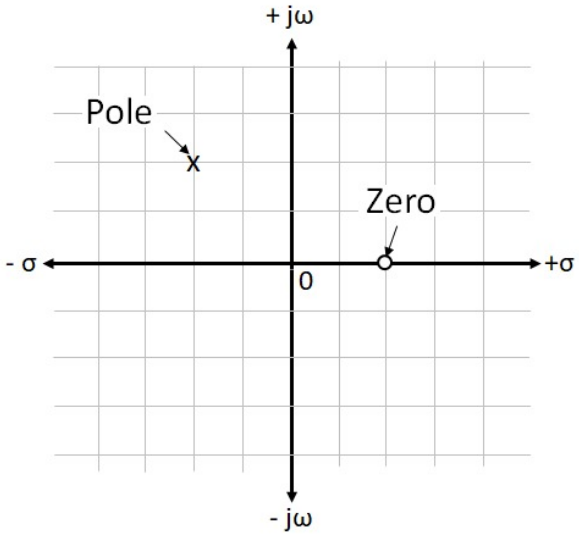

Source: Addapted from Franklin et al. (2002).

Poles are usually indicated with an x and zeros with an o. Poles or zeros in the left half planes of the graph are all negative; poles or zeros in the right semi-plane are positive. The stability of the system can be determined by the position of the poles in s plane.

If any pole is in the real positive part of the s plane, the system will be unstable. If all poles have the negative real part, the system will be stable, and if any pole is totally imaginary, the system will be critically stable. If there are poles with the complex part, the output will have an oscillatory characteristic (DORF; MBIHOP, 2013). All of these combinations can be accessed in Table 1.

Table 1 – Stability analysis based on the poles values

Pole		**System Status**
Real part	**Complexe part**	
+	+	Unstable
+	-	Unstable
+	0	Unstable
-	+	Stable
-	-	Stable
-	0	Stable
0	+	Critically stable
0	-	Critically stable
0	0	Critically stable

Source: Addapted from Dorf e Mbihop (2013).

3 Materials and Methods

This chapter presents the dynamic modeling of AGVs considering half of each vehicle analyzed. The vertical displacements of the suspension and of the load were determined as the outputs to be investigated, as well as the angle of rotation of the load in relation to its gravitational center. Inputs were considered in the form of displacements imposed to the wheels, simulating obstacles in the path of AGVs. In addition, the models were made in a generalized way, allowing the use for different configurations of the same AGV model only changing the initial data. the initial hypotheses presented in the previous chapter were adopted for all models, providing the simplifications needed.

3.1 Four-wheels AGV

The four-wheel AGV is a unit load one. As previously mentioned, the selected model has four identical driving wheels. The vehicle reference was that of the HOOGEWIJS (2020) prototype.

3.1.1 Dynamic model

Adopting the suspension module shown in Figure 2 and the modeling of full vehicle (DARUS; SAM, 2009) and a quarter of a vehicle (DARUS; ENZAI, 2010), the diagram representing the mechanical system shown in Figure 22 was drafted.

Figure 22 – Four-wheel AGV diagram

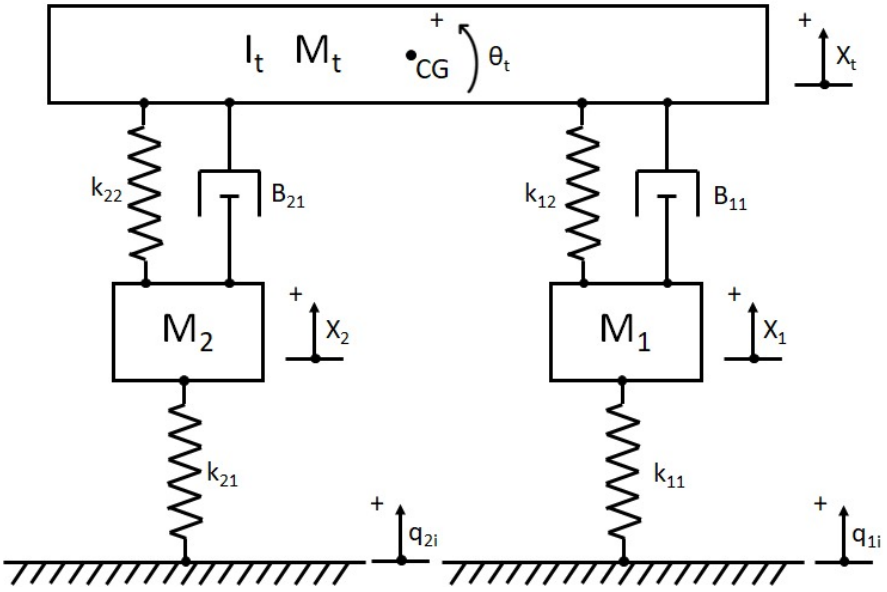

Source: Author.

The two inputs (q_{i_1} and q_{i_2}) were defined as one for each wheel. Given the distance between the axes and the speed of the vehicle, it is expected a time lag between them, even though they are identical. The mass M_t represents half of the total mass (the mass of the chassis plus the mass of the load carried). I_t is the moment of inertia of the loaded vehicle, while masses M_1 and M_2 are the for the suspensions. Having this in hand, for modeling according to Rao (2009), Equation 2.1 is applied to the masses M_1, M_2 and M_t and Equation 2.2 for the moment of inertia I_t. From the free-body diagram in Figure 23, the resulting equations are written as it follows.

Figure 23 – Four-wheel AGV - free-body diagrams

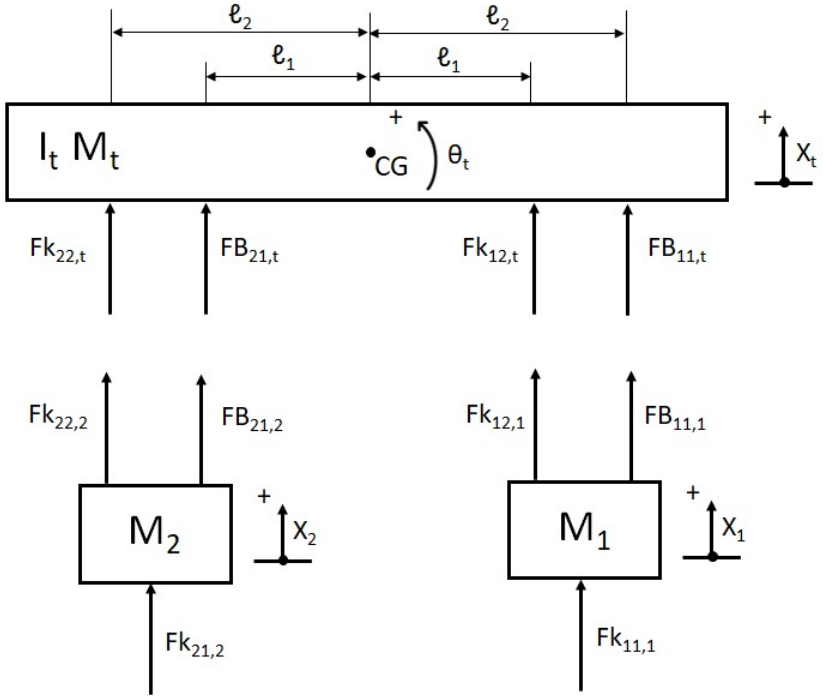

Source: Author.

For the mass M_1, the sum of forces at the x direction is given by Equation 3.1.

$$\sum F_x = M_1 \ddot{x_1} = F_{k_{11,1}} + F_{k_{12,1}} + F_{B_{11,1}} \tag{3.1}$$

Since the springs and dampers are linear, the forces acting on mass one are those of Equations 3.2 to 3.4. The angle θ_t contributes to forces with a displacement - a negative one for the forces to the left of the CG and a positive one to the right of the CG. The contribution will be of the order of $tg\theta_t$ times the distance between the CG and the application of the force. However, given the initial hypotheses of small deformations, the system can be linearized by adopting θ_t small enough so that $tg\theta_t \approx \theta_t$.

$$F_{k_{11,1}} = -k_{11}\left(x_1 - q_{i_1}\right) \tag{3.2}$$

$$F_{k_{12,1}} = -k_{12}\left(x_1 - \left(x_t + tg\theta_t l_1\right)\right) \tag{3.3}$$

$$F_{B_{11,1}} = -B_{11}\left(\dot{x_1} - (\dot{x_t} + tg\dot{\theta_t}l_2)\right) \tag{3.4}$$

Analogously to the development for mass M_1, Equations 3.5 to 3.8 are obtained for mass M_2.

$$\sum F_x = M_2\ddot{x_2} = F_{k_{21,2}} + F_{k_{22,2}} + F_{B_{21,2}} \tag{3.5}$$

$$F_{k_{21,2}} = -k_{21}\left(x_2 - q_{i_2}\right) \tag{3.6}$$

$$F_{k_{22,2}} = -k_{22}\left(x_2 - (x_t - tg\theta_t l_2)\right) \tag{3.7}$$

$$F_{B_{21,2}} = -B_{21}\left(\dot{x_2} - (\dot{x_t} - tg\dot{\theta_t}l_1)\right) \tag{3.8}$$

For the mass M_t (Equation 3.9) and moment of inertia I_t (Equation 3.10), the forces involved are the same, Equations 3.11 to 3.14. Once more the positioning of the force in relation to the CG will define its sign of the momentum generated: negative to the left and positive to the right.

$$\sum F_x = M_t\ddot{x_t} = F_{k_{22,t}} + F_{k_{12,t}} + F_{B_{11,t}} + F_{B_{21,t}} \tag{3.9}$$

$$\sum M_z = I_t\ddot{\theta_t} = -F_{k_{22,t}}l_2 + F_{k_{12,t}}l_1 + F_{B_{11,t}}l_2 - F_{B_{21,t}}l_1 \tag{3.10}$$

$$F_{k_{12,t}} = -k_{12}\left((x_t + tg\theta_t l_1) - x_1\right) \tag{3.11}$$

$$F_{B_{11,t}} = -B_{11}\left((\dot{x_t} + tg\dot{\theta_t}l_2) - \dot{x_1}\right) \tag{3.12}$$

$$F_{k_{22,t}} = -k_{22}\left((x_t - tg\theta_t l_2) - x_2\right) \tag{3.13}$$

$$F_{B_{21,t}} = -B_{21}\left((\dot{x_t} - tg\dot{\theta_t}l_1) - \dot{x_2}\right) \tag{3.14}$$

Writing the equations obtained in matrix form - as shown in Equation 3.15 - the mass matrix M, the stiffness matrix k and the damping matrix B, defined respectively in Equations 3.16, 3.18 and 3.17 are obtained.

$$M\begin{bmatrix}\ddot{x_1}\\ \ddot{x_2}\\ \ddot{x_t}\\ \ddot{\theta_t}\end{bmatrix} = B\begin{bmatrix}\dot{x_1}\\ \dot{x_2}\\ \dot{x_t}\\ \dot{\theta_t}\end{bmatrix} + k\begin{bmatrix}x_1\\ x_2\\ x_t\\ \theta_t\end{bmatrix} + \begin{bmatrix}k_{11} & 0\\ 0 & k_{21}\\ 0 & 0\\ 0 & 0\end{bmatrix}\begin{bmatrix}q_{i_1}\\ q_{i_2}\end{bmatrix} \tag{3.15}$$

$$M = \begin{bmatrix} M_1 & 0 & 0 & 0 \\ 0 & M_2 & 0 & 0 \\ 0 & 0 & M_1 & 0 \\ 0 & 0 & 0 & I_t \end{bmatrix} \tag{3.16}$$

$$B = \begin{bmatrix} -B_{11} & 0 & B_{11} & B_{11}l_2 \\ 0 & -B_{21} & B_{21} & -B_{21}l_1 \\ B_{11} & B_{21} & -B_{11} - B_{21} & -B_{11}l_2 + B_{21}l_1 \\ B_{11}l_2 & -B_{21}l_1 & -B_{11}l_2 + B_{21}l_1 & -B_{11}l_2^2 - B_{21}l_1^2 \end{bmatrix} \tag{3.17}$$

$$k = \begin{bmatrix} -k_{11} - k_{12} & 0 & k_{12} & k_{12}l_1 \\ 0 & -k_{21} - k_{22} & k_{22} & -k_{22}l_2 \\ k_{12} & k_{22} & -k_{22} - k_{12} & -k_{12}l_1 + k_{22}l_2 \\ k_{12}l_1 & -k_{22}l_2 & k_{22}l_2 - k_{12}l_1 & -k_{12}l_1^2 - k_{22}l_2^2 \end{bmatrix} \tag{3.18}$$

Given the complexity of the system found, to obtain the model TFs, the system will be written in the form of a state space.

3.1.2 State space

For the implementation of the state space, eight states were selected, being them the four outputs and their respective velocities. This is shown by the vector of Equation 3.19 and the derivative thereof in the vector of Equation 3.20. The outputs are listed in the vector of Equation 3.21 and the inputs in the vector of Equation 3.22.

$$x = \begin{bmatrix} x_1 & x_2 & x_t & \theta_t & \dot{x_1} & \dot{x_2} & \dot{x_t} & \dot{\theta}_t \end{bmatrix}^T \tag{3.19}$$

$$\dot{x} = \begin{bmatrix} \dot{x_1} & \dot{x_2} & \dot{x_t} & \dot{\theta}_t & \ddot{x_1} & \ddot{x_2} & \ddot{x_t} & \ddot{\theta}_t \end{bmatrix}^T \tag{3.20}$$

$$y = \begin{bmatrix} x_1 & x_2 & x_t & \theta_t \end{bmatrix}^T \tag{3.21}$$

$$u = \begin{bmatrix} q_{i_1} & q_{i_2} \end{bmatrix}^T \tag{3.22}$$

Thus, to obtain the system proposed in Equation 2.18, based on the equations defined on the chapter before, the state (A), input (B), output (C) and feed forward (D) matrices are then

assembled and shown in Equations 3.23 to 3.27. Because the system has no control loop, the matrix D is null.

$$A = \begin{bmatrix} 0 & 0 & 0 & 0 & 1 & 0 & 0 & 0 \\ 0 & 0 & 0 & 0 & 0 & 1 & 0 & 0 \\ 0 & 0 & 0 & 0 & 0 & 0 & 1 & 0 \\ 0 & 0 & 0 & 0 & 0 & 0 & 0 & 1 \\ \frac{-k_{11}-k_{12}}{M_1} & 0 & \frac{k_{12}}{M_1} & a & \frac{-B_{11}}{M_1} & 0 & \frac{B_{11}}{M_1} & b \\ 0 & \frac{-k_{21}-k_{22}}{M_2} & \frac{k_{22}}{M_2} & c & 0 & \frac{-B_{21}}{M_2} & \frac{B_{21}}{M_2} & d \\ \frac{k_{12}}{M_t} & \frac{k_{22}}{M_t} & \frac{-k_{22}-k_{12}}{M_t} & e & \frac{B_{11}}{M_t} & \frac{B_{21}}{M_t} & \frac{-B_{11}-B_{21}}{M_t} & f \\ \frac{k_{12}l_1}{I_t} & \frac{-k_{22}l_2}{I_t} & \frac{k_{22}l_2-k_{12}l_1}{I_t} & g & \frac{B_{11}l_2}{I_t} & \frac{-B_{21}l_1}{I_t} & \frac{-B_{11}l_2+B_{21}l_1}{I_t} & h \end{bmatrix} \tag{3.23}$$

$$\begin{aligned} a &= \tfrac{k_{12}l_1}{M_1} & b &= \tfrac{B_{11}l_2}{M_1} \\ c &= \tfrac{-k_{22}l2}{M_2} & d &= \tfrac{-B_{21}l_1}{M_2} \\ e &= \tfrac{k_{22}l_2-k_{12}l_1}{M_t} & f &= \tfrac{-B_{11}l_2+B_{21}l_1}{M_t} \\ g &= \tfrac{-k_{22}l_2^2-k_{12}l_1^2}{I_t} & h &= \tfrac{-B_{11}l_2^2-B_{21}l_1^2}{I_t} \end{aligned} \tag{3.24}$$

$$B = \begin{bmatrix} 0 & 0 \\ 0 & 0 \\ 0 & 0 \\ 0 & 0 \\ \frac{k_{11}}{M_1} & 0 \\ 0 & \frac{k_{21}}{M_2} \\ 0 & 0 \\ 0 & 0 \end{bmatrix} \tag{3.25}$$

$$C = \begin{bmatrix} 1 & 0 & 0 & 0 & 0 & 0 & 0 & 0 \\ 0 & 1 & 0 & 0 & 0 & 0 & 0 & 0 \\ 0 & 0 & 1 & 0 & 0 & 0 & 0 & 0 \\ 0 & 0 & 0 & 1 & 0 & 0 & 0 & 0 \end{bmatrix} \tag{3.26}$$

$$D = \begin{bmatrix} 0 & 0 \\ 0 & 0 \\ 0 & 0 \\ 0 & 0 \end{bmatrix} \tag{3.27}$$

For the solution of the state space, computational tools from MATLAB are employed.

3.2 Forklift AGV

The stacking AGV has a similar model to that of 4 wheels. The main change will be the displacement of the gravitational center, as in this case the load is on the forks at the front of the vehicle and not centralized in relation to the wheels (LARSSON T.J. AND et al., 2003).

3.2.1 Dynamic model

The system diagram, presented in Figure 24, was assembled in order to reconsider the chassis mass together with the transported mass, in order to consider that, during the simulation, the forklift would have its forks in a fixed position. This is necessary because if the forks move along the horizontal displacement of the AGV, the system would no longer be invariant. The free-body diagrams made having these considerations in mind are shown in Figure 25.

Figure 24 – Forklift AGV diagram

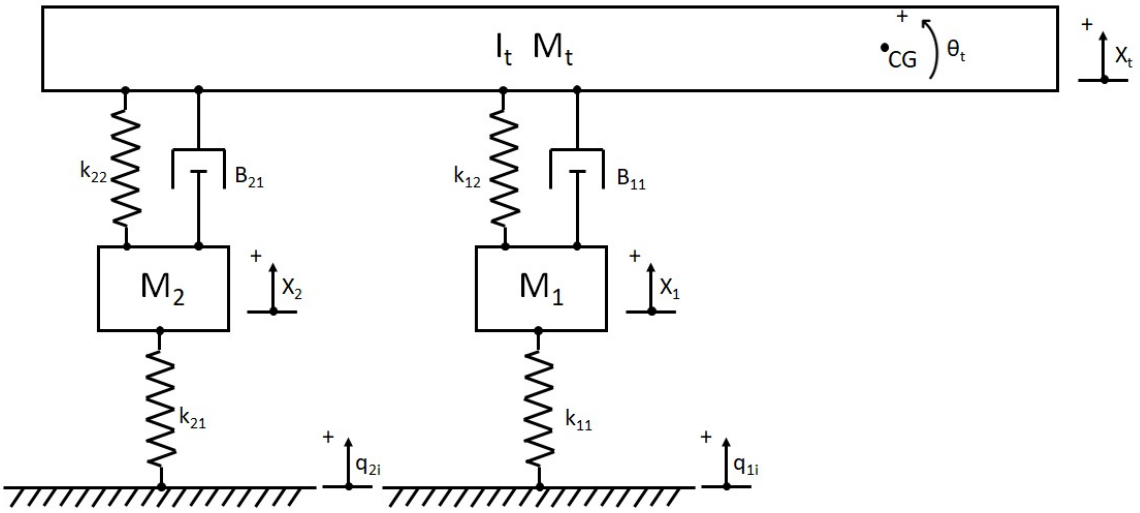

Source: Author.

Having this established, regarding the previous model, the sum of forces will be the same for translation, but not for rotation. However, the description of the forces involved undergo some changes, and the new forces are expressed in the Equations 3.28 to 3.33.

$$F_{k_{12,1}} = -k_{12}\left(x_1 - (x_t - tg\theta_t l_2)\right) \tag{3.28}$$

$$F_{B_{11,1}} = -B_{11}\left(\dot{x_1} - (\dot{x_t} - tg\dot{\theta_t} l_1)\right) \tag{3.29}$$

$$F_{k_{12,t}} = -k_{12}\left((x_t - tg\theta_t l_2) - x_1\right) \tag{3.30}$$

$$F_{B_{11,t}} = -B_{11}\left((\dot{x_t} - tg\dot{\theta_t} l_1) - \dot{x_1}\right) \tag{3.31}$$

Figure 25 – Forklift AGV - free-body diagrams

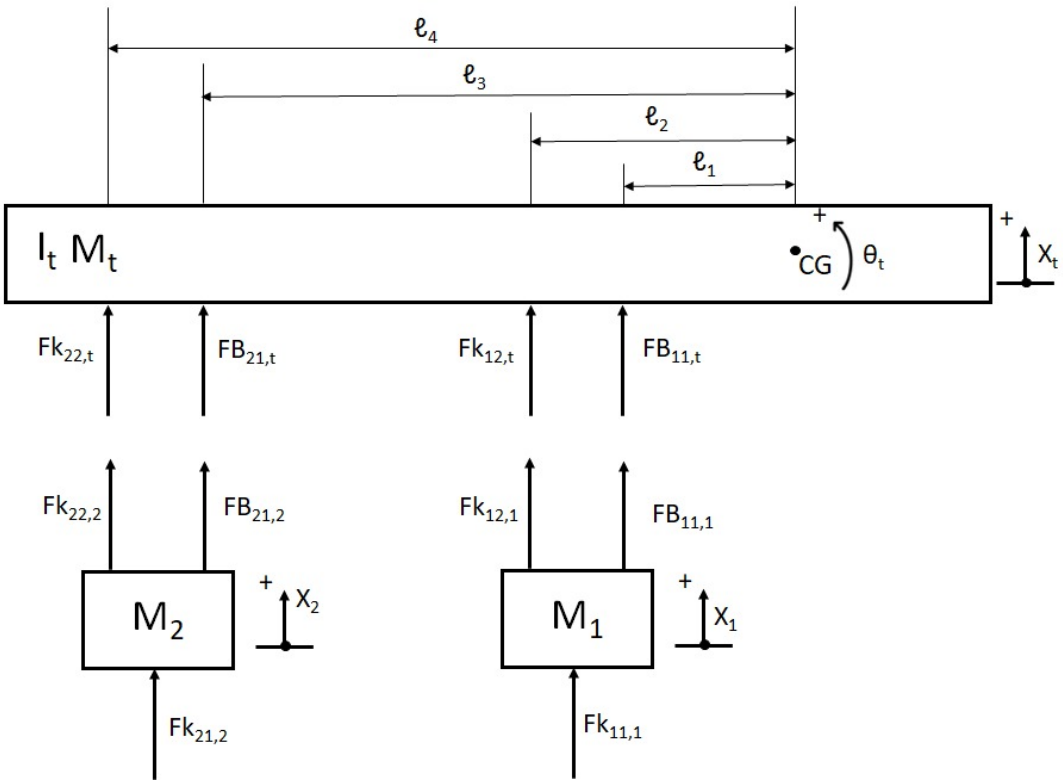

Source: Author.

$$F_{k_{22,t}} = -k_{22}\left((x_t - tg\theta_t l_4) - x_2\right) \tag{3.32}$$

$$F_{B_{21,t}} = -B_{21}\left((\dot{x_t} - tg\dot{\theta_t} l_3) - \dot{x_2}\right) \tag{3.33}$$

Likewise, the sum of the moments changes and it is represented by Equation 3.34. Now, all the forces cause a negative moment in relation to the CG.

$$I_t\ddot{\theta_t} = -F_{k_{22,t}} l_4 - F_{k_{12,t}} l_2 - F_{B_{11,t}} l_1 - F_{B_{21,t}} l_3 \tag{3.34}$$

The system in the matrix form, after being linearized, will be identical to that of Equation 3.15. The matrices of mass M, damping B and stiffness k for this model are presented in equations 3.35, 3.36 and 3.37, respectively.

$$M = \begin{bmatrix} M_1 & 0 & 0 & 0 \\ 0 & M_2 & 0 & 0 \\ 0 & 0 & M_1 & 0 \\ 0 & 0 & 0 & I_t \end{bmatrix} \tag{3.35}$$

$$B = \begin{bmatrix} -B_{11} & 0 & B_{11} & -B_{11}l_1 \\ 0 & -B_{21} & B_{21} & -B_{21}l_3 \\ B_{11} & B_{21} & -B_{11} - B_{21} & B_{11}l_1 + B_{21}l_3 \\ -B_{11}l_1 & -B_{21}l_3 & B_{11}l_1 + B_{21}l_3 & -B_{11}l_1^2 - B_{21}l_3^2 \end{bmatrix} \tag{3.36}$$

$$k = \begin{bmatrix} -k_{11} - k_{12} & 0 & k_{12} & -k_{12}l_2 \\ 0 & -k_{21} - k_{22} & k_{22} & -k_{22}l_4 \\ k_{12} & k_{22} & -k_{22} - k_{12} & k_{12}l_2 + k_{22}l_4 \\ -k_{12}l_2 & -k_{22}l_4 & k_{22}l_4 + k_{12}l_2 & -k_{12}l_2^2 - k_{22}l_4^2 \end{bmatrix} \tag{3.37}$$

Again, the system requires the use of state space to obtain all TFs of the model.

3.2.2 State space

The state, outputs and inputs vectors are identical to the four-wheel AGV. Changes appear in the state space matrices, more specifically in the state matrix, being the other three the same as in the previous model. The new matrix of states A is presented in Equation 3.38 with some elements of the matrix detailed in Equation 3.39.

$$A = \begin{bmatrix} 0 & 0 & 0 & 0 & 1 & 0 & 0 & 0 \\ 0 & 0 & 0 & 0 & 0 & 1 & 0 & 0 \\ 0 & 0 & 0 & 0 & 0 & 0 & 1 & 0 \\ 0 & 0 & 0 & 0 & 0 & 0 & 0 & 1 \\ \frac{-k_{11}-k_{12}}{M_1} & 0 & \frac{k_{12}}{M_1} & a & \frac{-B_{11}}{M_1} & 0 & \frac{B_{11}}{M_1} & b \\ 0 & \frac{-k_{21}-k_{22}}{M_2} & \frac{k_{22}}{M_2} & c & 0 & \frac{-B_{21}}{M_2} & \frac{B_{21}}{M_2} & d \\ \frac{k_{12}}{M_t} & \frac{k_{22}}{M_t} & \frac{-k_{22}-k_{12}}{M_t} & e & \frac{B_{11}}{M_t} & \frac{B_{21}}{M_t} & \frac{-B_{11}-B_{21}}{M_t} & f \\ \frac{-k_{12}l_1}{I_t} & \frac{-k_{22}l_2}{I_t} & \frac{k_{22}l_2+k_{12}l_1}{I_t} & g & \frac{-B_{11}l_2}{I_t} & \frac{-B_{21}l_1}{I_t} & \frac{B_{11}l_2+B_{21}l_1}{I_t} & h \end{bmatrix} \tag{3.38}$$

$$\begin{aligned} a &= \tfrac{-k_{12}l_2}{M_1} & b &= \tfrac{-B_{11}l_1}{M_1} \\ c &= \tfrac{-k_{22}l_4}{M_2} & d &= \tfrac{-B_{21}l_3}{M_2} \\ e &= \tfrac{k_{22}l_4+k_{12}l_2}{M_t} & f &= \tfrac{B_{11}l_1+B_{21}l_3}{M_t} \\ g &= \tfrac{-k_{22}l_4^2-k_{12}l_2^2}{I_t} & h &= \tfrac{-B_{11}l_1^2-B_{21}l_3^2}{I_t} \end{aligned} \tag{3.39}$$

3.3 Six wheels AGV

The six-wheel AGV is of the same unit load model as the 4-wheel AGV, but, as previously mentioned, only the pair of central wheels will be motor. In theory, this model is used to allow the use of only two engines without many losses in the movement.

3.3.1 Dynamic model

This model presents one more input variable and one more output variable, precisely because of the postponement of the third suspension module, as can be seen in Figure 26. The equations are analogous to the others, but again, the additional module adds one more equation. The direction of forces, displacements and angular velocities in relation to the gravitational center must always be maintained according to the sign convention.

Figure 26 – Six-wheel AGV diagram

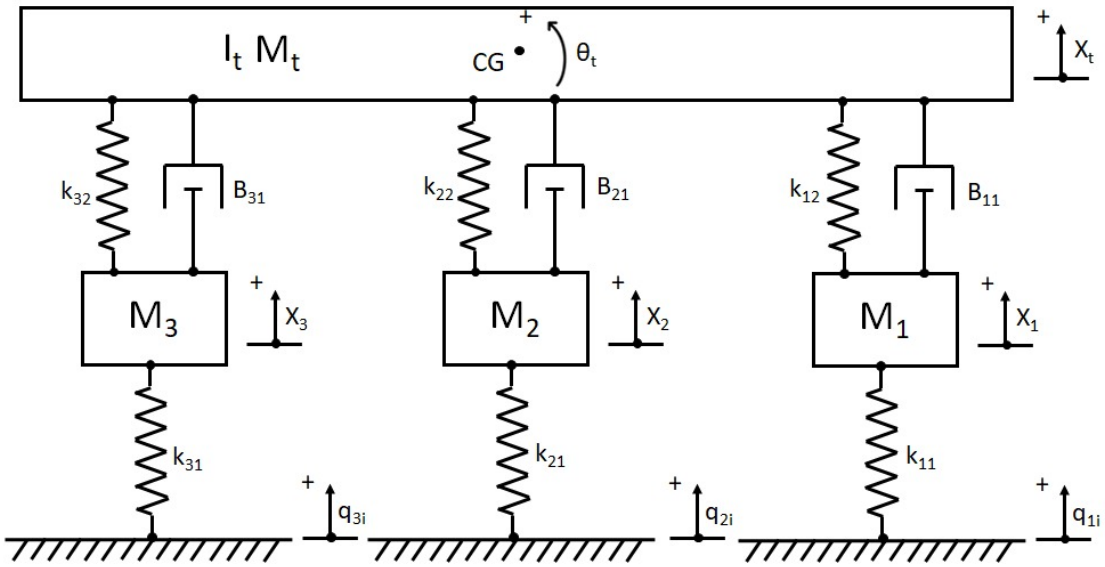

Source: Author.

From the free-body diagrams, shown in Figure 27, it is confirmed that equations for masses M_1 and M_2 will be piratically the same as for the models in section 3.1.

In terms of masses, a few forces have some details changed: the force of dumpers B_{11} and B_{21}, and the forces of springs F_{12} and FB_{22}. All this is shown in Equations 3.40 to 3.43.

$$F_{k_{12,1}} = -k_{12}\left(x_1 - (x_t - tg\theta_t l_2)\right) \tag{3.40}$$

$$F_{B_{11,1}} = -B_{11}\left(\dot{x_1} - (\dot{x_t} - tg\dot{\theta}_t l_3)\right) \tag{3.41}$$

$$F_{k_{22,2}} = -k_{22}\left(x_2 - (x_t - tg\theta_t l_1)\right) \tag{3.42}$$

Figure 27 – Six-wheel AGV - free-body diagrams

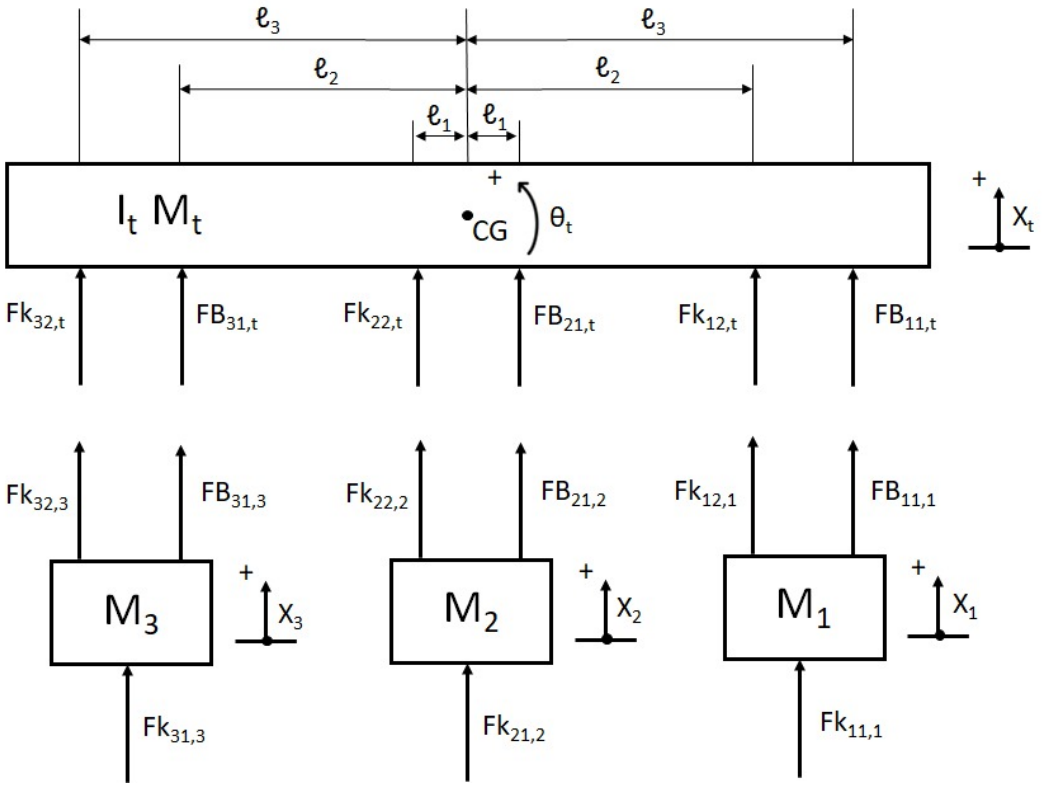

Source: Author.

$$F_{B_{21,2}} = -B_{21}\left(\dot{x_2} - (\dot{x_t} + tg\dot{\theta_t}l_1)\right) \tag{3.43}$$

Analogously to the equation of mass M_2 in both previous models, the equation of mass M_3 is shown in Equations 3.44 to 3.47.

$$\sum F_x = M_3\ddot{x_3} = F_{k_{31,3}} + F_{k_{32,3}} + F_{B_{31,3}} \tag{3.44}$$

$$F_{k_{31,3}} = -k_{31}\left(x_3 - q_{i_3}\right) \tag{3.45}$$

$$F_{k_{32,3}} = -k_{32}\left(x_3 - (x_t - tg\theta_t l_3)\right) \tag{3.46}$$

$$F_{B_{31,3}} = -B_{31}\left(\dot{x_1} - (\dot{x_t} - tg\dot{\theta_t}l_2)\right) \tag{3.47}$$

In equations 3.48 to 3.55, the sum of forces for the mass M_t and the moments for I_tt are presented, as well as the description of all spring and dampers forces involved.

$$M_t\ddot{x_t} = F_{k_{12,t}} + F_{k_{22,t}} + F_{k_{32,t}} + F_{B_{11,t}} + F_{B_{21,t}} + F_{B_{31,t}} \tag{3.48}$$

$$I_t\ddot{\theta_t} = F_{k_{12,t}}l_2 - F_{k_{22,t}}l_1 - F_{k_{32,t}}l_3 + F_{B_{11,t}}l_3 + F_{B_{21,t}}l_1 - F_{B_{31,t}}l_2 \tag{3.49}$$

$$F_{k_{12,t}} = -k_{12}\left((x_t + tg\theta_t l_2) - x_1\right) \tag{3.50}$$

$$F_{B_{11,t}} = -B_{11}\left((\dot{x_t} + tg\dot{\theta_t} l_3) - \dot{x_1}\right) \tag{3.51}$$

$$F_{k_{22,t}} = -k_{22}\left((x_t - tg\theta_t l_1) - x_2\right) \tag{3.52}$$

$$F_{B_{21,t}} = -B_{21}\left((\dot{x_t} + tg\dot{\theta_t} l_1) - \dot{x_2}\right) \tag{3.53}$$

$$F_{k_{32,t}} = -k_{32}\left((x_t - tg\theta_t l_3) - x_3\right) \tag{3.54}$$

$$F_{B_{31,t}} = -B_{31}\left((\dot{x_t} - tg\dot{\theta_t} l_2) - \dot{x_3}\right) \tag{3.55}$$

After linearizing the system, by the hypothesis of small displacements, all equations were written in matrix form, which allows the obtaining of Equation 3.56. The matrix of masses M, stiffness k and damping B are those shown in Equations 3.57, 3.59 and 3.58, respectively.

$$M\begin{bmatrix}\ddot{x_1}\\ \ddot{x_2}\\ \ddot{x_3}\\ \ddot{x_t}\\ \ddot{\theta_t}\end{bmatrix} = B\begin{bmatrix}\dot{x_1}\\ \dot{x_2}\\ \dot{x_3}\\ \dot{x_t}\\ \dot{\theta_t}\end{bmatrix} + k\begin{bmatrix}x_1\\ x_2\\ x_3\\ x_t\\ \theta_t\end{bmatrix} + \begin{bmatrix}k_{11} & 0 & 0\\ 0 & k_{21} & 0\\ 0 & 0 & k_{31}\\ 0 & 0 & 0\\ 0 & 0 & 0\end{bmatrix}\begin{bmatrix}q_{i_1}\\ q_{i_1}\\ q_{i_3}\end{bmatrix} \tag{3.56}$$

$$M = \begin{bmatrix}M_1 & 0 & 0 & 0 & 0\\ 0 & M_2 & 0 & 0 & 0\\ 0 & 0 & M_3 & 0 & 0\\ 0 & 0 & 0 & M_t & 0\\ 0 & 0 & 0 & 0 & I_t\end{bmatrix} \tag{3.57}$$

$$B = \begin{bmatrix}-B_{11} & 0 & 0 & B_{11} & B_{11}l_3\\ 0 & -B_{21} & 0 & B_{21} & B_{21}l_1\\ 0 & 0 & -B_{31} & B_{31} & -B_{31}l_2\\ B_{11} & B_{21} & B_{31} & -B_{11} - B_{21} - B_{31} & -B_{11}l_3 - B_{21}l_1 + B_{31}l_2\\ B_{11}l_3 & B_{21}l_1 & -B_{31}l_2 & -B_{11}l_3 - B_{21}l_1 + B_{31}l_2 & -B_{11}l_3^2 - B_{21}l_1^2 - B_{31}l_2^2\end{bmatrix} \tag{3.58}$$

$$k = \begin{bmatrix}-k_{11} - k_{12} & 0 & 0 & k_{12} & k_{12}l_2\\ 0 & -k_{21} - k_{22} & 0 & k_{22} & -k_{22}l_1\\ 0 & 0 & -k_{31} - k_{32} & k_{32} & -k_{32}l_3\\ k_{12} & -k_{22} & -k_{32} & a & b\\ k_{12}l_2 & -k_{22}l_1 & -k_{32}l_3 & c & d\end{bmatrix} \tag{3.59}$$

$$\begin{aligned} a &= -k_{12} - k_{22} - k_{32} \\ b &= -k_{12}l_2 + k_{22}l_1 + k_{32}l_3 \\ c &= -k_{12}l_2 + k_{22}l_1 + k_{32}l_3 \\ d &= -k_{12}l_2^2 - k_{22}l_1^2 - k_{32}l_3^2 \end{aligned} \tag{3.60}$$

The next step will be, then, to move the system to the state space in order to facilitate the determination of the TFs.

3.3.2 State space

Given the addition of an equation in the system, the states, inputs and outputs needed to be redefined. So the state vector, as in Equation 3.61, has now ten elements, the five outputs displacements and their respective velocities. The derivative of the state vector are presented in Equation 3.62.

$$x = \begin{bmatrix} x_1 & x_2 & x_3 & x_t & \theta_t & \dot{x_1} & \dot{x_2} & \dot{x_3} & \dot{x_t} & \dot{\theta_t} \end{bmatrix}^T \tag{3.61}$$

$$\dot{x} = \begin{bmatrix} \dot{x_1} & \dot{x_2} & \dot{x_3} & \dot{x_t} & \dot{\theta_t} & \ddot{x_1} & \ddot{x_2} & \ddot{x_3} & \ddot{x_t} & \ddot{\theta_t} \end{bmatrix}^T \tag{3.62}$$

The outputs will be the four linear displacements of the four masses and the angular displacement of the mass M_t, all represented in the vector of Equation 3.63.

$$y = \begin{bmatrix} x_1 & x_2 & x_3 & x_t & \theta_t \end{bmatrix}^T \tag{3.63}$$

The inputs are the displacements imposed on each wheel, with a delay from each other considering the distance between axes and the vehicle's speed. They are disposed in the vector of Equation 3.64.

$$u = \begin{bmatrix} q_{i_1} & q_{i_2} & q_{i_3} \end{bmatrix}^T \tag{3.64}$$

Based on Equation 2.18, the state (A), input (B), output (C) and feed forward (D) matrices are then assembled and shown in Equations 3.65 to 3.69. Note again, that as the system

do not have a control loop, matrix D is null.

$$A = \begin{bmatrix} 0 & 0 & 0 & 0 & 0 & 1 & 0 & 0 & 0 & 0 \\ 0 & 0 & 0 & 0 & 0 & 0 & 1 & 0 & 0 & 0 \\ 0 & 0 & 0 & 0 & 0 & 0 & 0 & 1 & 0 & 0 \\ 0 & 0 & 0 & 0 & 0 & 0 & 0 & 0 & 1 & 0 \\ 0 & 0 & 0 & 0 & 0 & 0 & 0 & 0 & 0 & 1 \\ \frac{-k_{11}-k_{12}}{M_1} & 0 & 0 & \frac{k_{12}}{M_1} & a & \frac{-B_{11}}{M_1} & 0 & 0 & \frac{B_{11}}{M_1} & b \\ 0 & \frac{-k_{21}-k_{22}}{M_2} & 0 & \frac{k_{22}}{M_2} & c & 0 & \frac{-B_{21}}{M_2} & 0 & \frac{B_{21}}{M_2} & d \\ 0 & 0 & \frac{-k_{31}-k_{32}}{M_3} & \frac{k_{32}}{M_3} & e & 0 & 0 & \frac{-B_{31}}{M_3} & \frac{B_{31}}{M_3} & f \\ \frac{k_{12}}{M_t} & \frac{k_{22}}{M_t} & \frac{k_{32}}{M_t} & g & h & \frac{B_{11}}{M_t} & \frac{B_{21}}{M_t} & \frac{B_{31}}{M_t} & i & j \\ \frac{k_{12}l_2}{I_t} & \frac{-k_{22}l_1}{I_t} & \frac{-}{k_{32}l_3}I_t & k & l & \frac{B_{11}l_3}{I_t} & \frac{B_{21}l_1}{I_t} & \frac{-B_{31}l_2}{I_t} & m & n \end{bmatrix} \tag{3.65}$$

$$\begin{array}{cc} a = \frac{k_{12}l_2}{M_1} & b = \frac{B_{11}l_3}{M_1} \\ c = \frac{k_{22}l_1}{M_2} & d = \frac{B_{21}l_1}{M_2} \\ e = \frac{k_{32}l_3}{M_3} & f = \frac{B_{31}l_2}{M_3} \\ g = \frac{-k_{12}-k_{22}-k_{32}}{M_t} & h = \frac{-k_{12}l_2+k_{22}l_1+k_{32}l_3}{M_t} \\ i = \frac{-B_{11}-B_{21}-B_{31}}{M_t} & j = \frac{-B_{11}l_3-B_{21}l_1+B_{31}l_2}{M_t} \\ k = \frac{-k_{12}l_2+k_{22}l_1+k_{32}l_3}{I_t} & l = \frac{-k_{12}l_2^2-k_{22}l_1^2-k_{32}l_3^2}{I_t} \\ m = \frac{-B_{11}l_3-B_{21}l_1+B_{31}l_2}{I_t} & n = \frac{-B_{11}l_3^2-B_{21}l_1^2-B_{31}l_2^2}{I_t} \end{array} \tag{3.66}$$

$$B = \begin{bmatrix} 0 & 0 & 0 \\ 0 & 0 & 0 \\ 0 & 0 & 0 \\ 0 & 0 & 0 \\ \frac{k_{11}}{M_1} & 0 & 0 \\ 0 & \frac{k_{21}}{M_2} & 0 \\ 0 & 0 & \frac{k_{31}}{M_3} \\ 0 & 0 & 0 \end{bmatrix} \tag{3.67}$$

$$C = \begin{bmatrix} 1 & 0 & 0 & 0 & 0 & 0 & 0 & 0 & 0 & 0 \\ 0 & 1 & 0 & 0 & 0 & 0 & 0 & 0 & 0 & 0 \\ 0 & 0 & 1 & 0 & 0 & 0 & 0 & 0 & 0 & 0 \\ 0 & 0 & 0 & 1 & 0 & 0 & 0 & 0 & 0 & 0 \\ 0 & 0 & 0 & 0 & 1 & 0 & 0 & 0 & 0 & 0 \end{bmatrix} \tag{3.68}$$

$$D = \begin{bmatrix} 0 & 0 & 0 \\ 0 & 0 & 0 \\ 0 & 0 & 0 \\ 0 & 0 & 0 \\ 0 & 0 & 0 \end{bmatrix} \tag{3.69}$$

3.4 Matlab and Simulink

From the state spaces obtained for each model, a code was executed in Matlab to obtain the responses in the domain of time, frequency and for the study of stability. The *ss* function was used to reach the state space, while *sys* function was applied for calculating the TFs. Finally, the *pzmap* functions were used for the pole map, *bode* for the Bode diagrams and *rlocus* for the location of the roots, both for each TF (DUKKIPATI, 2007). The full codes can be seen in Appendix A.

For the responses in time domain, models were elaborated in Simulink to facilitate the overlapping effect and the inputs lag. The model for four-wheels AGVs (unit load and forklift) is shown in Figure 28 - in the case for the step input; for the others inputs, only the source block is replaced.

Figure 28 – Simulink blocs diagrams for the four-wheels AGVs

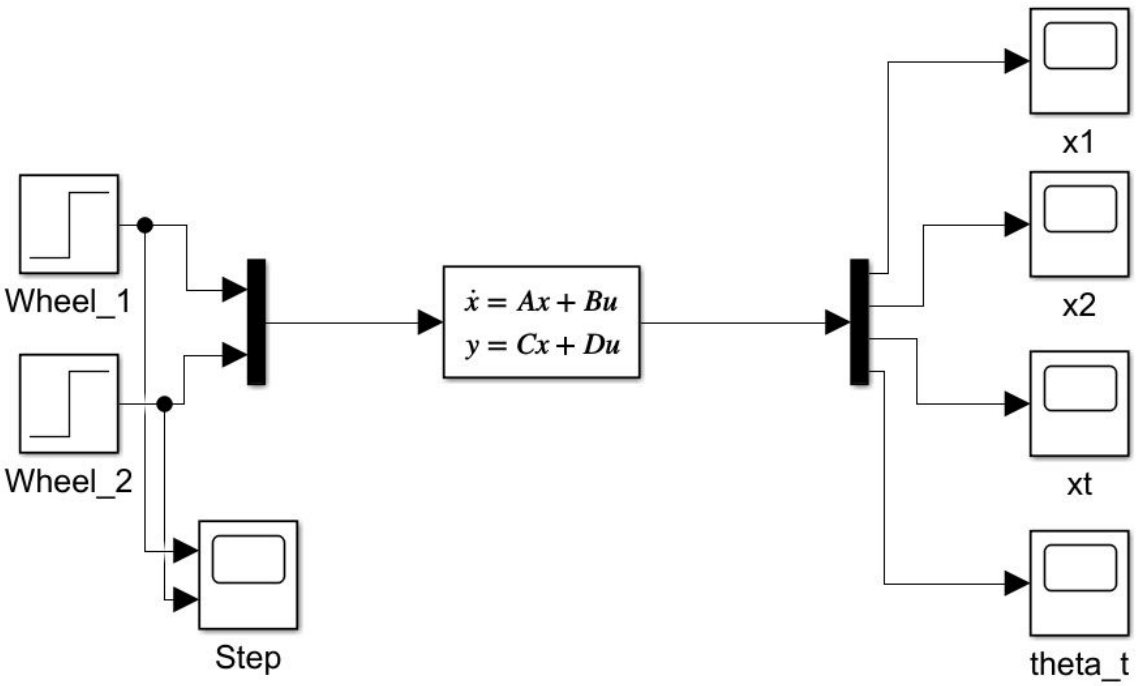

Source: Author.

For the six-wheels AGV, the standard model is, this time, made only for the pulse input. Provided by a combination of the step input with a derivative block, the bloc diagram is shown in Figure 29. With all tools ready, next step is to run the models and analyze the results.

Figure 29 – Simulink blocs diagrams for the six-wheels AGV

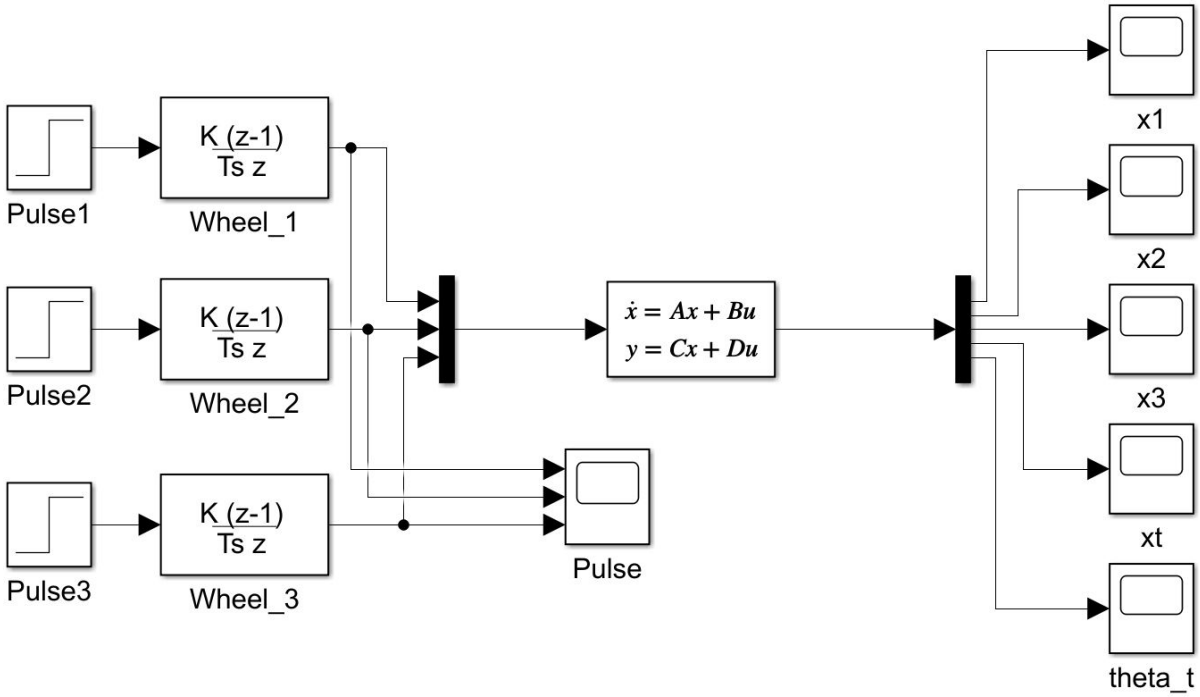

Source: Author.

4 Results and discussion

As the procedures described in Section 3 were applied for the three models, the present section is divided into three subsections, each for an analysis: in time, in frequency and stability. For the simulations, the initial data was extracted from the literature and estimated if it was not accessible. The main reference was the prototype developed by HOOGEWIJS (2020). For the other two models, catalogs from NKC-Kolec (2020) were used for dimensional and mass estimations. Some characteristics in common with the prototype were maintained, such as the damping and stiffness coefficients of the suspension modules. The initial data for the models are presented in Tables 2 to 4.

Table 2 – Four-wheels AGV parameters

M_1 [kg]	25
M_2 [kg]	25
M_c [kg]	100
M_l [kg]	500
M_t [kg]	300
I_t [kgm^2]	3.93
k_{11} [N/m]	1600
k_{21} [N/m]	1600
k_{12} [N/m]	1600
k_{22} [N/m]	1600
B_{11} [Ns/m]	460
B_{21} [Ns/m]	460
l_1 [m]	0.52
l_2 [m]	0.52
v [km/h]	5
Delay between wheels [s]	0.75

Source: Author.

As four-wheels AGVs that have all wheels powered have also the same mass. The same does not happen in the other models; in the AGV forklift, for example, the rear wheels are usually larger and therefore heavier. In the six-wheels AGV, the central pair of wheels are the motorized one, being then heavier than the others.

The delay between the entrance to the wheels was calculated in function of the speed and the wheelbase of the model. The speed of $5km/h$ was standardized for all simulations. The transport cargo was also standardized, to make the comparison between responses more visible. The moments of inertia were estimated based on the reference value obtained for the four-wheels AGV, considering the dimensions and masses of each model.

Although in the models the spring and dampers of the same suspension have different points of application, these points were adopted as the same, simplifying the calculations further

Table 3 – Forklift AGV parameters

M_1 [kg]	18
M_2 [kg]	25
M_c [kg]	240
M_l [kg]	500
M_t [kg]	370
I_t [kgm^2]	8.4
k_{11} [N/m]	1600
k_{21} [N/m]	1600
k_{12} [N/m]	1600
k_{22} [N/m]	1600
B_{11} [Ns/m]	460
B_{21} [Ns/m]	460
l_1 [m]	0.50
l_2 [m]	0.50
l_3 [m]	1.62
l_4 [m]	1.62
v [km/h]	5
Delay between wheels [s]	0.8

Source: Author.

Table 4 – Six-wheels AGV parameters

M_1 [kg]	20
M_2 [kg]	25
M_3 [kg]	20
M_c [kg]	180
M_l [kg]	500
M_t [kg]	340
I_t [kgm^2]	9.5
k_{11} [N/m]	1600
k_{21} [N/m]	1600
k_{31} [N/m]	1600
k_{12} [N/m]	1600
k_{22} [N/m]	1600
k_{32} [N/m]	1600
B_{11} [Ns/m]	460
B_{21} [Ns/m]	460
B_{31} [Ns/m]	460
l_1 [m]	0.0
l_2 [m]	0.8
l_3 [m]	0.8
v [km/h]	5
Delay between wheels 1 and 2 [s]	0.58
Delay between wheels 1 and 3 [s]	1.15

Source: Author.

more. In the case of the six-wheels AGV, this forces the suspension of the central wheel to do not act on the angular displacement of the total mass.

4.1 Time response

All inputs were created respecting each other's delays. The amplitudes were predefined at $A_s = 0.1$ m for the step, $A_p = 0.1$ m for the impulse and $A_r = 0.002$ m for the slope of the ramp. The amplitudes were defined thinking about more robust obstacles than those AGVs normally faces, precisely extrapolating the systems to more atypical scenarios and until then little explored. All images generated on the temporal responses have the time in seconds on the x axis; on the y axis, for linear displacements, the values are posed in meters, while for angular displacements the values are in radians.

4.1.1 Pulse

The first input analyzed was the pulse function. As presented in chapter 3, when a pulse input is applied on the system, the responses tend to oscillate around the initial condition - in these cases null. This is true for both angular and linear displacement. The pulses applied on the three models are shown in Figure 30.

Figure 30 – Pulse input forms for all the AGVs

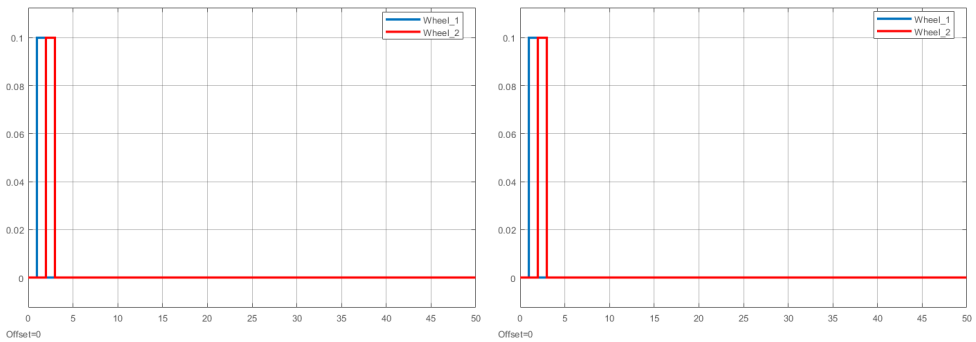

(a) Four-wheels AGV (b) Forklift AGV

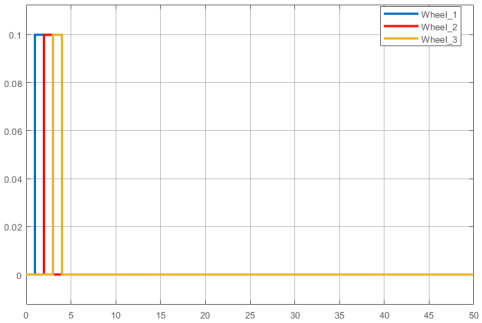

(c) Six-wheels AGV

Source: Author.

Figure 30a shows the pulse input in function of time for the four-wheels AGV, Figure 30b shows the pulse input in function of time for the forklift AGV and Figure 30c shows the pulse input in function of time for the six-wheels AGV.

The responses obtained for the four-wheel AGV are shown in Figure 31. As previously stated, all responses tend to zero, the initial condition value. However, after 50 seconds of simulation the suspension outputs continue to fluctuate considerably, which is expected, since the M_t mass had a settling time of 13.54 seconds, as shown in Table 5.

Figure 31 – Outputs of the four-wheels AGV for the pulse input.

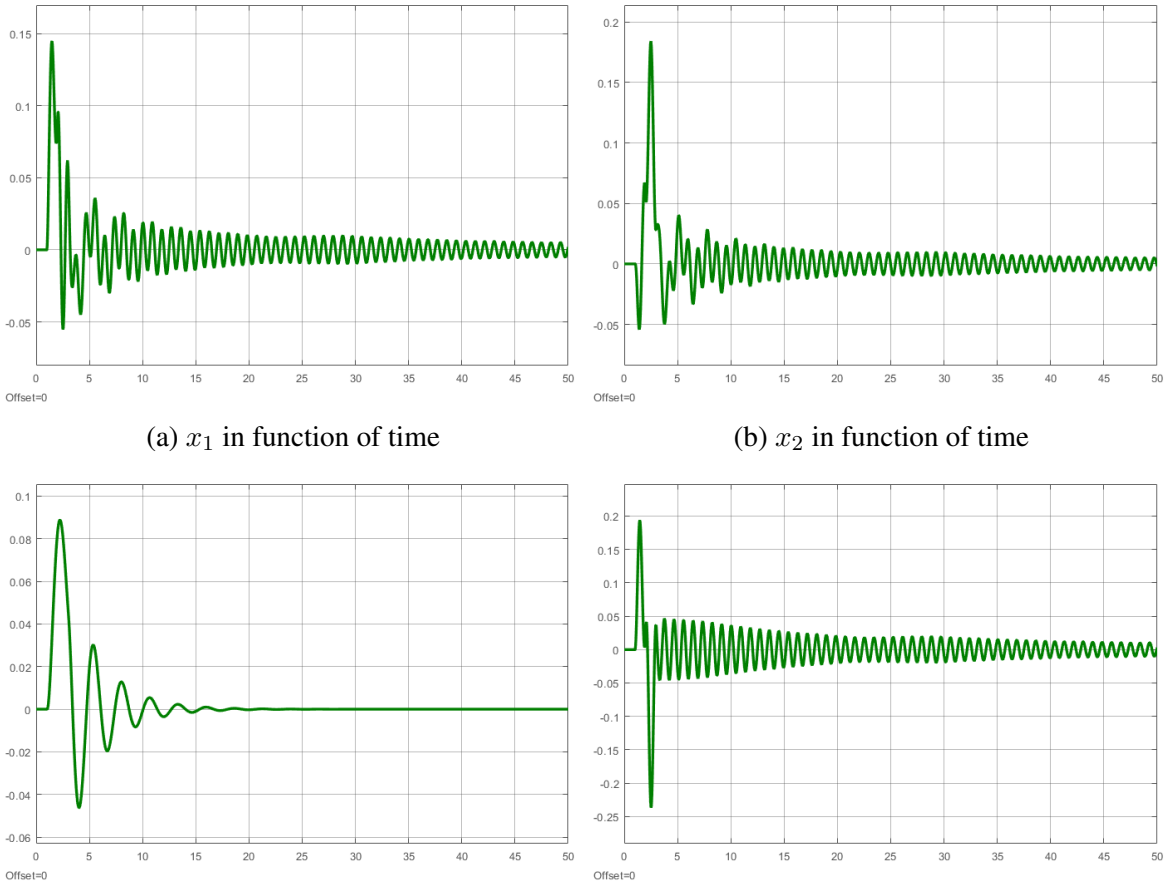

(a) x_1 in function of time

(b) x_2 in function of time

(c) x_t in function of time

(d) θ_t in function of time

Source: Author.

In Figure 31a, x_1 represents the linear displacement of the front wheel suspension in function of time. In Figure 31b, x_2 is the linear displacement of the rear wheel suspension in function of time. In Figure 31c, x_t is the linear displacement in function of time of the total mass of the loaded AGV and in Figure 31d, θ_t is the angular displacement in function of time of the total mass of the loaded AGV.

For θ_t the settling time is also greater than 50 seconds and the oscillations are very intense, at a value that although small, approximately 0.025 radians (or 1.43 degrees), not suitable depending on the type of load. Only θ_t had an overshoot. In the case of x_t it does not even occur, as the peak value is less than the pulse amplitude value. In general, the outputs are

Table 5 – Four-wheels AGV outputs parameters for the pulse input.

	x_t	θ_t
Delay time (t_d) [s]	1.63	1.216
Rise time (t_r) [s]	-	0.273
Peak time (t_p) [s]	2.208	2.525
Settling time (t_s) [s]	13.54	>50
Overshoot (M_p)	-	0.0471

Source: Author.

not particularly stable, but a damping increase could solve this problem.

Proceeding to the next model, the answers are plotted in Figure 32. The forklift AGV proved to be even less stable compared to the unit load with four wheels. The output x_2 oscillates with frequency and amplitude greater than x_1, showing that the rear wheels are more dynamically requested than the front ones. This is not exactly intuitive, since the load is closer to the front wheels.

Figure 32 – Outputs of the forklift AGV for the pulse input.

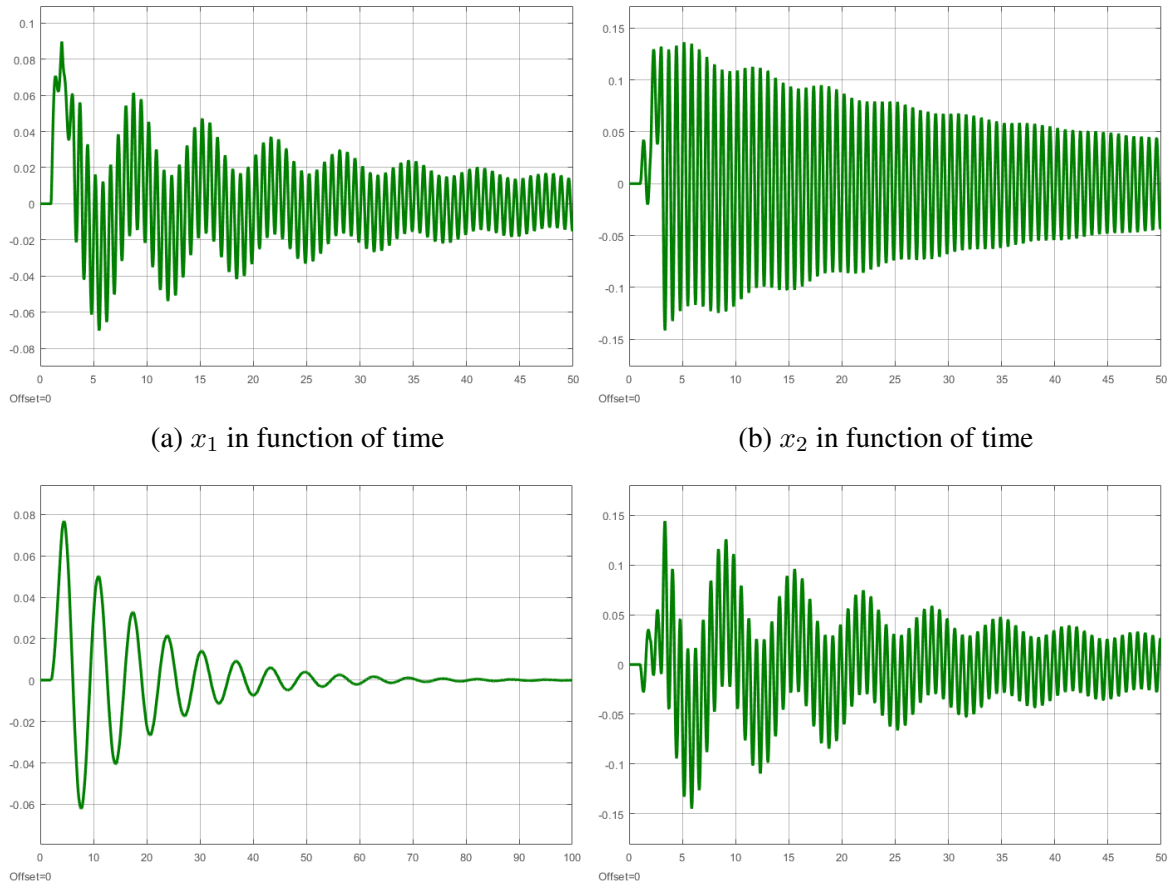

(a) x_1 in function of time

(b) x_2 in function of time

(c) x_t in function of time

(d) θ_t in function of time

Source: Author.

In Figure 32a, x_1 represents the linear displacement of the front wheel suspension in function of time. In Figure 32b, x_2 is the linear displacement of the rear wheel suspension in

function of time. In Figure 32c, x_t is the linear displacement in function of time of the total mass of the loaded AGV and in Figure 32d, θ_t is the angular displacement in function of time of the total mass of the loaded AGV.

The settling time for x_t is approximately 4.5 times that of the four-wheel AGV, as show in Table 6. θ_t did not present overshoot, but in general its value decreases more slowly over time, causing the fact that only after almost 50 seconds of simulation θ_t reaches the value of approximately 0.025 radians.

Table 6 – Forklift AGV outputs parameters for the pulse input.

	x_t	θ_t
Delay time (t_d) [s]	3.55	3.223
Rise time (t_r) [s]	-	-
Peak time (t_p) [s]	4.488	3.383
Settling time (t_s) [s]	59.8	>50
Overshoot (M_p)	-	-

Source: Author.

Finally, the responses for the latest model for a pulse input are shown in Figure 33. It is observed that considering distances of the CG of Table 4, the response of x_2 is more similar to that of x_t than to that of the other two wheels, which end up absorbing the obstacle more efficiently.

In Figure 33a, x_1 represents the linear displacement of the front wheel suspension in function of time. In Figure 33b, x_2 is the linear displacement of the center wheel suspension in function of time. In Figure 33c, x_3 is the linear displacement of the rear wheel suspension in function of time. In Figure 33d, x_t is the linear displacement in function of time of the total mass of the loaded AGV and in Figure 33e, θ_t is the angular displacement in function of time of the total mass of the loaded AGV.

With the addition of the third suspension in the partial model, the damping of the vehicle as a whole was increased. For this reason, the responses took a much more desired form, having the shortest settling time for θ_t and x_t, as shown in Table 7. However, because of its three inputs, θ_t showed the largest overshoot among the three models.

Table 7 – Six-wheels AGV outputs parameters for the pulse input.

	x_t	θ_t
Delay time (t_d) [s]	1,757	1,220
Rise time (t_r) [s]	-	0,215
Peak time (t_p) [s]	2,025	3,402
Settling time (t_s) [s]	11,15	37,37
Overshoot (M_p)	-	0,0617

Source: Author.

Figure 33 – Outputs of the six-wheels AGV for the pulse input.

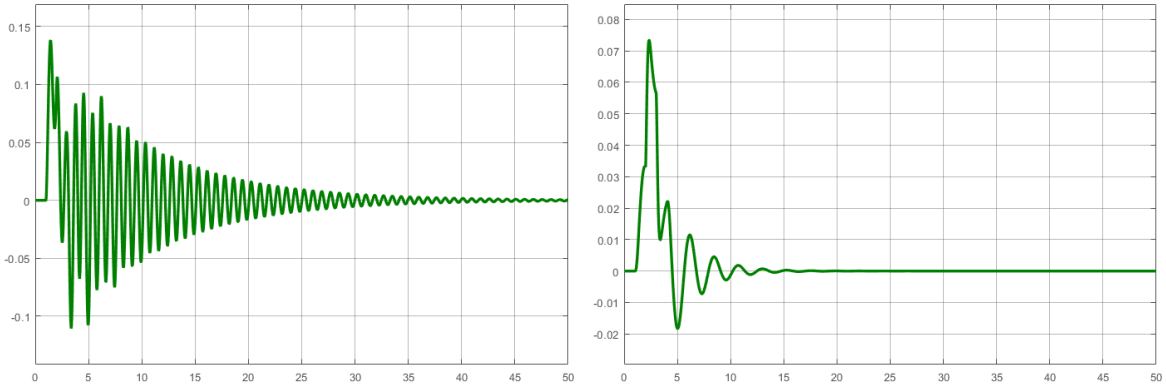

(a) x_1

(b) x_2

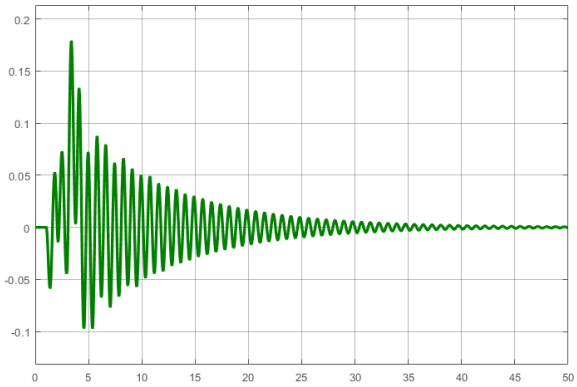

(c) x_3

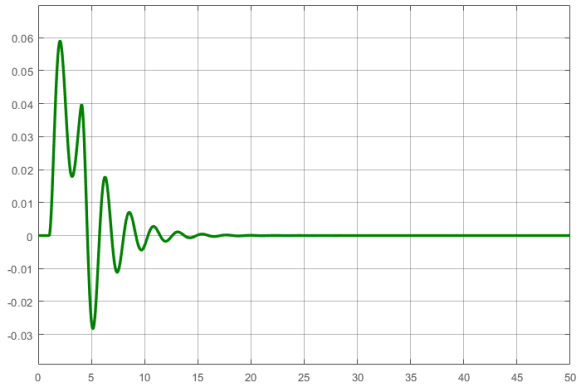

(d) x_t

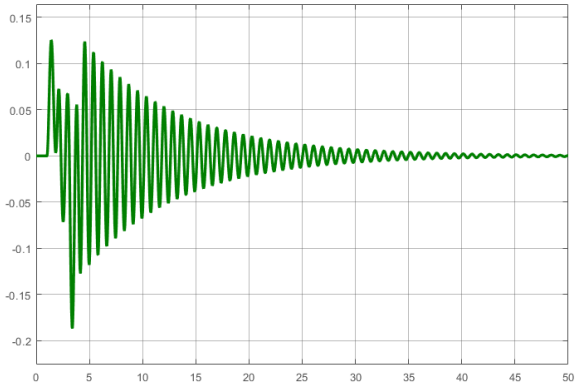

(e) θ_t

Source: Author.

4.1.2 Step

The next input studied is the step function, in which only the ascent was applied, as can be seen in Figure 34. Again, the gaps between the wheels and the speed of vehicles were considered, and the amplitude was A_s = 0.1 m, for all models. In the case of the step, the angular displacement will not stabilize in the amplitude of the input, but in the initial condition, because after a while with the two wheels on the step, the θ_t angle tends to zero again.

Figure 34 – Step input forms for all the AGVs

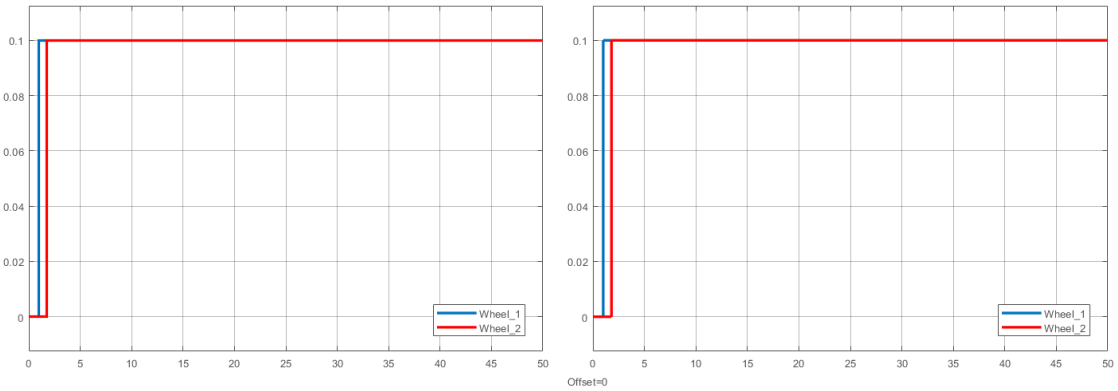

(a) Four-wheels AGV

(b) Forklift AGV

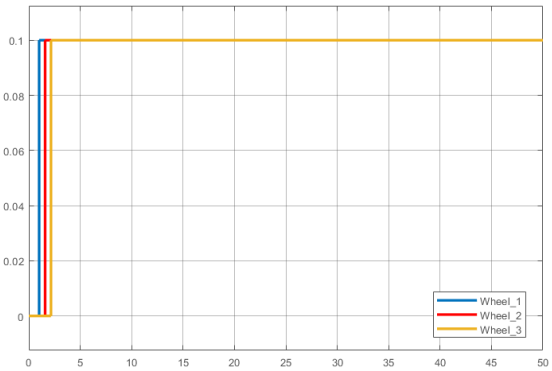

(c) Six-wheels AGV

Source: Author.

Figure 34a shows the step input in function of time for the four-wheels AGV, Figure 34b shows the step input in function of time for the forklift AGV and Figure 34c shows the step input in function of time for the six-wheels AGV.

The responses obtained for the four-wheel AGV are shown in Figure 35 below. For the step input, the four-wheel AVG showed better performance in comparison with the pulse, as seen by the differences in the settling time presented in Tables 5 and 8.

In Figure 35a, x_1 represents the linear displacement of the front wheel suspension in function of time. In Figure 35b, x_2 is the linear displacement of the rear wheel suspension in function of time. In Figure 35c, x_t is the linear displacement in function of time of the total mass of the loaded AGV and in Figure 35d, θ_t is the angular displacement in function of time of the total mass of the loaded AGV.

A reduction in overshoots and also in the amplitude of the oscillations shows that the system, in general, responds better to a step than to a pulse, even if the settling times are still high, bringing up again the choice of dampers.

Again for the forklift AGV, the responses are slower and with greater oscillations and amplitudes as shown in Figure 36. The rear suspension undergoes to more intense oscillations, proving that in fact the model requires two different suspensions, one for the rear wheels and

Figure 35 – Outputs of the four-wheels AGV for the step input.

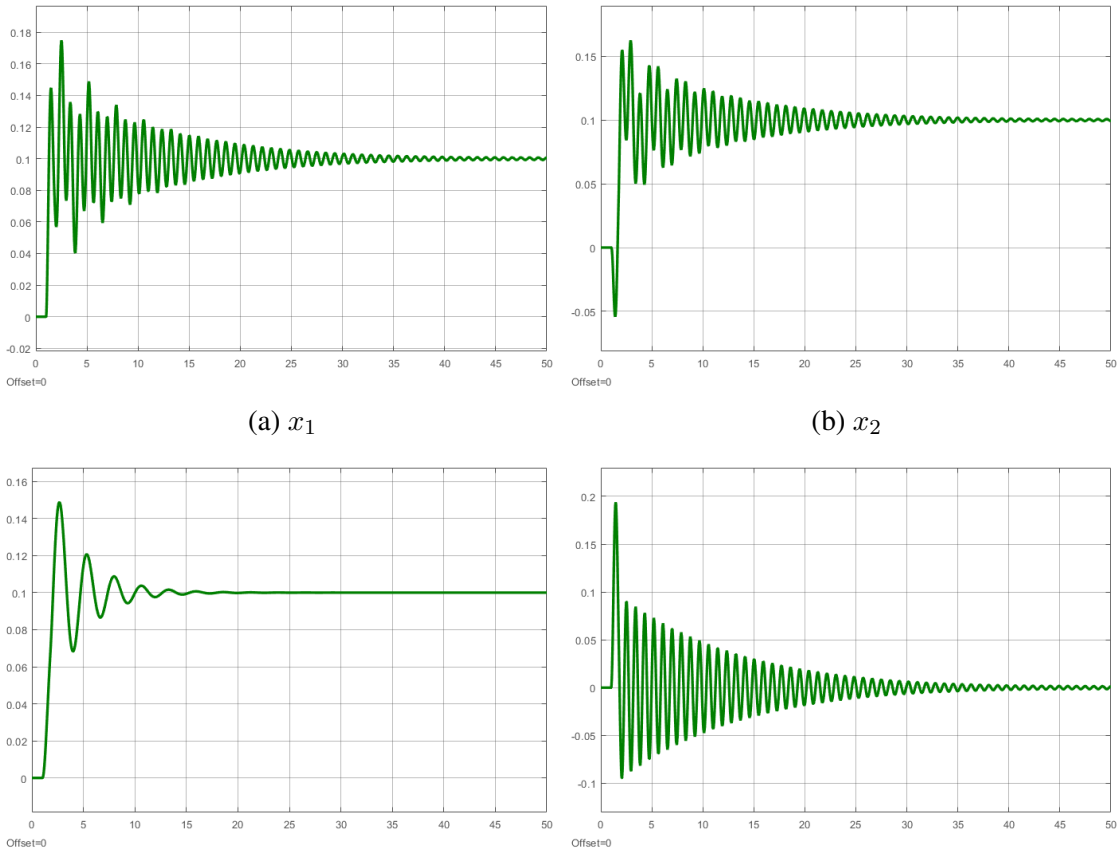

(a) x_1 (b) x_2

(c) x_t (d) θ_t

Source: Author.

Table 8 – Four-wheels AGV outputs parameters for the step input.

	x_t	θ_t
Delay time (t_d) **[s]**	1.62	1.256
Rise time (t_r) **[s]**	0.751	0.0308
Peak time (t_p) **[s]**	2.685	1.453
Settling time (t_s) **[s]**	13.66	30.19
Overshoot (M_p)	0.0452	0.0039

Source: Author.

one for the front.

In Figure 36a, x_1 represents the linear displacement of the front wheel suspension in function of time. In Figure 36b, x_2 is the linear displacement of the rear wheel suspension in function of time. In Figure 36c, x_t is the linear displacement in function of time of the total mass of the loaded AGV and in Figure 36d, θ_t is the angular displacement in function of time of the total mass of the loaded AGV.

If compared to the other four-wheeled AGV, again the settling times are approximately five times greater for x_t, as can be seen in Table 9. This means load is in motion much longer, putting it more at risk of falling, breaking or suffering any damage.

The six-wheeled AGV again proved to be the most stable of all for the load, as can be

Figure 36 – Outputs of the forklift AGV for the step input.

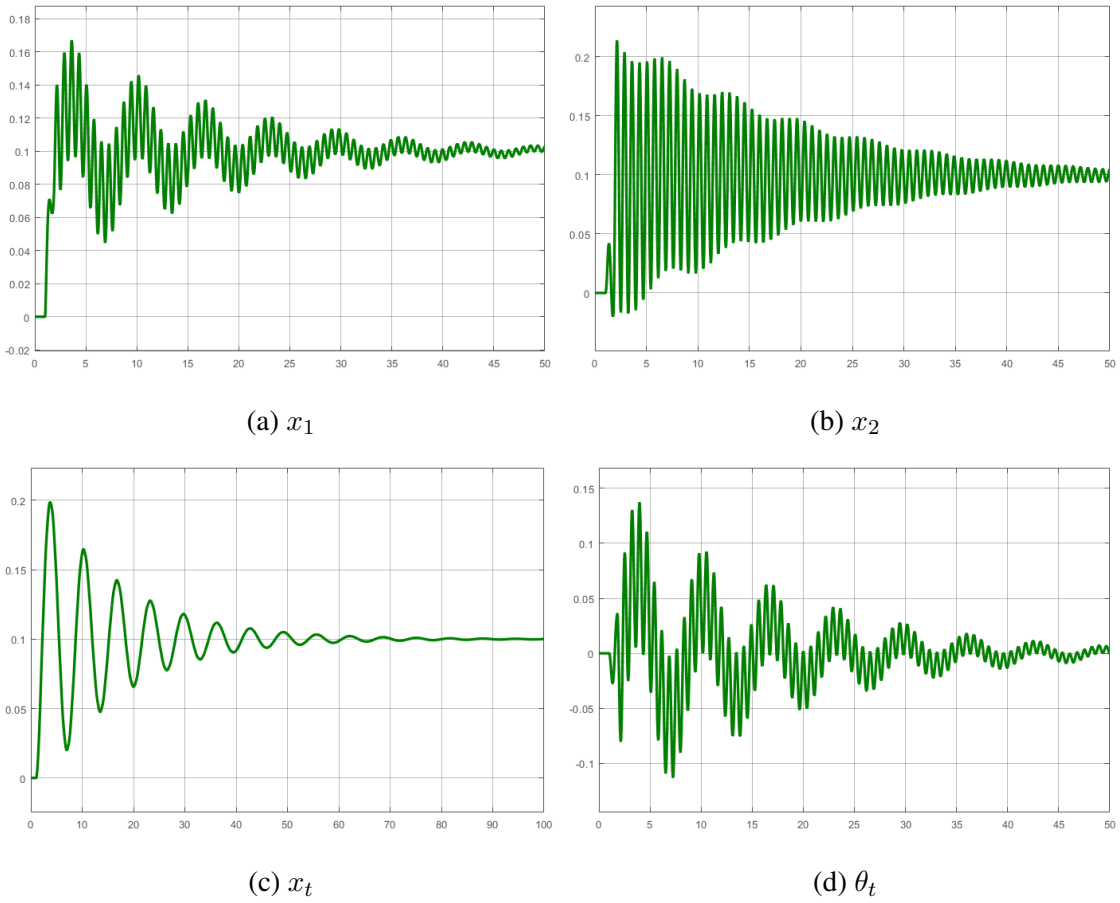

(a) x_1 (b) x_2

(c) x_t (d) θ_t

Source: Author.

Table 9 – Forklift AGV outputs parameters for the step input.

	x_t	θ_t
Delay time (t_d) [s]	1.806	2.485
Rise time (t_r) [s]	0.826	-
Peak time (t_p) [s]	3.73	3.962
Settling time (t_s) [s]	62.52	>50
Overshoot (M_p)	0.0986	-

Source: Author.

seen in Figure 37. The vehicle's higher damping causes the amplitude of oscillations to decrease more quickly, resulting in a faster settling time for x_t in particular of only 8.764 seconds. For θ_t, the value is 32.06 seconds; even if lower in relation to the forklift model that exceeds 50 seconds, it is subtly higher than the four-wheels. All parameters are shown in Table 10.

In Figure 37a, x_1 represents the linear displacement of the front wheel suspension in function of time. In Figure 37b, x_2 is the linear displacement of the center wheel suspension in function of time. In Figure 37c, x_3 is the linear displacement of the rear wheel suspension in function of time. In Figure 37d, x_t is the linear displacement in function of time of the total mass of the loaded AGV and in Figure 37e, θ_t is the angular displacement in function of time of the total mass of the loaded AGV.

Figure 37 – Outputs of the six-wheels AGV for the step input.

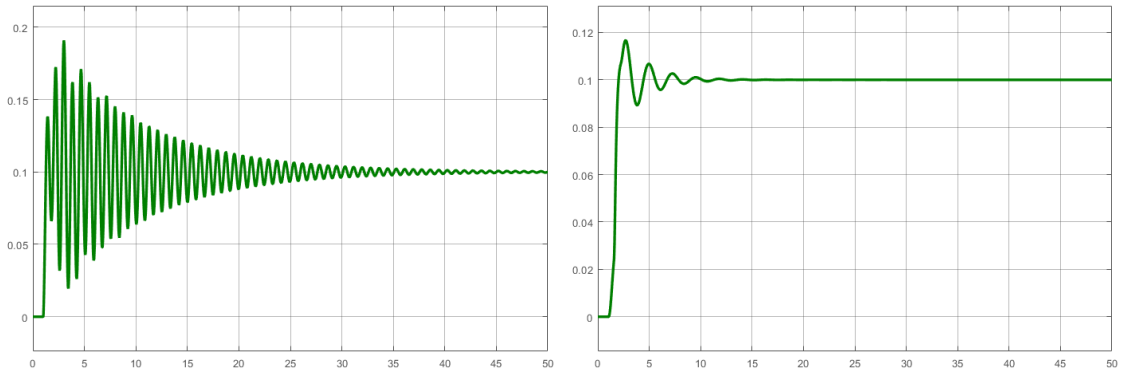

(a) x_1 (b) x_2

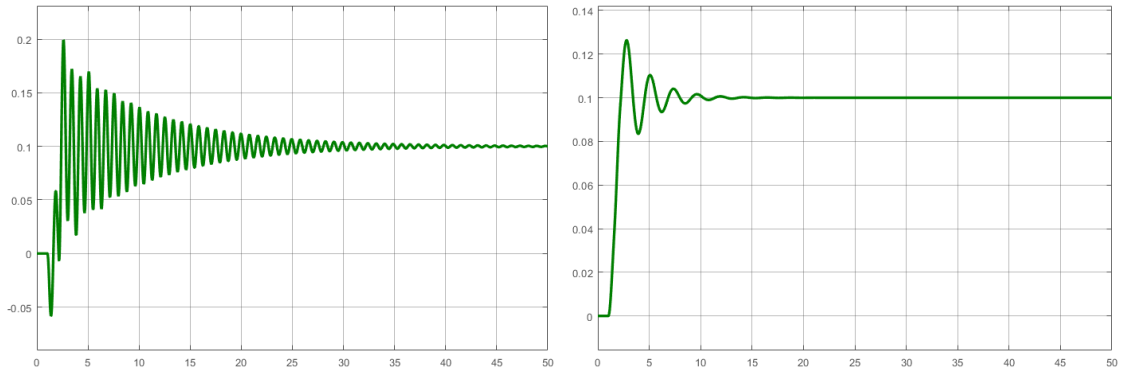

(c) x_3 (d) x_t

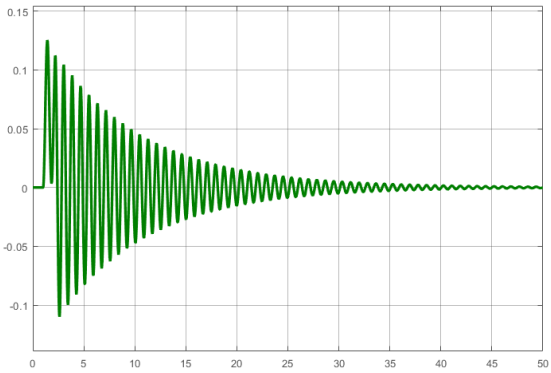

(e) θ_t

Source: Author.

Table 10 – Six-wheels AGV outputs parameters for the step input.

	x_t	θ_t
Delay time (t_d) [s]	1.71	1.277
Rise time (t_r) [s]	0.836	-
Peak time (t_p) [s]	2.794	1.408
Settling time (t_s) [s]	8.764	32.06
Overshoot (M_p)	0.0264	-

Source: Author.

4.1.3 Ramp

The last input on the time analysis is the ramp function. The slope of the ramp was defined with A_r = 0.002 m. For this type of input, the outputs are expected to follow the slope of the ramp, without oscillating over it. As for the angle θ_t, a response such as that of the step for linear displacements is desired, that is, from a time on the ramp, the angle will stabilize with the value of the angle of inclination of the ramp (in this case, approximately 0.00145 radians). In Figure 38 all forms of the ramp inputs for the three models can be observed.

Figure 38 – Ramp input forms for all the AGVs

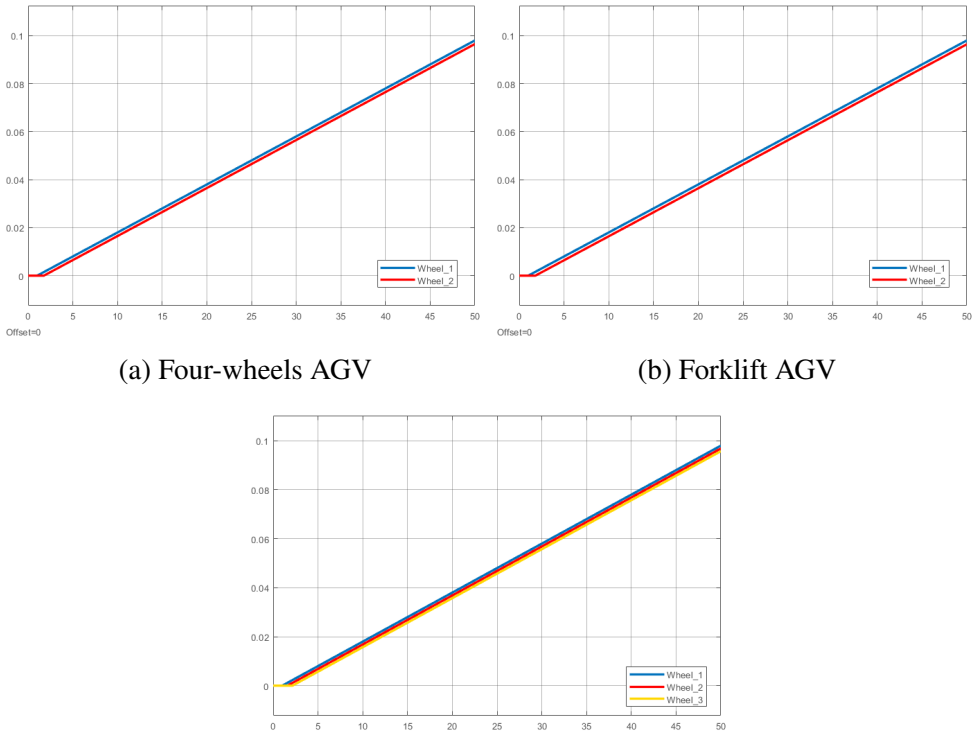

(a) Four-wheels AGV

(b) Forklift AGV

(c) Six-wheels AGV

Source: Author.

Figure 38a shows the ramp input in function of time for the four-wheels AGV, Figure 38b shows the ramp input in function of time for the forklift AGV and Figure 38c shows the ramp input in function of time for the six-wheels AGV.

In general, as can be seen in Figures 39, 40 and 41, for all models the response of the linear displacements of the mass M_t presented an almost perfect shape, with small oscillations at the beginning of the rising, stabilizing before the 10, 25 and 5 seconds for the four-wheel, forklift and six-wheel models, respectively. However, the settling time of the forklift AGV was the biggest again what proved to be marginally less stable for the load, also presenting the greatest oscillations amplitude among all at the beginning of the ramp.

In Figure 39a, x_1 represents the linear displacement of the front wheel suspension in function of time. In Figure 39b, x_2 is the linear displacement of the rear wheel suspension in function of time. In Figure 39c, x_t is the linear displacement in function of time of the total mass

Figure 39 – Outputs of the four-wheels AGV for the ramp input.

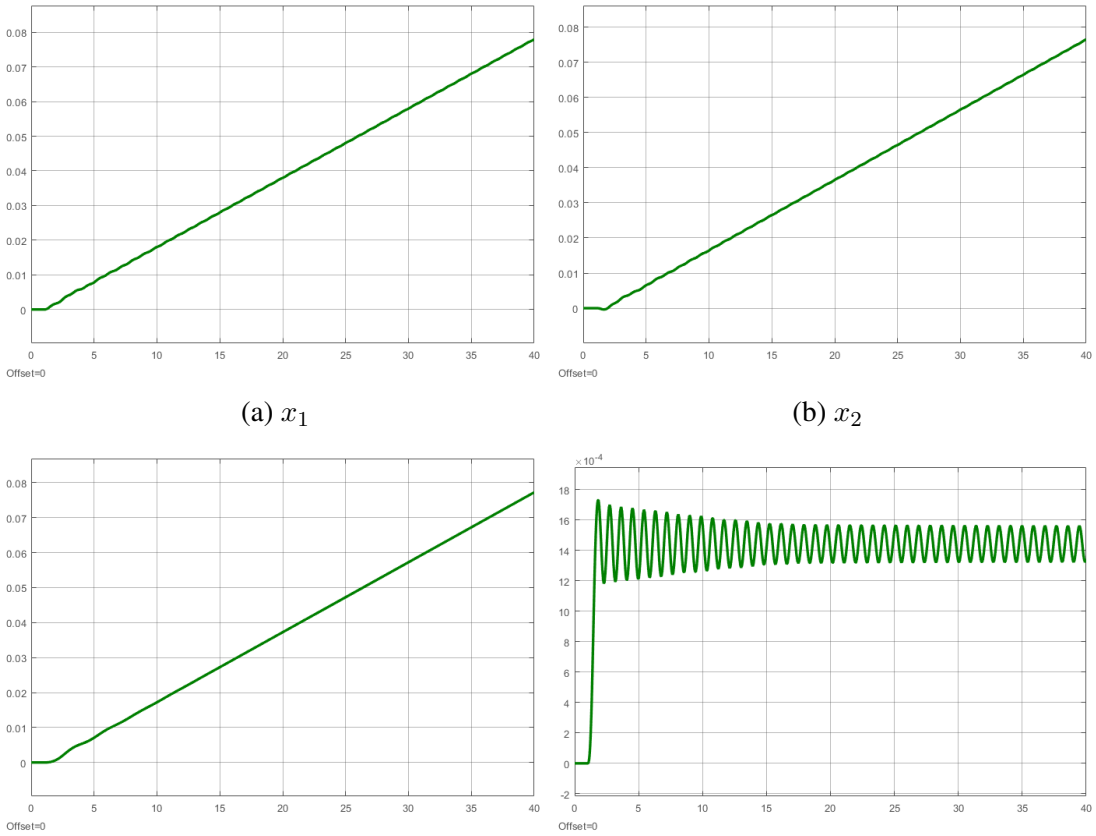

(a) x_1 (b) x_2

(c) x_t (d) θ_t

Source: Author.

of the loaded AGV and in Figure 39d, θ_t is the angular displacement in function of time of the total mass of the loaded AGV.

Therefore, in Tables 11, 12 and 13 the parameters were analyzed only for θ_t, since their answers have greater complexity, even if with similar forms. For the four-wheel AGV, θ_t was oscillating with an amplitude that does not exceed 0.0006 radians and with an overshoot of 0.00029, but it decreased very slowly, making the settling beyond the simulation period.

Table 11 – Four-wheels AGV output parameters for the ramp input.

	θ_t
Delay time (t_d) [s]	1.487
Rise time (t_r) [s]	0.359
Peak time (t_p) [s]	1.852
Setting time (t_s) [s]	>50
Overshoot (M_p) [m]	0.00029

Source: Author.

In Figure 40a, x_1 represents the linear displacement of the front wheel suspension in function of time. In Figure 40b, x_2 is the linear displacement of the rear wheel suspension in function of time. In Figure 40c, x_t is the linear displacement in function of time of the total mass

Figure 40 – Outputs of the forklift AGV for the ramp input.

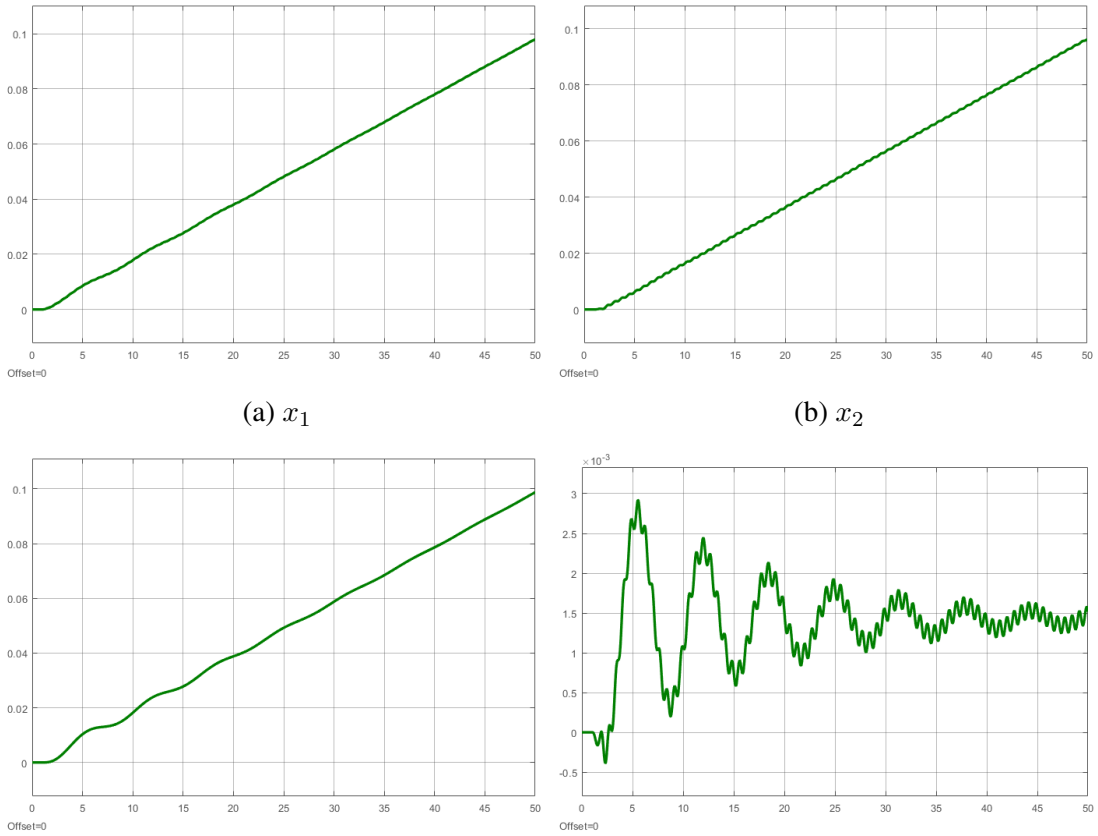

(a) x_1 (b) x_2

(c) x_t (d) θ_t

Source: Author.

of the loaded AGV and in Figure 40d, θ_t is the angular displacement in function of time of the total mass of the loaded AGV.

Table 12 – Forklift AGV output parameters for the ramp input.

	θ_t
Delay time (t_d) [s]	3.893
Rise time (t_r) [s]	0.917
Peak time (t_p) [s]	5.531
Setting time (t_s) [s]	>50
Overshoot (M_p) [m]	0.0014

Source: Author.

For the AGV forklift, θ_t presented more significant oscillations, extrapolating 0.003 radians. In addition, again the answer has oscillations within the oscillations, which causes an almost vibratory movement on the load, which is not desired at all.

In Figure 41a, x_1 represents the linear displacement of the front wheel suspension in function of time. In Figure 41b, x_2 is the linear displacement of the center wheel suspension in function of time. In Figure 41c, x_3 is the linear displacement of the rear wheel suspension in function of time. In Figure 41d, x_t is the linear displacement in function of time of the total mass

Figure 41 – Outputs of the six-wheels AGV for the ramp input.

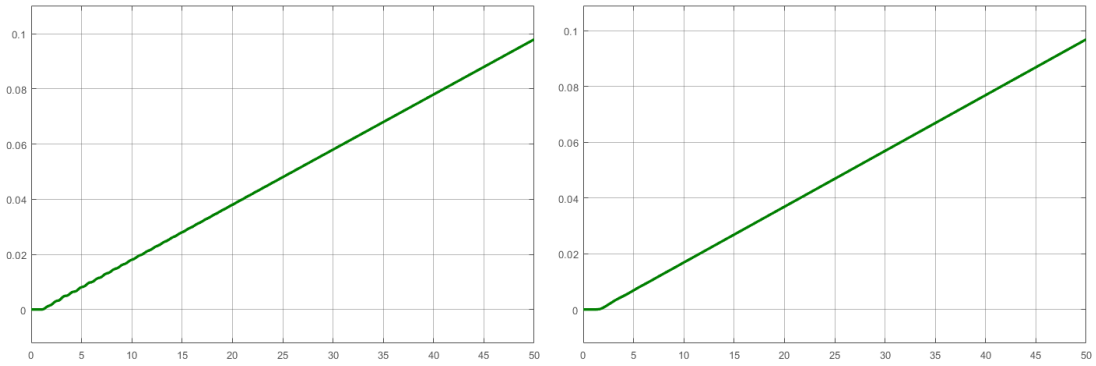

(a) x_1 (b) x_2

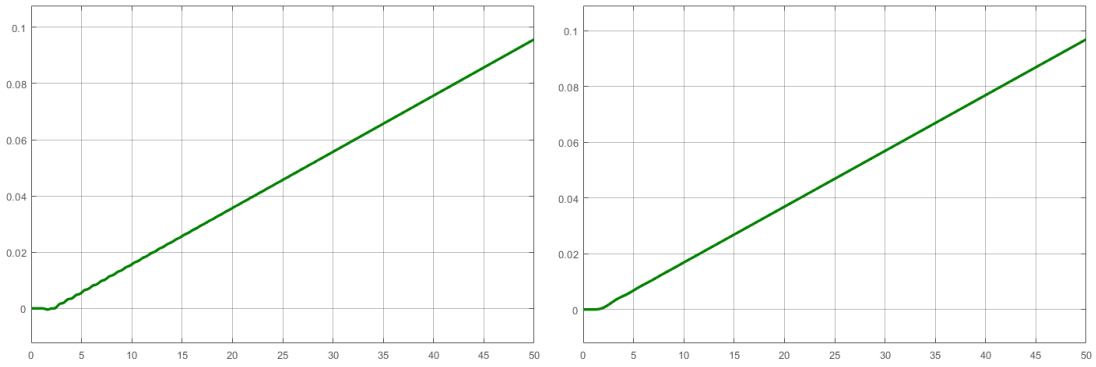

(c) x_3 (d) x_t

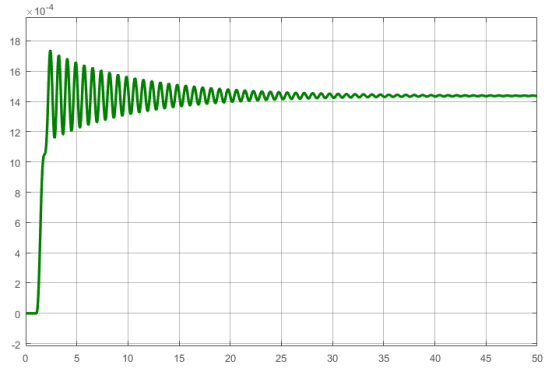

(e) θ_t

Source: Author.

of the loaded AGV and in Figure 41e, θ_t is the angular displacement in function of time of the total mass of the loaded AGV.

For the six-wheels AGV, again the settling time for θ_t is considerably lower, even if it is still slightly elevated, longer than 30 seconds. It presents overshoot values similar to the four-wheels AGV. After analyzing all the answers, the input function that caused more impact on the load, as expected, was the pulse, followed by the step and ramp functions. For the models that appeared to be more stable, the descending order was six-wheels unit load, four-wheels unit load and the forklift. In respect to AGV models, this order can be easily changed with modifications

Table 13 – Six-wheels AGV output parameters for the ramp input.

	θ_t
Delay time (t_d) [s]	1.502
Rise time (t_r) [s]	0.0899
Peak time (t_p) [s]	2.409
Setting time (t_s) [s]	30.64
Overshoot (M_p) [m]	0.00029

Source: Author.

in the parameters defined at the beginning of this chapter, but this is not the focus of this study.

4.2 Frequency response

For the response analysis in the frequency domain, the Bode diagrams were plotted. As previously defined, a transfer function will always be the ratio between an output and an input, and in case the output is affected by two or more inputs, the effects must be then superimposed for a response in time. Such overlap was made in Simulink. In the frequency analysis, Bode diagrams are made for each transfer function, that is, the total diagrams of the model will be the product of the number of inputs by the number of outputs.

Figure 42 – Bode diagrams - Four-wheels AGV

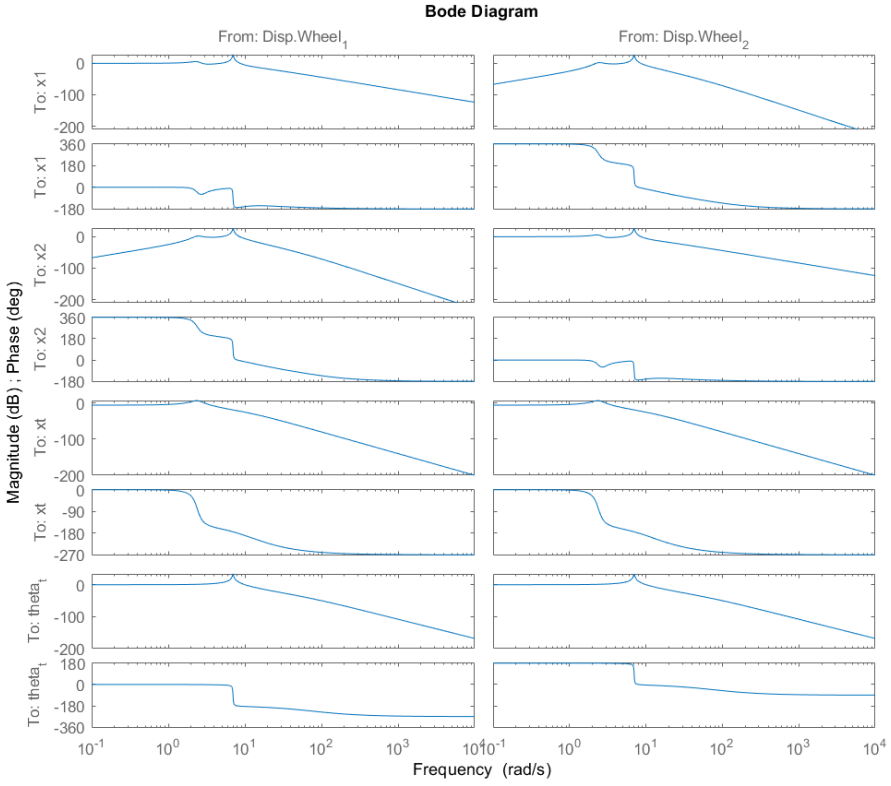

Source: Author.

The sets of Bode diagrams are shown in Figures 42, 43 and 44 are shown, with the magnitude and phase diagrams for all TFs of the four-wheel, forklift and six-wheel AGVs, respectively. In Appendix B, the same diagrams are plotted separately, allowing better visibility.

The main information to be obtained from the Bode diagrams will be the damped natural frequencies of the system, frequencies which if excited can cause resonance in the vehicle. As explained in Chapter 3, for under-damped systems - as is the case - the resonances are manifested as peaks in the magnitude diagrams.

Observing the Bode diagrams of the four-wheel AGV, it is possible to notice two peaks, one around 2.3 rad/s and the other around 7 rad/s. Although both peaks are present in the TFs of the suspension, only the first peak shows for x_t and the second for θ_t. This means each of these frequencies will cause a displacement of the load, whether linear or angular, to resonate, so it should be avoided. It is also noticeable that the first peak is more attenuated in the diagrams of x_1 and x_2, showing that the second dumped natural frequency will have more impact on them.

Figure 43 – Bode diagrams - Forklift AGV

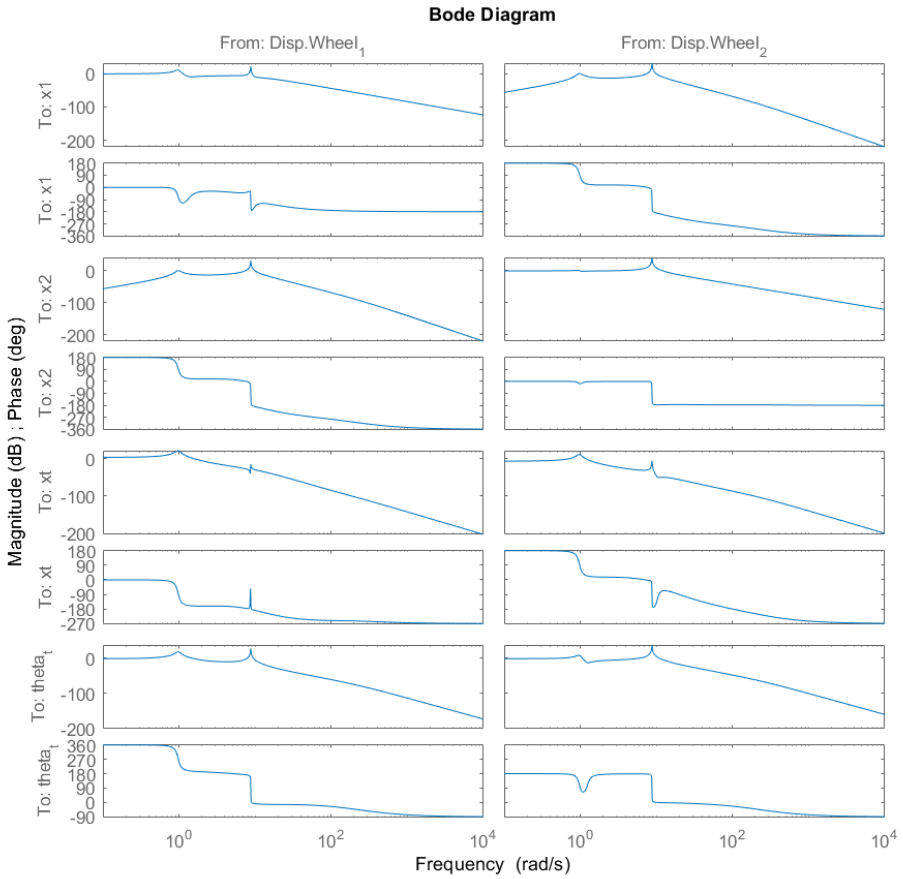

Source: Author.

As with the four-wheel AGV, the forklift model also has two peaks in its Bode diagrams, the first around 1 rad/s and the second around 8.7 rad/s. But this time, both are present for all

outputs, showing that this AGV model has a greater interaction between the angular and linear displacement of the load in the frequency domain.

Figure 44 – Bode diagrams - Six-wheels AGV

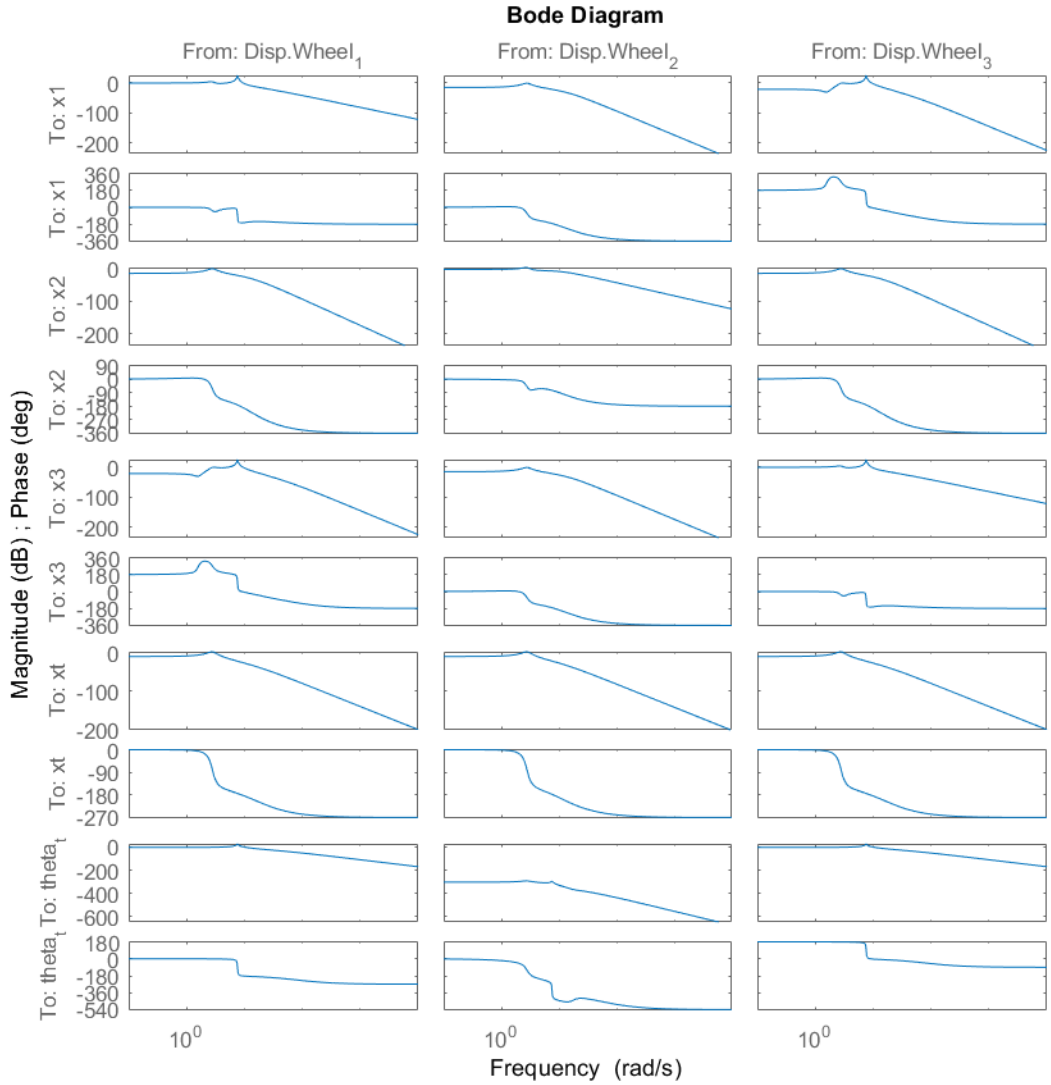

Source: Author.

Finally, for the six-wheels AGV, more diagrams are plotted given the increased number of inputs and outputs. Despite having a greater damping, the peaks are still visible, and again, due to the symmetry caused by the position of the gravitational center, the first peak, around X, appears in the vertical displacement diagrams x_1, x_2, x_3 and x_t. The second peak, however, appears only at x_1, x_3 and θ_t, since x_2 is aligned with x_t. All damped natural frequencies obtained from the Bode diagrams are specified in Table 14. In conclusion, the influence of the damped natural frequencies is related to the outputs of the mass M_t and to the positioning of the gravitational center in relation to the suspensions.

Table 14 – AGV's damped natural frequency

AGV	ω_{n1}		ω_{n2}	
	[rad/s]	**[Hz]**	**[rad/s]**	**[Hz]**
4 wheels	2.350	0.374	7.010	1.116
Forklift	0.968	0.154	8.750	1.393
6 wheels	2.730	0.434	7.600	1.209

Source: Author.

4.3 Poles and zeros analysis

Finally, in order to study the stability of the systems, state space formulation was used to stratify the eigenvalues of the state matrix to obtain all poles of AGVs, which are specified in Tables 15, 16 and 17. In addition, the poles and zeros maps were also plotted from the obtained MIMO system, which are presented in Figures 45, 46 and 47, for the four-wheel, forklift and six-wheel AGVs respectively.

Figure 45 – Poles and zeros map - Four-wheels AGV

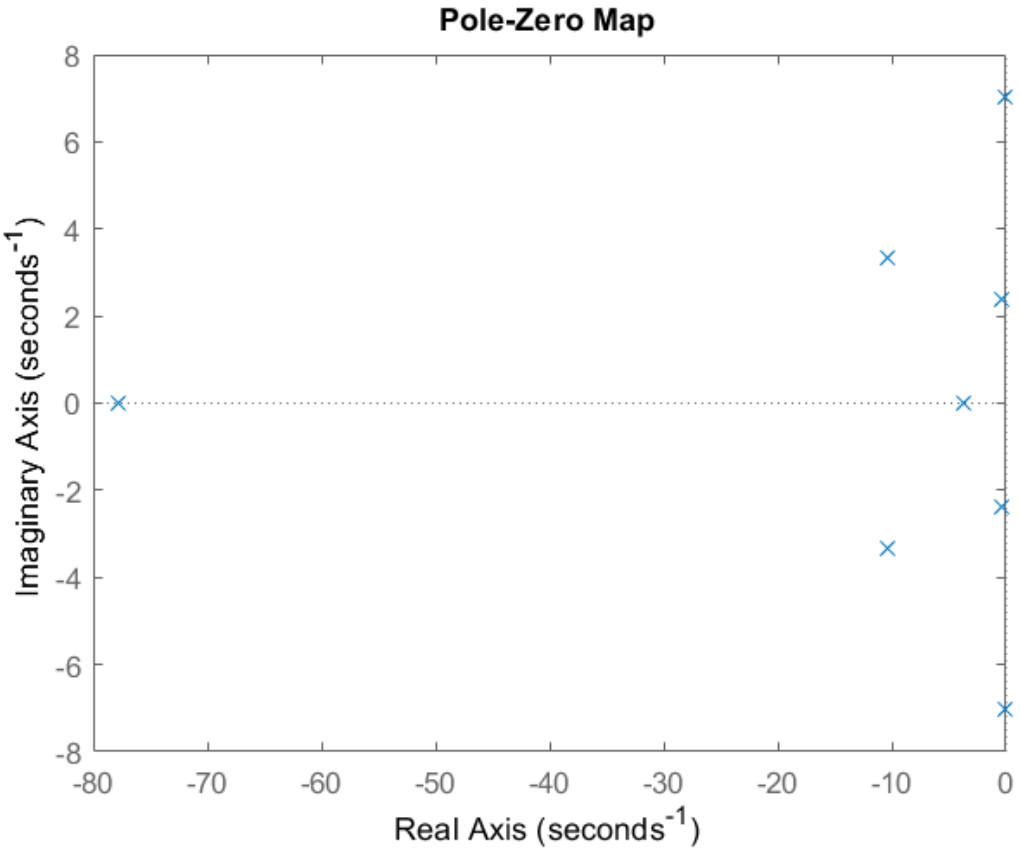

Source: Author.

According to Tables 15, 16 and 17, all systems are stable, since all poles are on the left side of the plane s, that is, they are all negative. This stability is confirmed by the tendency of

Table 15 – Poles - 4 Wheels AGV

Pole 1	-77.8667+0.0000i
Pole 2	-3.6821+0.0000i
Pole 3	-10.4098+3.3343i
Pole 4	-10.4098-3.3343i
Pole 5	-0.3235+2.3683i
Pole 6	-0.3235-2.3683i
Pole 7	-0.0755+7.0101i
Pole 8	-0.0755-7.0101i

Source: Author.

Figure 46 – Poles and zeros map - Forklift AGV

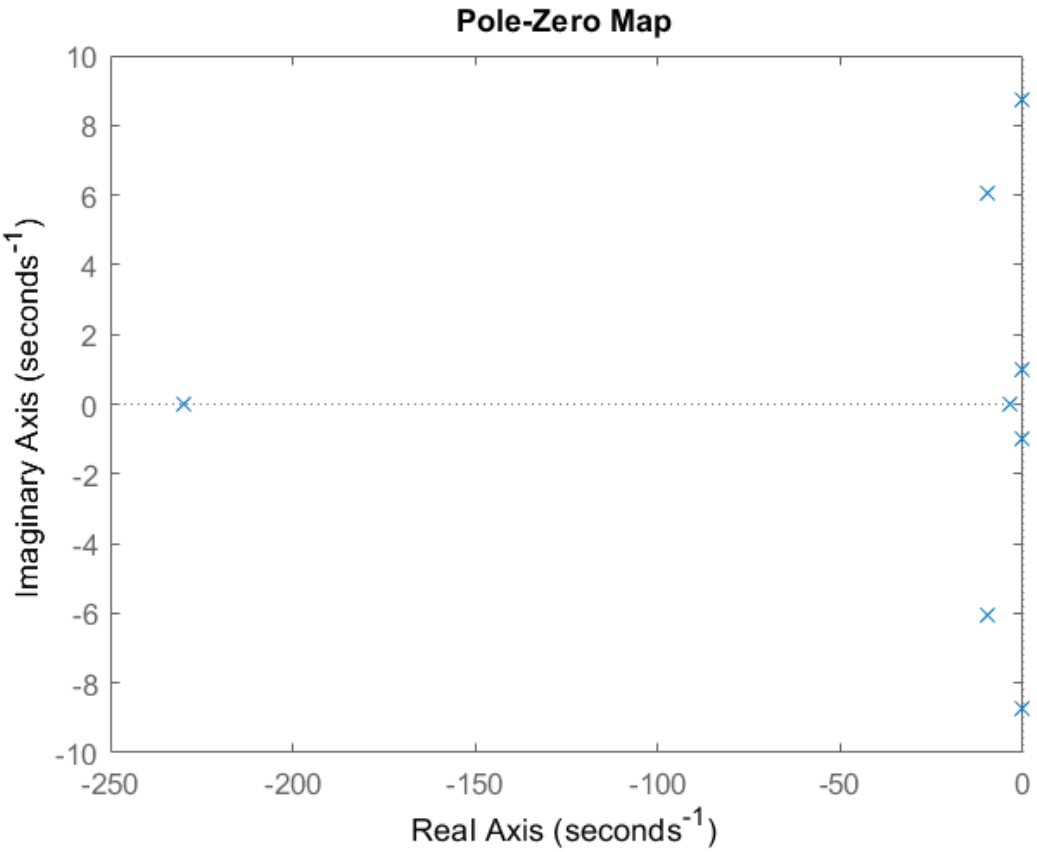

Source: Author.

responses in the time domain to reduce the amplitude of its oscillations until it stops completely. Although in the time simulation some outputs have not settled totally, with the study of the poles it is possible to confirm that eventually this balance point will occur. The analysis of the poles will also be important for future next steps, as for example on the implementation of a controller. Once the model is functional and the parameters are adjusted in order to improve the responses keeping the system stable, the possibility of closing the mesh and eventually controlling it is easier to be studied.

In order to provide more information on the stability of the system, changes on the gain

Table 16 – Poles - Forklift AGV

Pole 1	-1.8068E+02+0.0000i
Pole 2	-9.7015+6.0596i
Pole 3	-9.7015-6.0596i
Pole 4	-0.0411-8.6083i
Pole 5	-0.0411+8.6083i
Pole 6	-0.0655+0.9692i
Pole 7	-0.065-0.9692i
Pole 8	-3.5561+0.0000i

Source: Author.

Figure 47 – Poles and zeros map - Six-wheels AGV

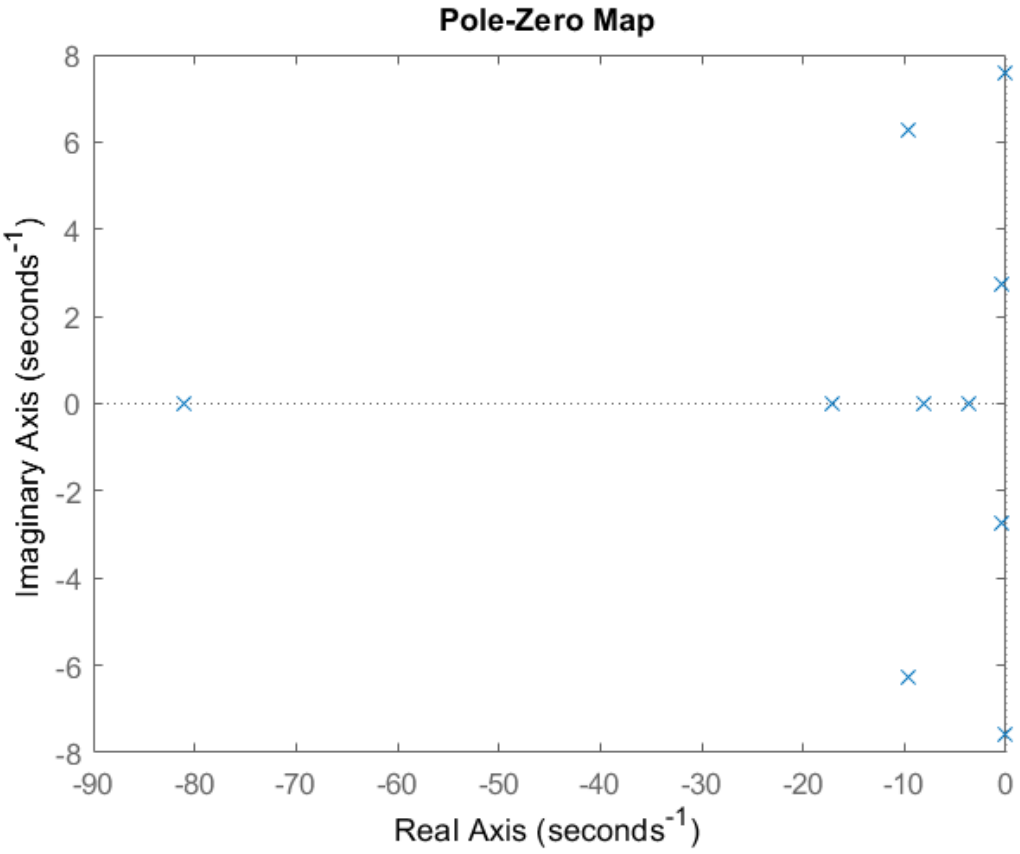

Source: Author.

of the TFs were put in place. The root locus method, a graphic technique to determine the path taken by the closed-loop poles with the variation of system parameters, was applied. It is a widely used tool for both stability analysis and design of control systems. The charts produced are included in Appendix C.

Table 17 – Poles - 6 Wheels AGV

Pole 1	-81,0682+0,0000i
Pole 2	-17,1497+0,0000i
Pole 3	-9,6584+6,2684i
Pole 4	-9,6584-6,2684i
Pole 5	-0,1122+7,5959i
Pole 6	-0,1122-7,5959i
Pole 7	-8,1766+0,0000i
Pole 8	-0,4080-2,7586i
Pole 9	-0,4080+2,7586i
Pole 10	-3,6863+0,0000i

Source: Author.

5 Conclusions

In this work, three AGVs were dynamically modeled in order to enable the study of their responses in time and frequency domains, in addition to the analysis of the models stability. The modeling, focused on the actions of the suspensions, was developed with half of the vehicles, and the results were obtained through the method of space-state with the aid of the MATLAB - Simulink software.

As expected by the literature review, the responses in time and in the frequency of the models presented a conventional form, validating the models (even if not fully, since there were no practical tests). For the ramp input, time results were less oscillatory in general, being the safest obstacle for the loads of these AGVs. As for the step function, the models with four wheels showed great oscillations for the angular displacements, which for the six-wheel vehicle was largely attenuated due to the extra damping. The same was detected for the pulse function.

Among the four-wheel vehicles, the forklift proved to be relatively less stable than the unit load, since under the same conditions, the oscillations were considerably higher. This phenomenon is a consequence of the outdated gravitational center due to the fact that the load is supported on the forks at the front of the vehicle.

From the frequency response, two dampened natural frequencies were observed in each model, the first being in greater relations with linear displacement and the second with angular displacements. The response in the frequency domain was very similar between all three vehicles, as two resonance frequencies arose at each simulation.

The parameters chosen for the vehicles showed that, in general, the three have stability in terms of their poles study, but that the damping coefficient of the dampers would not be suitable for the proposed obstacles. In addition, in the case of the AGV forklift, it is necessary that the rear wheels have different suspensions to ensure less oscillation of the load.

As the goal of this work was to model three different AGVs and to compare the responses between them, the values of the properties of the machine elements and their dimensions were estimated from literature. That said, the results with high oscillations show the importance of a dynamic model, even if simplified, especially for the four-wheel AGV, which had all of its data extracted entirely from the prototype project developed by HOOGEWIJS (2020). The model and procedures proposed were proved capable of contesting the values found and evaluating (and eventually modifying, in a design context) them, either to obtain a more stable response, or to adjust the parameters to the ones of commercial elements to make it possible to manufacture the AGV.

In addition, the parameters were calculated by HOOGEWIJS (2020) only to the unit load type AGV with four wheels, and the absence of other references implied on the estimation for the two other concepts, which may also justify responses with high settling times as the ones obtained.

In general, the models are ready to be used in whatever way necessary to support a project or as a basis for more complex simulations and investigations or even for closing the control loop of the vehicles and implementing passive suspension modules on them.

5.1 Next steps

Regarding the information found in literature, even a simple model can highlight potential failures in the choice of dampers, springs and tires in a prototype project. However, for a more reliable study it would be necessary to complex the model by adding variables such as acceleration of the vehicle, friction of the ground with the tire, forces from a curvilinear movement, weariness of the angles of row and yaw in the modeling, among others.

In addition, the use of the state space form opens the door for the implementation of controllers that are not only in PID format, but eventually even a LQR or observer-controller type, closing the loop with the ability to adjust finer and more subtle responses than PID controllers with configurations suitable for a variety of scenarios. This could, perhaps, lead to feasible AGV applications on non-conventional terrains such as sandy and snow-covered.

Bibliography

AGUIRRE, L. *Introdução à Identificação de Sistemas – Técnicas Lineares e Não-Lineares Aplicadas a Sistemas Reais*. 2. ed. Belo Horizonte, Brazil: UFMG, 2004.

BA-SYSTèMES. *Horizontal Reel AGV*. 2020. Last access: 11/22/2020. Disponível em: <https://www.basystemes.com/en/agvs/range/gbh/>.

BOTTURA, C. *Análise Linear de Sistemas*. 1. ed. Rio de Janeiro, Brazil: Guanabara Dois, 1982.

CANO, C. E. V. *Técnica de navegação de um robô móvel baseado em um sistema de visão para entregá-lo a uma célula flexível de manufatura.* Tese (Doutorado) — Universidade de Brasília, Programa de Mestrado em Sistemas Mecatrônicos, 2006.

CASTRUCCI, P.; BRITTAR, A.; SALES, R. *Controle Automático*. 1. ed. Rio de Janeiro, Brazil: LTC, 2011.

CATARRINHO, R. F. S. d. M. *Contribuição para o fabrico de um Veículo Guiado Automaticamente.* Tese (Doutorado) — Instituto Superior de Engenharia de Coimbra, 2018.

DARUS, R.; ENZAI, N. Modeling and control active suspension system for a quarter car model. *International Conference on Science and Social Research (CSSR 2010)*, 2010.

DARUS, R.; SAM, Y. Modeling and control active suspension system for a full car model. *5th International Colloquium on Signal Processing Its Applications (CSPA)*, 2009.

D'AZZO, J.; HOUPIS, C. *Linear Control Systems Analysis and Design: Conventional and Modern*. 4. ed. New York, USA: McGraw-Hill, 1995.

DORF, C.; MBIHOP, H. *Sistema de Controle Modernos*. 12. ed. Rio de Janeiro, Brazil: LTC, 2013.

DUKKIPATI, R. *Solving Engineering System Dynamic Problems with MATLAB*. 1. ed. New Delhi, India: New Age International, 2007.

FAZLOLLAHTABAR, H.; NIAKI, S. Fault tree analysis for reliability evaluation of an advanced complex manufacturing system. *Advaced Manufacturing System*, v. 17, n. 01, 2018. ISSN 107-18.

FELICIO, L. C. *Modelagem da Dinâmica de Sistemas e Estudo da Resposta*. São Carlos, Brazil: RiMa Editora, 2010.

FERRELLI, P. et al. Redução de custos operacionais e condições inseguras em um almoxarifado após automatização de rotas internas. *CONBREPRO*, Ponta Grossa, PR, 2015.

FRANKLIN, G.; POWELL, J.; EMANI-NAEINI, A. *Feedback Control of Dynamic Systems*. 4. ed. New Jersey, USA: Prentice Hall, 2002.

GEROMEL, J.; PALHARES, A. *Análise Linear de Sistemas Dinâmicos: Teoria, Ensaios Práticos e Exercícios*. 1. ed. São Paulo, Brazil: Edgard Blücher Ltda., 2004.

HADERSPECK, J. Carregado e pronto para trabalhar: plataformas agv inteligentes aumentam a eficiência. *Indústria de Bebidas*, p. 60+, 2019.

HAMMOND, L. Agvs at work. *IFS Publications Ltd*, United Kingdon, 1986.

HOOGEWIJS, D. *Research and design of an autonomous and collaborative guided vehicle prototype, to be applied in indoor and outdoor environments and different types of floor.* Tese (Doutorado) — Programa de Pós-gradação em Engenharia Mecânica da Universidade Federal de São Carlos, 2020.

KARNOPP, D.; MARGOLIS, D.; ROSENBERG, R. *System Dynamics: Modeling and Simulation of Mechatronic Systems*. 4. ed. Hoboken, USA: John Wiley and Sons, 2006.

KIM, C. W.; TANCHOCO, J. M. A. Agv dispatching based on workload balancing. 1999.

KLUEVER, C. *Dynamic Systems: Modeling, Simulation and Control*. 1. ed. Hoboken, USA: John Wiley and Sons, 2015.

LARSSON T.J. AND, L. J. et al. Industrial forklift trucks - dynamic stability and the design of safe logistics. *Safety Science Monitos*, v. 7, 2003.

NISE, N. *Engenharia de Sistemas de Controle*. 6. ed. Rio de Janeiro, Brazil: LTC, 2009.

NKC-KOLEC. *Products/Forklif AGV*. 2020. Last access: 11/22/2020. Disponível em: <https://www.kolec.co.jp/user_data/en/product/robo_fork>.

OGATA, K. *Engenharia de Controle Moderno*. 5. ed. São Paulo, Brazil: Pearson - Prentice Hall, 2010.

PéREZ, O. L. *Uma arquitetura mecatrônica de navegação para veículos com reboques guiados automaticamente em ambientes de sistemas flexíveis de manufatura.* Tese (Doutorado) — Universidade Federal do Rio de Janeiro, Programa de Pós-Graduação em Engenharia Mecânica, 2010.

RAO, S. *Vibrações Mecânica*. São Paulo, Brazil: Pearson Education do Brasil, 2009.

SANTOS, L. et al. A viabilidade da implementação de agvs em regiões portuárias. *CONBREPRO*, Ponta Grossa, PR, 2018.

SCOTT-AUTOMATION. *Conveyor/Unit Load AGV*. 2020. Last access: 11/22/2020. Disponível em: <https://www.scottautomation.com/products/conveyor-liftdeck-agv-automatic-guided-vehicle/#>.

SPERANZA, M. *Modelagem de Dinâmica de Sistemas - Notas de Aula*. Rio de Janeiro, Brazil: DEM/PUC-Rio, 2016. Last access: 12/15/2020.

WITCZAK, M. et al. Fault diagnosis of an automated guided vehicle with torque and motion forces estimation: A case study. *ISA Transactions*, v. 104, 2020.

YAN, R.; JACKSON, L. M.; DUNNETT, S. J. Automated guided vehicle mission reliability modelling using a combined fault tree and petri net approach. *Advaced Manufacturing Technology*, v. 92, n. 5, 2017. ISSN 1825–37.

Appendix

APPENDIX A – MATLAB routines

A.1 Four-wheels AGV

```
close all
clear all
clc

%% Initial Data %%

% Masses
M1 = 25; % Supension 1 mass[kg]
M2 = 25; % Supension 2 mass[kg]
Mc = 100; % Chassis mass[kg]
Ml = 500; % Load mass[kg]
Mt = Ml/2+Mc/2; % Chassis + load mass[kg]
It = 3.93; % Mass inertia moment [kg.m ]

% Springs
K12 = 1600; %Spring stiffness (Suspension 1) [N/m]
K22 = 1600; %Spring stiffness (Suspension 2) [N/m]

% Tires
K11 = 1600; %Tire stiffness (Suspension 1) [N/m]
K21 = 1600; %Tire stiffness (Suspension 2) [N/m]

% Dumpers
B11 = 460; %Damping coefficient (Suspension 1) [Ns/m]
B21 = 460; %Damping coefficient (Suspension 2) [Ns/m]

% Dimensions - check schematic
l1 = 0.52; %[m]
l2 = 0.52; %[m]

%% State Space %%

% System matrix
```

```
34 A = [0 0 0 0 1 0 0 0;
35       0 0 0 0 0 1 0 0;
36       0 0 0 0 0 0 1 0;
37       0 0 0 0 0 0 0 1;
38       (-K11-K12)/M1 0 K12/M1 (K12*l1)/M1 -B11/M1 0 B11/M1 (B11*
             l2)/M1;
39       0 (-K21-K22)/M2 K22/M2 (-K22*l2)/M2 0 -B21/M2 B21/M2 (-B21
             *l1)/M2;
40       K12/Mt K22/Mt (-K22-K12)/Mt ((K22*l2)-(K12*l1))/Mt B11/Mt
             B21/Mt (-B11-B21)/Mt (-(B11*l2)+(B21*l1))/Mt;
41       (K12*l1)/It (-K22*l2)/It ((K22*l2)-(K12*l1))/It (-(K22*l2
             ^2)-(K12*l1^2))/It (B11*l2)/It (-B21*l1)/It (-(B11*l2)
             +(B21*l1))/It (-(B11*l2^2)-(B21*l1^2))/It];
42
43 % Input matrix
44 B = [0 0;
45       0 0;
46       0 0;
47       0 0;
48       K11/M1 0;
49       0 K21/M2;
50       0 0;
51       0 0];
52
53 % Output matrix
54 C = [1 0 0 0 0 0 0 0;
55       0 1 0 0 0 0 0 0;
56       0 0 1 0 0 0 0 0;
57       0 0 0 1 0 0 0 0];
58
59 % Feedforward matrix
60 D = [0 0;
61       0 0;
62       0 0;
63       0 0];
64
65
66 states = {'x1' 'x2' 'xt' 'theta_t' 'x1*' 'x2*' 'xt*' 'theta_t*'
       };
```

```
67 inputs = {'Disp.Wheel_1' 'Disp.Wheel_2'};
68 outputs = {'x1' 'x2' 'xt' 'theta_t'};
69
70 sys_mimo = ss(A,B,C,D,'statename',states,...
71 'inputname',inputs,...
72 'outputname',outputs);
73
74 % State space to Transfert Function
75 TF = tf(sys_mimo);
76
77 %% Stability - Pole&Zero Map
78 stability = eig(A);
79 figure
80 pzmap(sys_mimo);
81
82
83 %% Frequency response - BODE
84 bode(sys_mimo);
85 for i=1:4
86     for j=1:2
87     figure
88     bode(sys_mimo(i,j))
89     end
90 end
91
92 %% Root Locus %%
93 for i=1:4
94     for j=1:2
95     figure
96     rlocus(sys_mimo(i,j))
97     end
98 end
```

A.2 Forklift AGV

```
close all
clear all
clc

%% Initial Data %%

% Masses
M1 = 18; % Supension 1 mass[kg]
M2 = 25; % Supension 2 mass[kg]
Mc = 240; % Chassis mass[kg]
Ml = 500; % Load mass[kg]
Mt = Ml/2+Mc/2; % Chassis + load mass[kg]
It = 8.4; % Mass inertia moment [kg.m ]

% Springs
K12 = 1600; %Spring stiffness (Suspension 1) [N/m]
K22 = 1600; %Spring stiffness (Suspension 2) [N/m]

% Tires
K11 = 1600; %Tire stiffness (Suspension 1) [N/m]
K21 = 1600; %Tire stiffness (Suspension 2) [N/m]

% Dumpers
B11 = 460; %Damping coefficient (Suspension 1) [Ns/m]
B21 = 460; %Damping coefficient (Suspension 2) [Ns/m]

% Dimensions - check schematic
l1 = 0.5; %[m]
l2 = 0.5; %[m]
l3 = 1.62; %[m]
l4 = 1.62; %[m]


%% State Space %%

% System matrix
A = [0 0 0 0 1 0 0 0;
```

```
38        0 0 0 0 0 1 0 0;
39        0 0 0 0 0 0 1 0;
40        0 0 0 0 0 0 0 1;
41        (-K11-K12)/M1 0 K12/M1 (-K12*l2)/M1 -B11/M1 0 B11/M1 (-B11
              *l1)/M1;
42        0 (-K21-K22)/M2 K22/M2 (-K22*l4)/M2 0 -B21/M2 B21/M2 (-B21
              *l3)/M2;
43        K12/Mt K22/Mt (-K22-K12)/Mt ((K22*l4)+(K12*l2))/Mt B11/Mt
              B21/Mt (-B11-B21)/Mt ((B11*l1)+(B21*l3))/Mt;
44        (-K12*l2)/It (-K22*l4)/It ((K22*l4)+(K12*l2))/It (-(K22*l4
              ^2)-(K12*l2^2))/It (-B11*l1)/It (-B21*l3)/It ((B11*l1)
              +(B21*l3))/It (-(B11*l1^2)-(B21*l3^2))/It];
45
46 % Input matrix
47 B = [0 0;
48        0 0;
49        0 0;
50        0 0;
51        K11/M1 0;
52        0 K21/M2;
53        0 0;
54        0 0];
55
56 % Output matrix
57 C = [1 0 0 0 0 0 0 0;
58        0 1 0 0 0 0 0 0;
59        0 0 1 0 0 0 0 0;
60        0 0 0 1 0 0 0 0];
61
62 % Feedforward matrix
63 D = [0 0;
64        0 0;
65        0 0;
66        0 0];
67
68
69 states = {'x1' 'x2' 'xt' 'theta_t' 'x1*' 'x2*' 'xt*' 'theta_t*'
       };
70 inputs = {'Disp.Wheel_1' 'Disp.Wheel_2'};
```

```
71 outputs = {'x1' 'x2' 'xt' 'theta_t'};
72
73 sys_mimo = ss(A,B,C,D,'statename',states ,...
74 'inputname',inputs ,...
75 'outputname',outputs);
76
77 % State space to Transfert Function
78 TF = tf(sys_mimo);
79
80 %% Stability - Pole&Zero Map
81 stability = eig(A);
82 figure
83 pzmap(sys_mimo);
84
85
86 %% Frequency response - BODE
87 bode(sys_mimo);
88 for i=1:4
89     for j=1:2
90     figure
91     bode(sys_mimo(i,j))
92     end
93 end
94
95 %% Root Locus %%
96 for i=1:4
97     for j=1:2
98     figure
99     rlocus(sys_mimo(i,j))
100    end
101 end
```

A.3 Six-wheels AGV

```
close all
clear all
clc

%% Initial Data %%

% Masses
M1 = 20; % Supension 1 mass[kg]
M2 = 25; % Supension 2 mass[kg]
M3 = 20; % Supension 3 mass[kg]
Mc = 180; % Chassis mass[kg]
Ml = 500; % Load mass[kg]
Mt = Ml/2+Mc/2; % Chassis + load mass[kg]
It = 9.5; % Mass inertia moment [kg.m ]

% Springs
K12 = 1600; %Spring stiffness (Suspension 1) [N/m]
K22 = 1600; %Spring stiffness (Suspension 2) [N/m]
K32 = 1600; %Spring stiffness (Suspension 3) [N/m]

% Tires
K11 = 1600; %Tire stiffness (Suspension 1) [N/m]
K21 = 1600; %Tire stiffness (Suspension 2) [N/m]
K31 = 1600; %Tire stiffness (Suspension 3) [N/m]

% Dumpers
B11 = 460; %Damping coefficient (Suspension 1) [Ns/m]
B21 = 460; %Damping coefficient (Suspension 2) [Ns/m]
B31 = 460; %Damping coefficient (Suspension 3) [Ns/m]

% Dimensions - check schematic
l1 = 0; %[m]
l2 = 0.8; %[m]
l3 = 0.8; %[m]

%% State Space %%

```

```
38 % System matrix
39 A = [0 0 0 0 0 1 0 0 0 0;
40       0 0 0 0 0 0 1 0 0 0;
41       0 0 0 0 0 0 0 1 0 0;
42       0 0 0 0 0 0 0 0 1 0;
43       0 0 0 0 0 0 0 0 0 1;
44       (-K11-K12)/M1 0 0 K12/M1 (K12*12)/M1 -B11/M1 0 0 B11/M1 (
             B11*13)/M1;
45       0 (-K21-K22)/M2 0 K22/M2 (-K22*11)/M2 0 -B21/M2 0 B21/M2 (
             B21*11)/M2;
46       0 0 (-K31-K32)/M3 K32/M3 (-K32*13)/M3 0 0 -B31/M3 B31/M3
             (-B31*12)/M3;
47       (K12)/Mt (K22)/Mt (K32)/Mt (-K22-K12-K32)/Mt (-(K12*12)+(
             K22*11)+(K32*13))/Mt (B11)/Mt (B21)/Mt (B31)/Mt (-B11-
             B21-B31)/Mt (-(B11*13)-(B21*11)+(B31*12))/Mt;
48       (K12*12)/It (-K22*11)/It (-K32*13)/It (-(K12*12)+(K22*11)
             +(K32*13))/It (-(K12*12^2)-(K22*11^2)-(K32*13^2))/It (
             B11*13)/It (B21*11)/It (-B31*12)/It (-(B11*13)-(B21*11)
             +(B31*12))/It (-(B11*13^2)-(B21*11^2)-(B31*12^2))/It];
49
50 % Input matrix
51 B = [0 0 0;
52       0 0 0;
53       0 0 0;
54       0 0 0;
55       0 0 0;
56       K11/M1 0 0;
57       0 K21/M2 0;
58       0 0 K31/M3;
59       0 0 0;
60       0 0 0];
61
62 % Output matrix
63 C = [1 0 0 0 0 0 0 0 0 0;
64       0 1 0 0 0 0 0 0 0 0;
65       0 0 1 0 0 0 0 0 0 0;
66       0 0 0 1 0 0 0 0 0 0;
67       0 0 0 0 1 0 0 0 0 0];
68
```

```
% Feedforward matrix
D = [0 0 0;
     0 0 0;
     0 0 0;
     0 0 0;
     0 0 0];


states = {'x1' 'x2' 'x3' 'xt' 'theta_t' 'x1*' 'x2*' 'x3*' 'xt*'
    'theta_t*'};
inputs = {'Disp.Wheel_1' 'Disp.Wheel_2' 'Disp.Wheel_3'};
outputs = {'x1' 'x2' 'x3' 'xt' 'theta_t'};

sys_mimo = ss(A,B,C,D,'statename',states,...
'inputname',inputs,...
'outputname',outputs);

% State space to Transfert Function
TF = tf(sys_mimo);

%% Stability - Pole&Zero Map
stability = eig(A);
figure
pzmap(sys_mimo);


%% Frequency response - BODE
bode(sys_mimo);
for i=1:5
    for j=1:3
    figure
    bode(sys_mimo(i,j))
    end
end

%% Root Locus %%
for i=1:5
    for j=1:3
    figure
```

```
107         rlocus(sys_mimo(i,j))
108         end
109 end
```

APPENDIX B – Bode diagrams

B.1 Four-wheels AGV

Figure 48 – Bode diagrams for the output x_1 - Four-wheels AGV

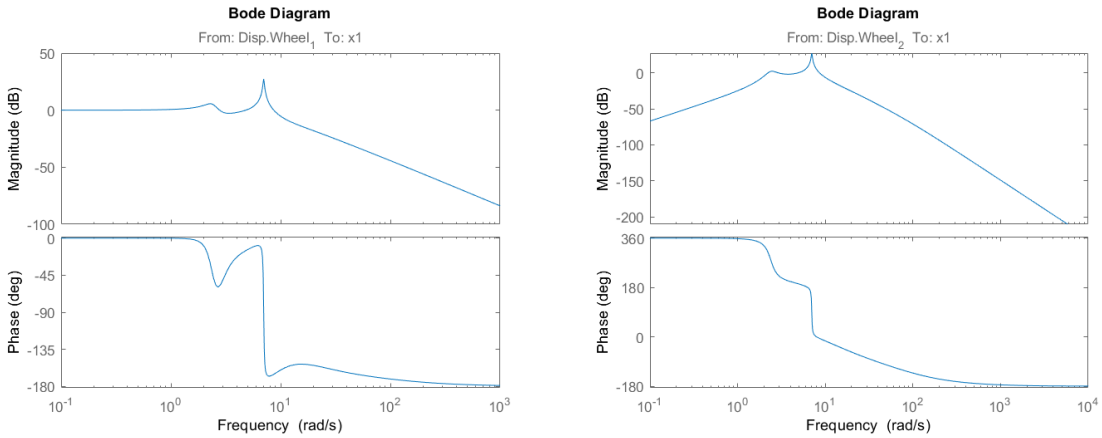

(a) Input q_{i1} (b) Input q_{i2}

Source: Author.

Figure 48a shows the Bode diagram for the output x_1, the linear displacement of the front wheel suspension, considering the input q_{i1} that is the one applied ate the front wheel. Figure 48b shows the Bode diagram for the output x_1, the linear displacement of the front wheel suspension, considering the input q_{i2} that is the one applied ate the rear wheel.

Figure 49 – Bode diagrams for the output x_2 - Four-wheels AGV

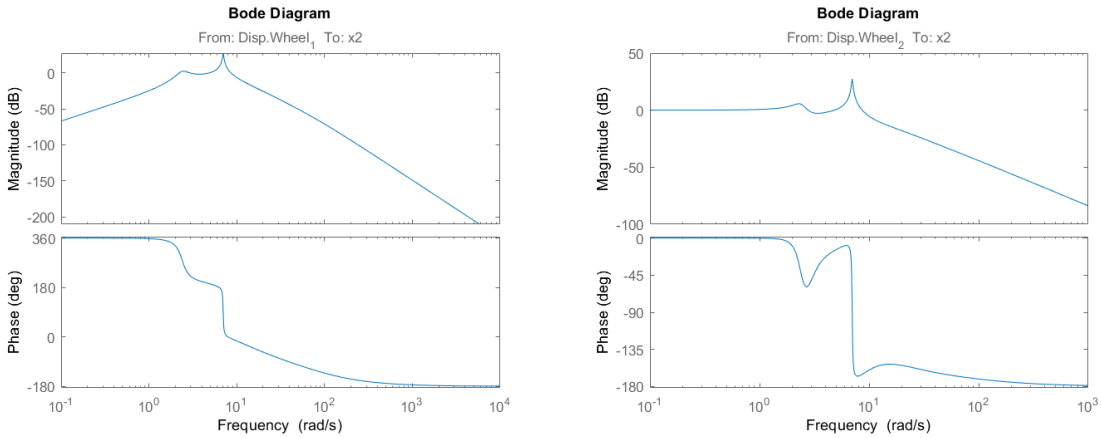

(a) Input q_{i1} (b) Input q_{i2}

Source: Author.

Figure 49a shows the Bode diagram for the output x_2, the linear displacement of the rear wheel suspension, considering the input q_{i1} that is the one applied ate the front wheel. Figure 49b

shows the Bode diagram for the output x_2, the linear displacement of the rear wheel suspension, considering the input q_{i2} that is the one applied ate the rear wheel.

Figure 50 – Bode diagrams for the output x_t - Four-wheels AGV

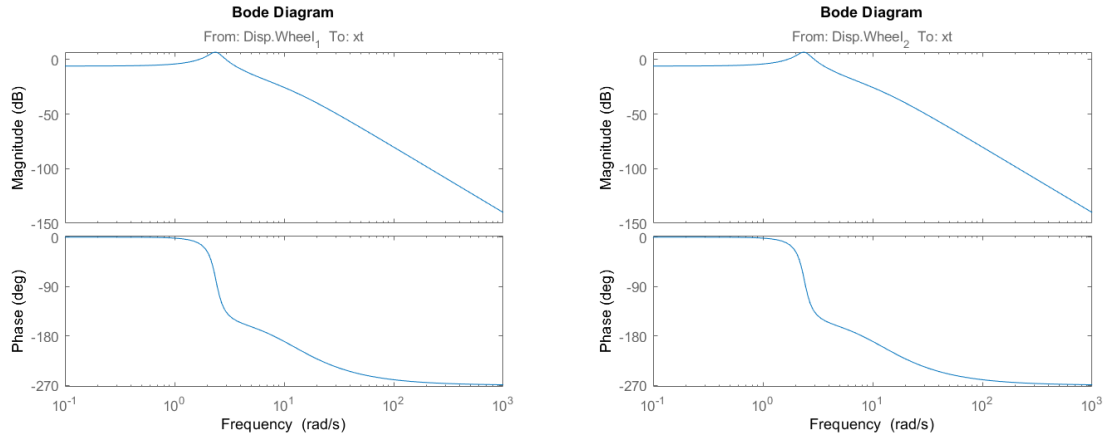

(a) Input q_{i1} (b) Input q_{i2}

Source: Author.

Figure 50a shows the Bode diagram for the output x_t, the linear displacement of the loaded AGV total mass, considering the input q_{i1} that is the one applied ate the front wheel. Figure 50b shows the Bode diagram for the output x_t, linear displacement of the loaded AGV total mass, considering the input q_{i2} that is the one applied ate the rear wheel.

Figure 51 – Bode diagrams for the output θ_t - Four-wheels AGV

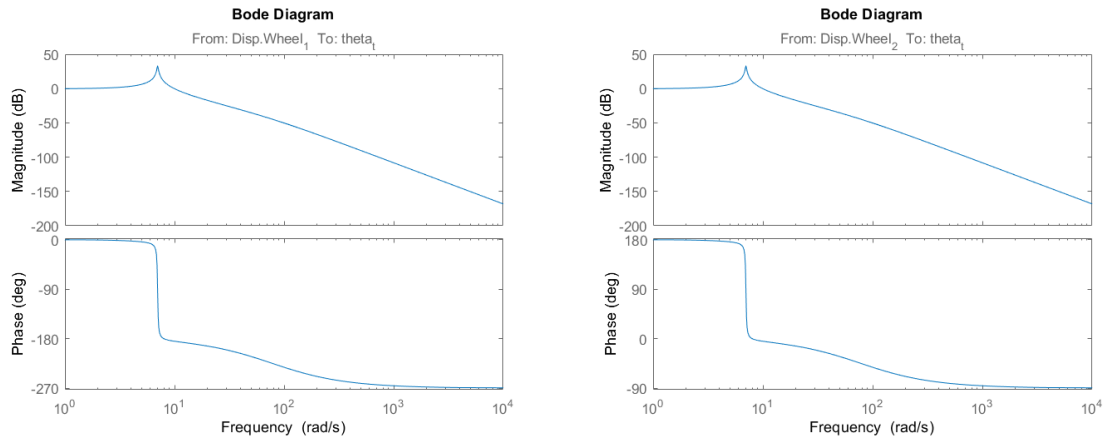

(a) Input q_{i1} (b) Input q_{i2}

Source: Author.

Figure 51a shows the Bode diagram for the output θ_t, the angular displacement of the loaded AGV total mass, considering the input q_{i1} that is the one applied ate the front wheel. Figure 51b shows the Bode diagram for the output θ_t, angular displacement of the loaded AGV total mass, considering the input q_{i2} that is the one applied ate the rear wheel.

B.2 Forklift AGV

Figure 52 – Bode diagrams for the output x_1 - Forklift AGV

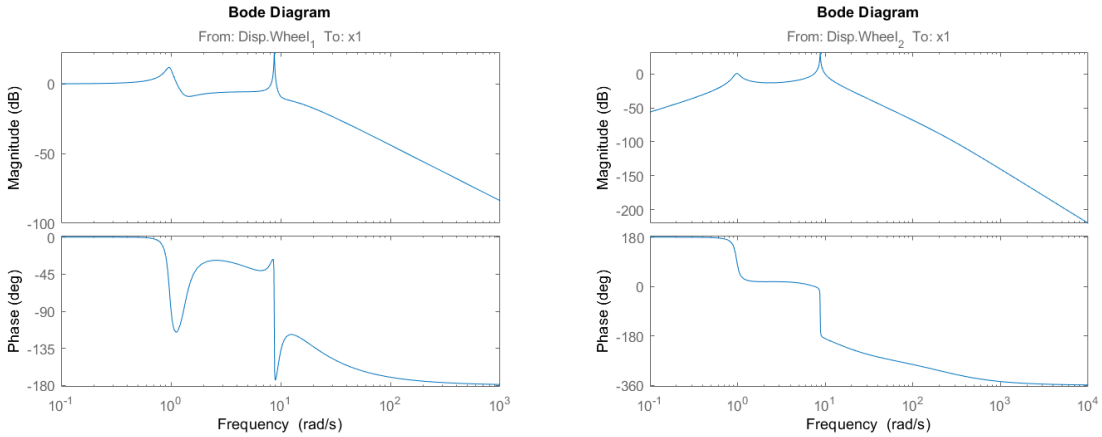

(a) Input q_{i1} (b) Input q_{i2}

Source: Author.

Figure 52a shows the Bode diagram for the output x_1, the linear displacement of the front wheel suspension, considering the input q_{i1} that is the one applied ate the front wheel. Figure 52b shows the Bode diagram for the output x_1, the linear displacement of the front wheel suspension, considering the input q_{i2} that is the one applied ate the rear wheel.

Figure 53 – Bode diagrams for the output x_2 - Forklift AGV

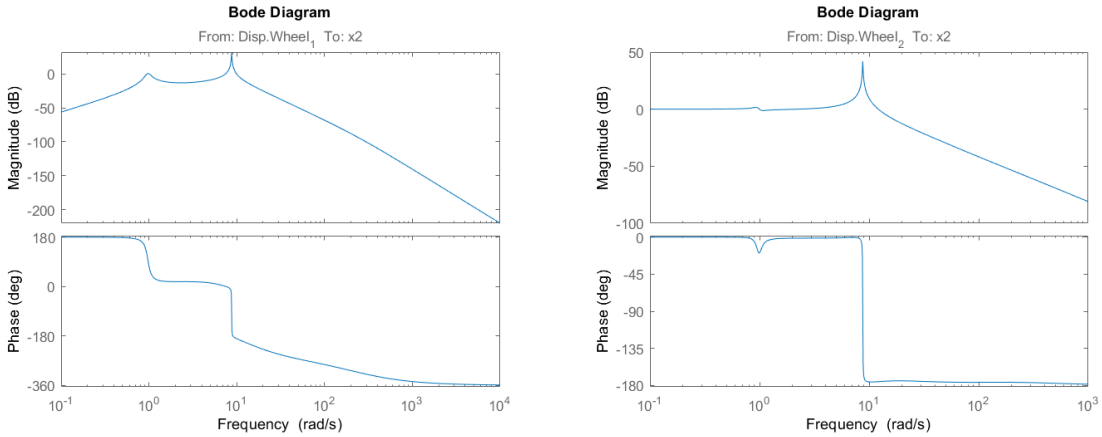

(a) Input q_{i1} (b) Input q_{i2}

Source: Author.

Figure 53a shows the Bode diagram for the output x_2, the linear displacement of the rear wheel suspension, considering the input q_{i1} that is the one applied ate the front wheel. Figure 53b shows the Bode diagram for the output x_2, the linear displacement of the rear wheel suspension, considering the input q_{i2} that is the one applied ate the rear wheel.

Figure 54a shows the Bode diagram for the output x_t, the linear displacement of the loaded AGV total mass, considering the input q_{i1} that is the one applied ate the front wheel.

Figure 54 – Bode diagrams for the output x_t - Forklift AGV

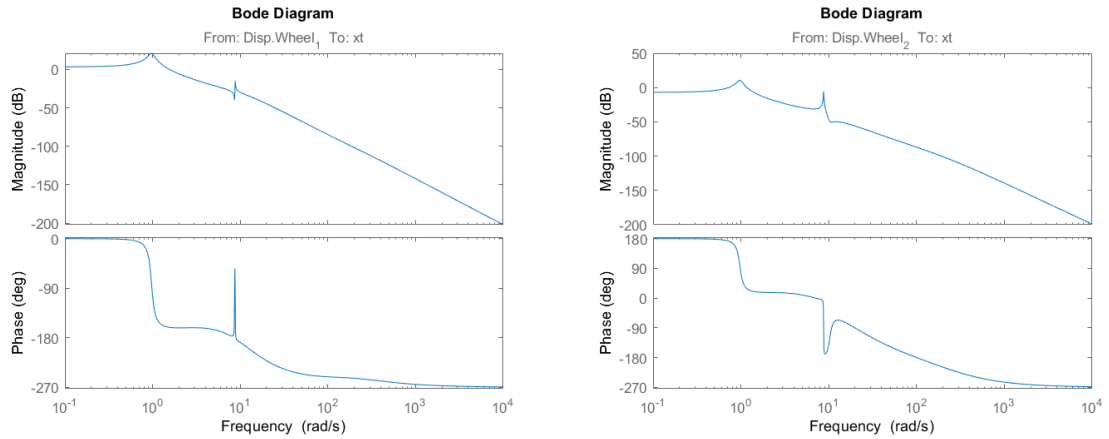

(a) Input q_{i1} (b) Input q_{i2}

Source: Author.

Figure 54b shows the Bode diagram for the output x_t, linear displacement of the loaded AGV total mass, considering the input q_{i2} that is the one applied ate the rear wheel.

Figure 55 – Bode diagrams for the output θ_t - Forklift AGV

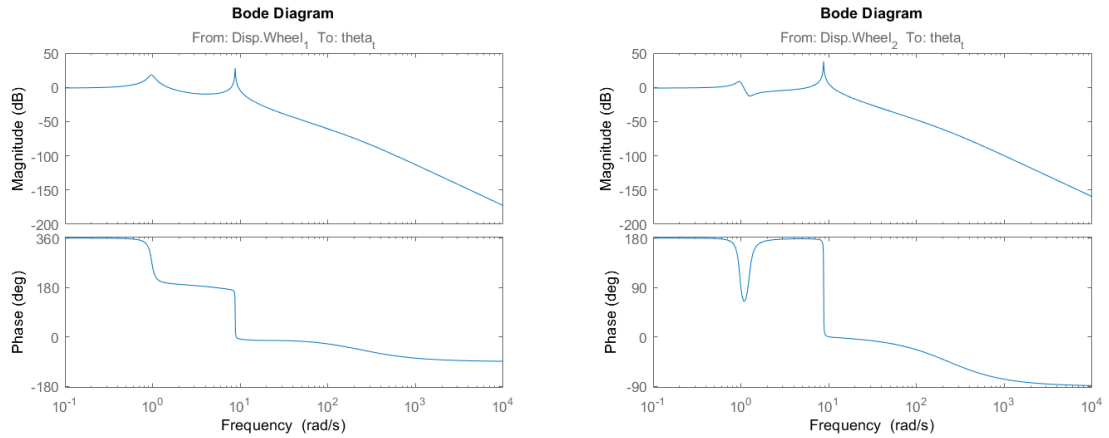

(a) Input q_{i1} (b) Input q_{i2}

Source: Author.

Figure 55a shows the Bode diagram for the output θ_t, the angular displacement of the loaded AGV total mass, considering the input q_{i1} that is the one applied ate the front wheel. Figure 55b shows the Bode diagram for the output θ_t, angular displacement of the loaded AGV total mass, considering the input q_{i2} that is the one applied ate the rear wheel.

B.3 Six-wheels AGV

Figure 56 – Bode diagrams for the output x_1 - Six-wheels AGV

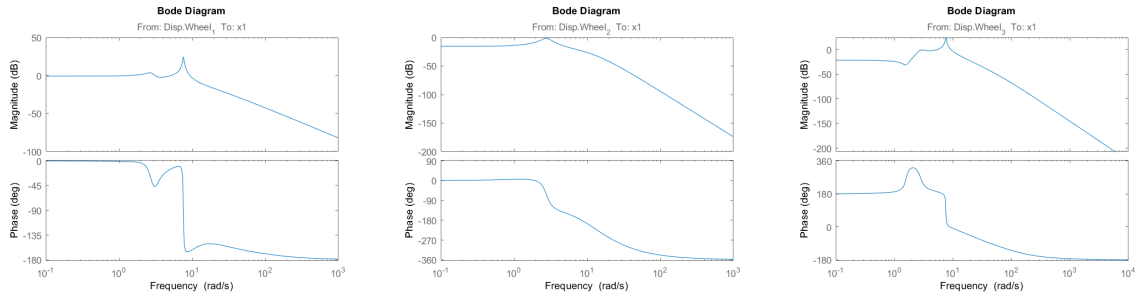

(a) Input q_{i1} (b) Input q_{i2} (c) Input q_{i3}

Source: Author.

Figure 56a shows the Bode diagram for the output x_1, the linear displacement of the front wheel suspension, considering the input q_{i1} that is the one applied ate the front wheel. Figure 56b shows the Bode diagram for the output x_1, the linear displacement of the front wheel suspension, considering the input q_{i2} that is the one applied ate the center wheel. Figure 56c shows the Bode diagram for the output x_1, the linear displacement of the front wheel suspension, considering the input q_{i3} that is the one applied ate the rear wheel.

Figure 57 – Bode diagrams for the output x_2 - Six-wheels AGV

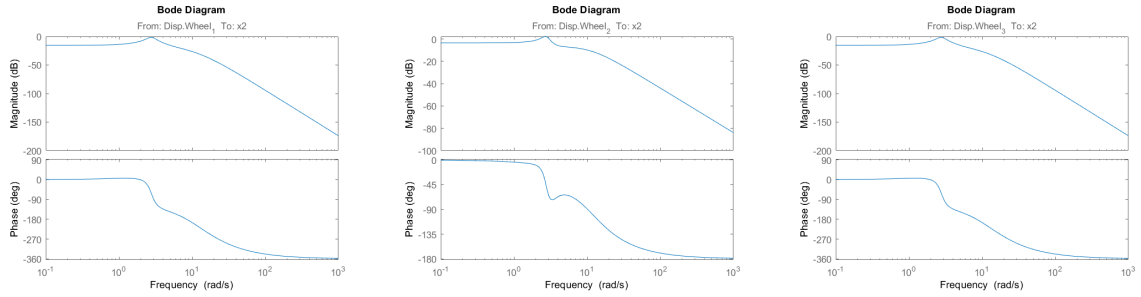

(a) Input q_{i1} (b) Input q_{i2} (c) Input q_{i3}

Source: Author.

Figure 57a shows the Bode diagram for the output x_2, the linear displacement of the center wheel suspension, considering the input q_{i1} that is the one applied ate the front wheel. Figure 57b shows the Bode diagram for the output x_2, the linear displacement of the center wheel suspension, considering the input q_{i2} that is the one applied ate the center wheel. Figure 57c shows the Bode diagram for the output x_2, the linear displacement of the center wheel suspension, considering the input q_{i3} that is the one applied ate the rear wheel.

Figure 58a shows the Bode diagram for the output x_3, the linear displacement of the rear wheel suspension, considering the input q_{i1} that is the one applied ate the front wheel. Figure 58b shows the Bode diagram for the output x_3, the linear displacement of the rear wheel suspension, considering the input q_{i2} that is the one applied ate the center wheel. Figure 58c shows the Bode

Figure 58 – Bode diagrams for the output x_3 - Six-wheels AGV

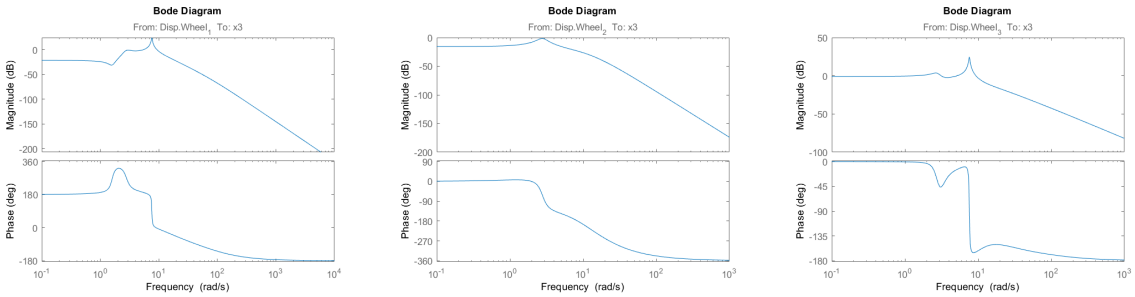

(a) Input q_{i1} (b) Input q_{i2} (c) Input q_{i3}

Source: Author.

diagram for the output x_3, the linear displacement of the rear wheel suspension, considering the input q_{i3} that is the one applied ate the rear wheel.

Figure 59 – Bode diagrams for the output x_t - Six-wheels AGV

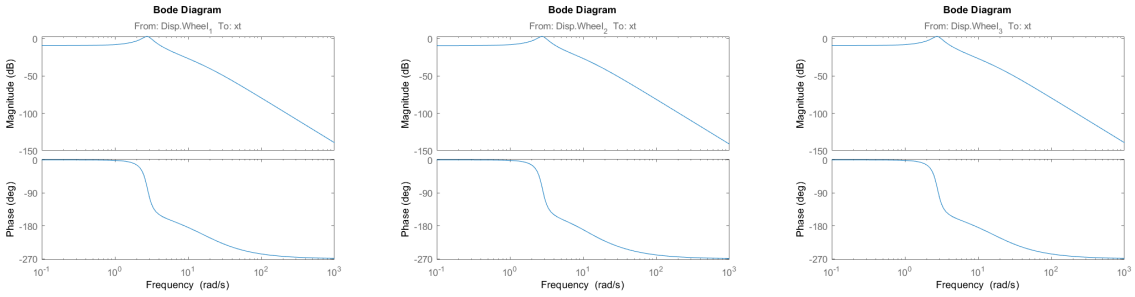

(a) Input q_{i1} (b) Input q_{i2} (c) Input q_{i3}

Source: Author.

Figure 59a shows the Bode diagram for the output x_t, the linear displacement of the loaded AGV total mass, considering the input q_{i1} that is the one applied ate the front wheel. Figure 59b shows the Bode diagram for the output x_t, the linear displacement of the loaded AGV total mass, considering the input q_{i2} that is the one applied ate the center wheel. Figure 59c shows the Bode diagram for the output x_t, the linear displacement of the loaded AGV total mass, considering the input q_{i3} that is the one applied ate the rear wheel.

Figure 60 – Bode diagrams for the output θ_t - Six-wheels AGV

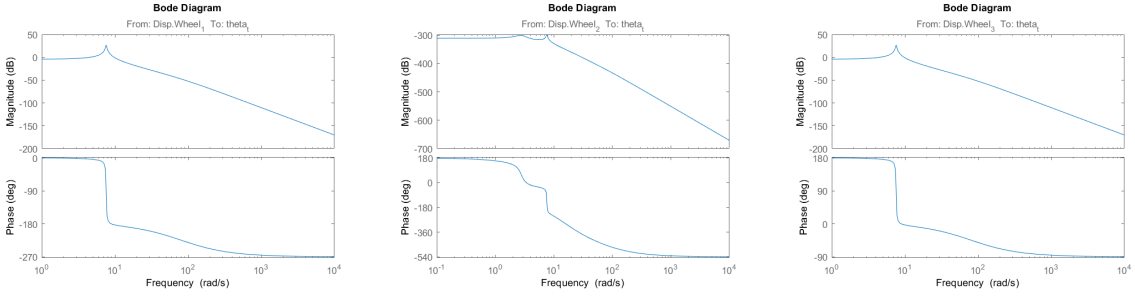

(a) Input q_{i1} (b) Input q_{i2} (c) Input q_{i3}

Source: Author.

Figure 60a shows the Bode diagram for the output θ_t, the angular displacement of the loaded AGV total mass, considering the input q_{i1} that is the one applied ate the front wheel. Figure 60b shows the Bode diagram for the output θ_t, the angular displacement of the loaded AGV total mass, considering the input q_{i2} that is the one applied ate the center wheel. Figure 60c shows the Bode diagram for the output θ_t, the angular displacement of the loaded AGV total mass, considering the input q_{i3} that is the one applied ate the rear wheel.

APPENDIX C – Root locus graphs

C.1 Four-wheels AGV

Figure 61 – Root locus diagrams for the output x_1 - Four-wheels AGV

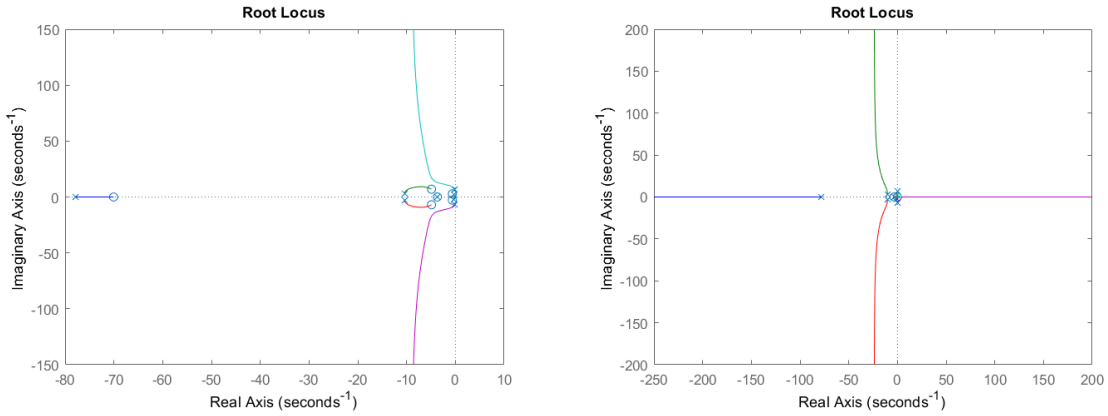

(a) Input q_{i1} (b) Input q_{i2}

Source: Author.

Figure 61a shows the Root Locus graph for the output x_1, the linear displacement of the front wheel suspension, considering the input q_{i1} that is the one applied ate the front wheel. Figure 61b shows the Root Locus graph for the output x_1, the linear displacement of the front wheel suspension, considering the input q_{i2} that is the one applied ate the rear wheel.

Figure 62 – Root locus diagrams for the output x_2 - Four-wheels AGV

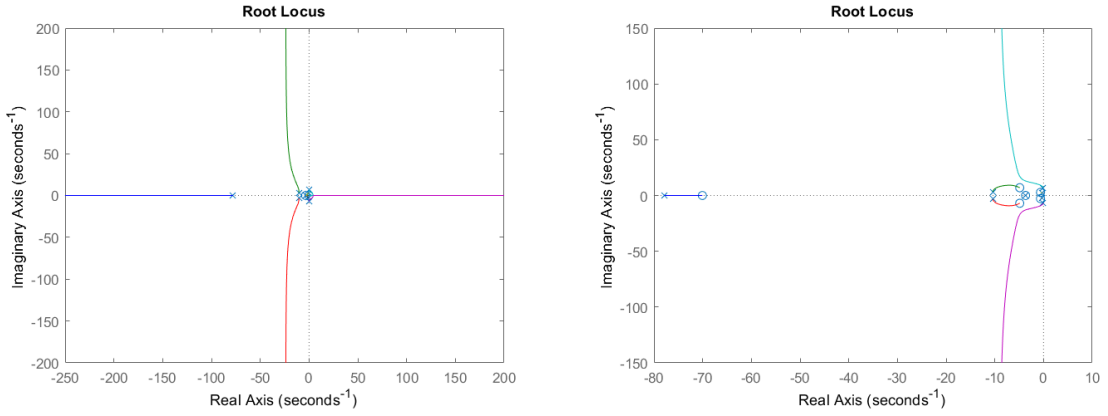

(a) Input q_{i1} (b) Input q_{i2}

Source: Author.

Figure 62a shows the Root Locus graph for the output x_2, the linear displacement of the rear wheel suspension, considering the input q_{i1} that is the one applied ate the front wheel.

Figure 62b shows the Root Locus graph for the output x_2, the linear displacement of the rear wheel suspension, considering the input q_{i2} that is the one applied ate the rear wheel.

Figure 63 – Root locus diagrams for the output x_t - Four-wheels AGV

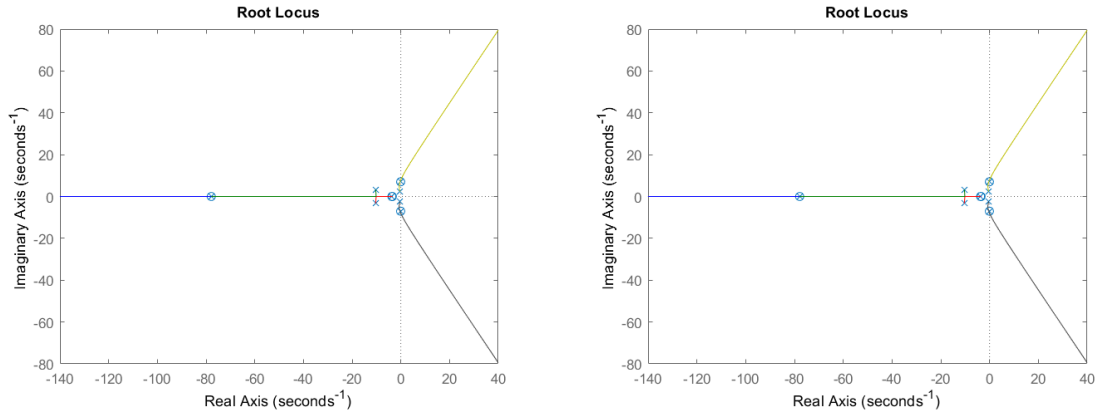

(a) Input q_{i1} (b) Input q_{i2}

Source: Author.

Figure 63a shows the Root Locus graph for the output x_t, the linear displacement of the loaded AGV total mass, considering the input q_{i1} that is the one applied ate the front wheel. Figure 63b shows the Root Locus graph for the output x_t, the linear displacement of the loaded AGV total mass, considering the input q_{i2} that is the one applied ate the rear wheel.

Figure 64 – Root locus diagrams for the output θ_t - Four-wheels AGV

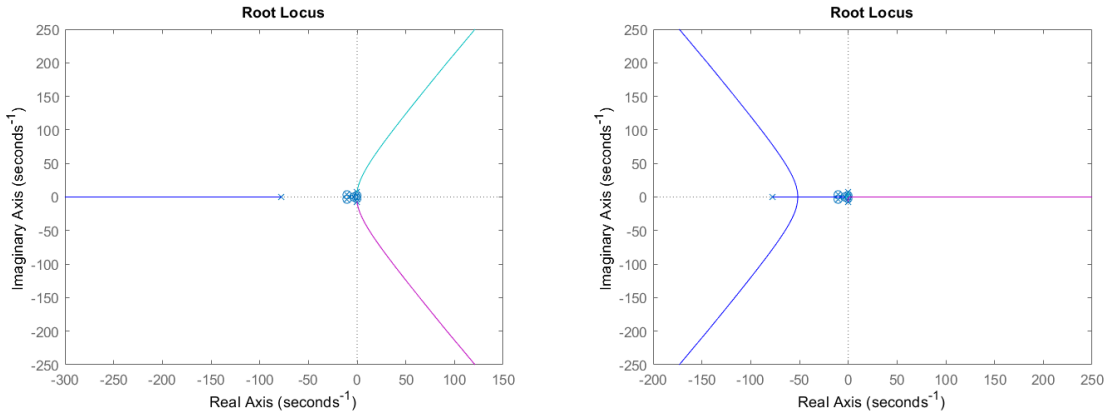

(a) Input q_{i1} (b) Input q_{i2}

Source: Author.

Figure 64a shows the Root Locus graph for the output θ_t, the angular displacement of the loaded AGV total mass, considering the input q_{i1} that is the one applied ate the front wheel. Figure 64b shows the Root Locus graph for the output θ_t, the angular displacement of the loaded AGV total mass, considering the input q_{i2} that is the one applied ate the rear wheel.

C.2 Forklift AGV

Figure 65 – Root locus diagrams for the output x_1 - Forklift AGV

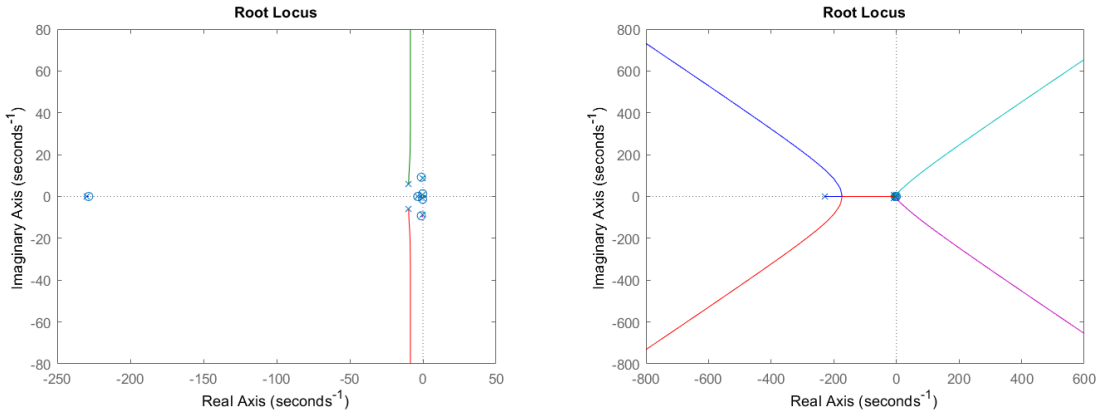

(a) Input q_{i1} (b) Input q_{i2}

Source: Author.

Figure 65a shows the Root Locus graph for the output x_1, the linear displacement of the front wheel suspension, considering the input q_{i1} that is the one applied ate the front wheel. Figure 65b shows the Root Locus graph for the output x_1, the linear displacement of the front wheel suspension, considering the input q_{i2} that is the one applied ate the rear wheel.

Figure 66 – Root locus diagrams for the output x_2 - Forklift AGV

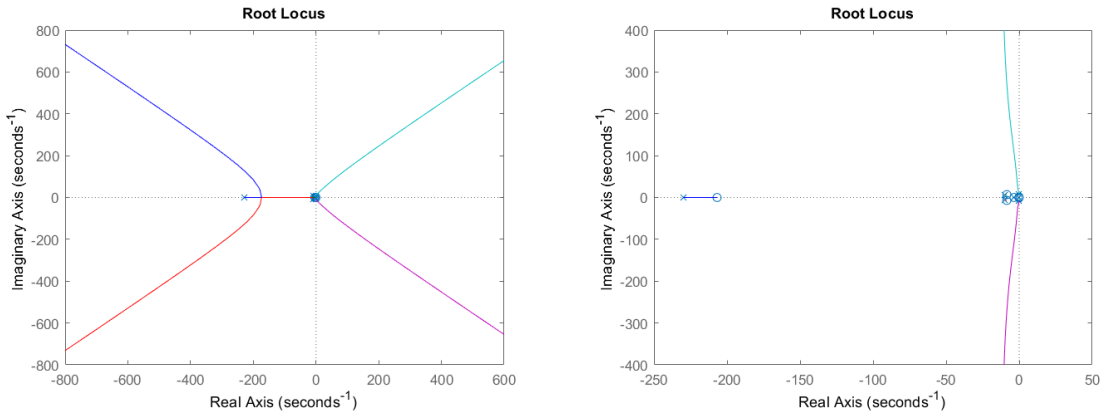

(a) Input q_{i1} (b) Input q_{i2}

Source: Author.

Figure 66a shows the Root Locus graph for the output x_2, the linear displacement of the rear wheel suspension, considering the input q_{i1} that is the one applied ate the front wheel. Figure 66b shows the Root Locus graph for the output x_2, the linear displacement of the rear wheel suspension, considering the input q_{i2} that is the one applied ate the rear wheel.

Figure 67a shows the Root Locus graph for the output x_t, the linear displacement of the loaded AGV total mass, considering the input q_{i1} that is the one applied ate the front wheel.

Figure 67 – Root locus diagrams for the output x_t - Forklift AGV

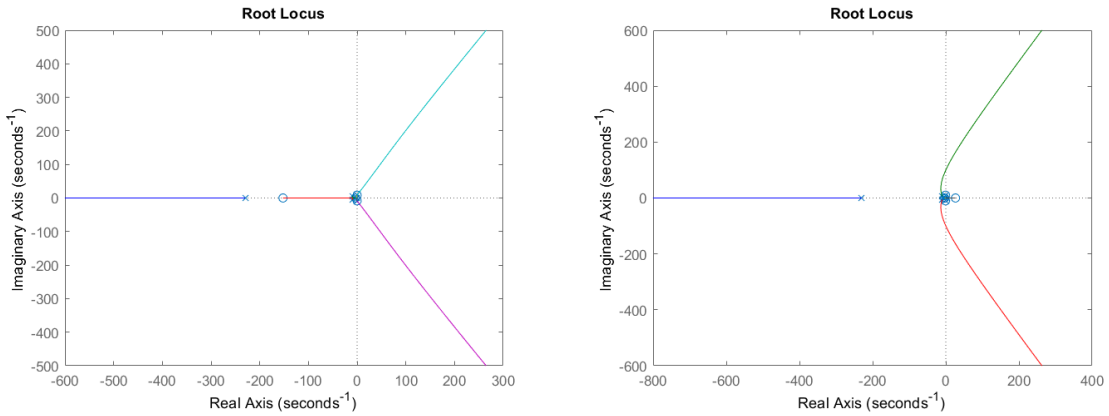

(a) Input q_{i1} (b) Input q_{i2}

Source: Author.

Figure 67b shows the Root Locus graph for the output x_t, the linear displacement of the loaded AGV total mass, considering the input q_{i2} that is the one applied ate the rear wheel.

Figure 68 – Root locus diagrams for the output θ_t - Forklift AGV

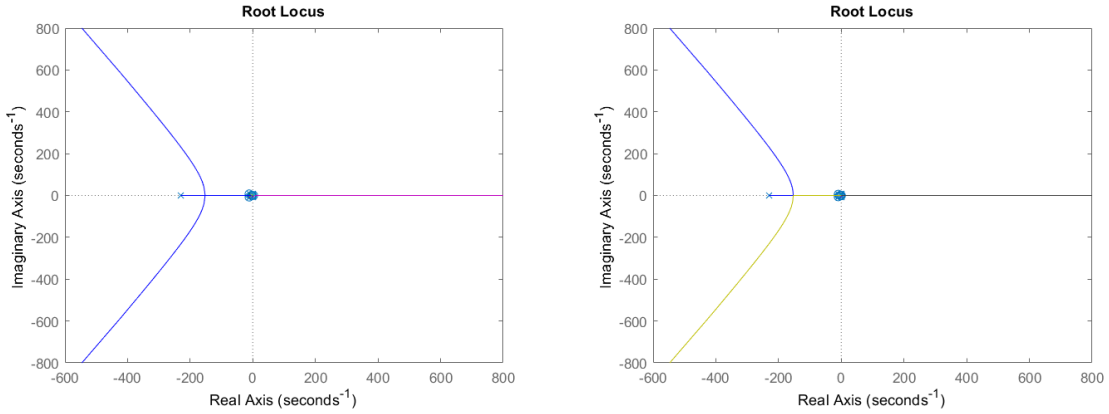

(a) Input q_{i1} (b) Input q_{i2}

Source: Author.

Figure 68a shows the Root Locus graph for the output θ_t, the angular displacement of the loaded AGV total mass, considering the input q_{i1} that is the one applied ate the front wheel. Figure 68b shows the Root Locus graph for the output θ_t, the angular displacement of the loaded AGV total mass, considering the input q_{i2} that is the one applied ate the rear wheel.

C.3 Six-wheels AGV

Figure 69 – Root locus diagrams for the output x_1 - Six-wheels AGV

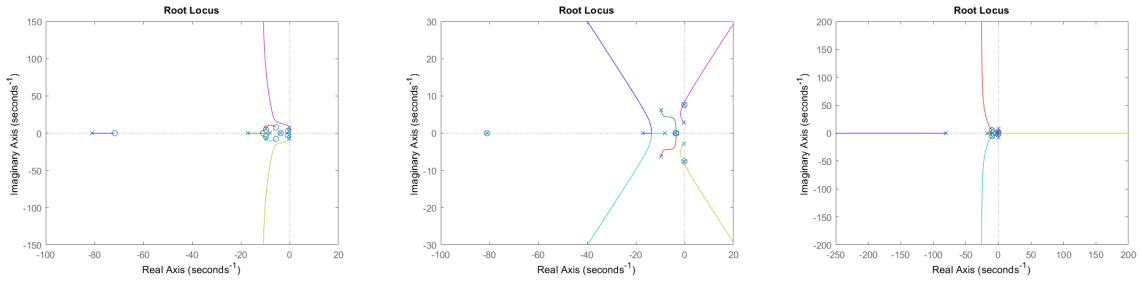

(a) Input q_{i1} (b) Input q_{i2} (c) Input q_{i3}

Source: Author.

Figure 69a shows the Root Locus graph for the output x_1, the linear displacement of the front wheel suspension, considering the input q_{i1} that is the one applied ate the front wheel. Figure 69b shows the Root Locus graph for the output x_1, the linear displacement of the front wheel suspension, considering the input q_{i2} that is the one applied ate the center wheel. Figure 69c shows the Root Locus graph for the output x_1, the linear displacement of the front wheel suspension, considering the input q_{i3} that is the one applied ate the rear wheel.

Figure 70 – Root locus diagrams for the output x_2 - Six-wheels AGV

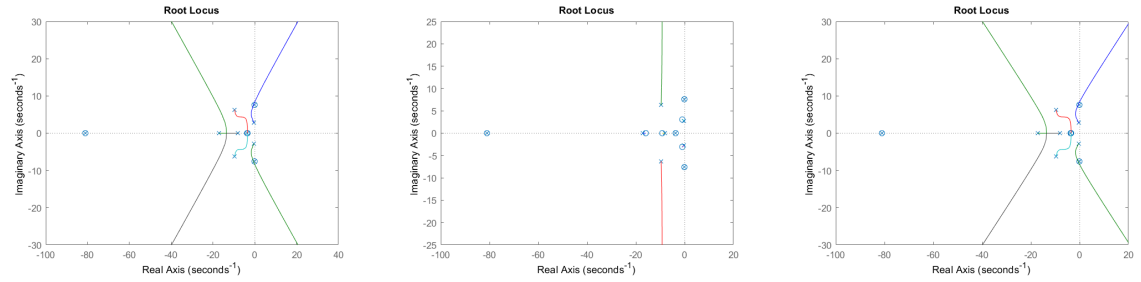

(a) Input q_{i1} (b) Input q_{i2} (c) Input q_{i3}

Source: Author.

Figure 70a shows the Root Locus graph for the output x_2, the linear displacement of the center wheel suspension, considering the input q_{i1} that is the one applied ate the front wheel. Figure 70b shows the Root Locus graph for the output x_2, the linear displacement of the center wheel suspension, considering the input q_{i2} that is the one applied ate the center wheel. Figure 70c shows the Root Locus graph for the output x_2, the linear displacement of the center wheel suspension, considering the input q_{i3} that is the one applied ate the rear wheel.

Figure 71a shows the Root Locus graph for the output x_3, the linear displacement of the rear wheel suspension, considering the input q_{i1} that is the one applied ate the front wheel. Figure 71b shows the Root Locus graph for the output x_3, the linear displacement of the rear wheel suspension, considering the input q_{i2} that is the one applied ate the center wheel. Figure

Figure 71 – Root locus diagrams for the output x_3 - Six-wheels AGV

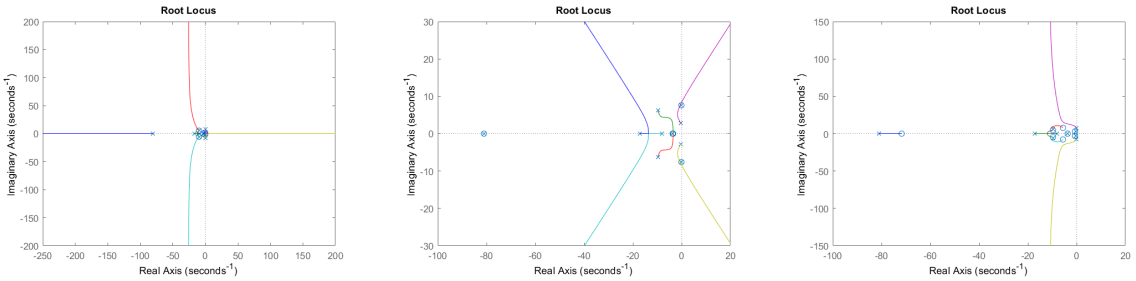

(a) Input q_{i1} (b) Input q_{i2} (c) Input q_{i3}

Source: Author.

71c shows the Root Locus graph for the output x_3, the linear displacement of the rear wheel suspension, considering the input q_{i3} that is the one applied ate the rear wheel.

Figure 72 – Root locus diagrams for the output x_t - Six-wheels AGV

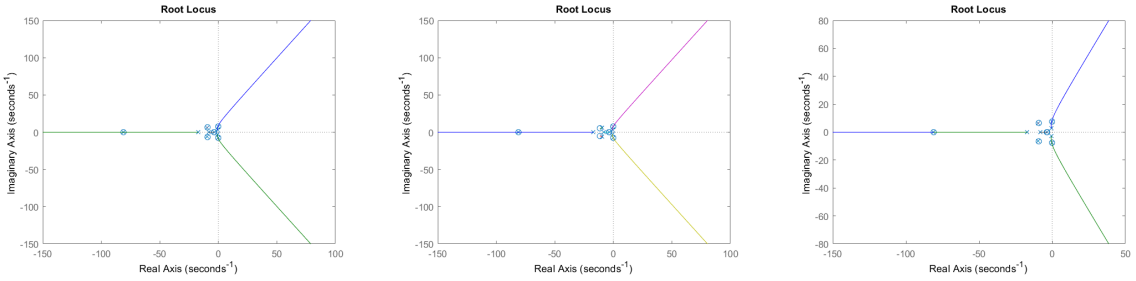

(a) Input q_{i1} (b) Input q_{i2} (c) Input q_{i3}

Source: Author.

Figure 72a shows the Root Locus graph for the output x_t, the linear displacement of the loaded AGV total mass, considering the input q_{i1} that is the one applied ate the front wheel. Figure 72b shows the Root Locus graph for the output x_t, the linear displacement of the loaded AGV total mass, considering the input q_{i2} that is the one applied ate the center wheel. Figure 72c shows the Root Locus graph for the output x_t, the linear displacement of the loaded AGV total mass, considering the input q_{i3} that is the one applied ate the rear wheel.

Figure 73 – Root locus diagrams for the output θ_t - Six-wheels AGV

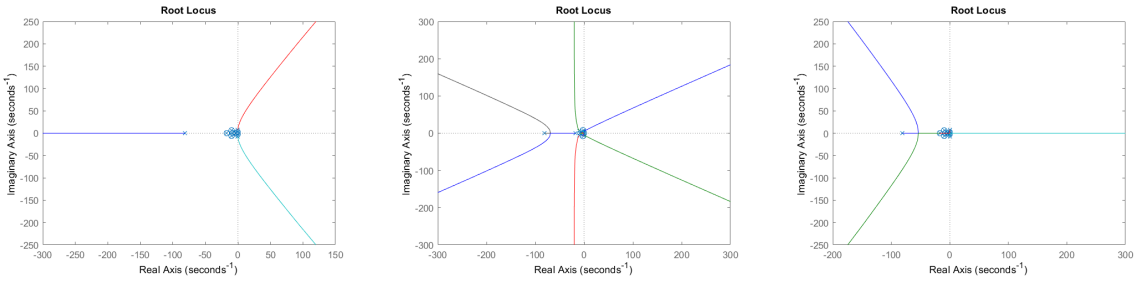

(a) Input q_{i1} (b) Input q_{i2} (c) Input q_{i3}

Source: Author.

Figure 73a shows the Root Locus graph for the output θ_t, the angular displacement of the loaded AGV total mass, considering the input q_{i1} that is the one applied ate the front wheel. Figure 73b shows the Root Locus graph for the output θ_t, the angular displacement of the loaded AGV total mass, considering the input q_{i2} that is the one applied ate the center wheel. Figure 73c shows the Root Locus graph for the output θ_t, the angular displacement of the loaded AGV total mass, considering the input q_{i3} that is the one applied ate the rear wheel.